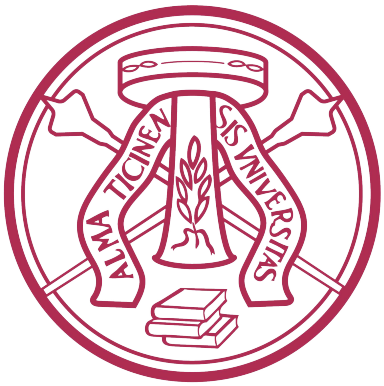

UNIVERSITÀ
DI PAVIA

Dipartimento di Fisica

Corso di Laurea Magistrale in Scienze Fisiche

Theory of a quantum Mach-Zehnder interferometer

Teoria di un interferometro di Mach-Zehnder quantistico

Tesi per la Laurea Magistrale di:
Antonio Martucci

Relatore:
Prof. Dario Gerace

Correlatore:
Dr. Davide Rinaldi

A.A. 2025-2026

Abstract

The Mach-Zehnder interferometer is a key element in optics and integrated photonics, with applications ranging from precision metrology to quantum optics. The device splits an optical signal into two paths and recombines them: the output at each port depends on the phase shift between the arms, which can be exploited to route the signal toward one port or the other. With the development of integrated nanophotonic platforms, it is now possible to build interferometers where the signal is a single photon propagating in a waveguide, and the phase shift is induced by the interaction with a single quantum emitter coupled to one of the two arms. In this context, a complete theoretical treatment of the Mach-Zehnder interferometer with a single input photon and a single qubit — in its technological realization, a semiconductor quantum dot — as the active phase-control element appears to be missing from the literature.

In this thesis, a complete calculation of the response of such an interferometer is developed, modelling the quantum dot as a two-level system (TLS) coupled directly to the waveguide, and subsequently as a Jaynes–Cummings (JC) system in which the emitter is embedded in an optical cavity coupled in turn to the waveguide. The adopted formalism is the time-bin framework, which discretizes the photonic field into temporal modes and reduces the dynamics to a collisional model that can be solved step by step. For the TLS case, a closed-form analytical solution is derived for the transmission and reflection probabilities and the phase shift as a function of the detuning. A comparison with a numerical simulation and an independent Runge–Kutta integration confirms the validity of the method. The core of the work is the extension to the JC system: the time-bin simulation is in this case the only available tool and allows the interferometer response to be explored as a function of the qubit-cavity coupling and the pulse bandwidth.

The results show that in both configurations the single photon can be routed from the transmission port to the reflection port with near-unity efficiency, when the pulse bandwidth is sufficiently narrow compared to the system linewidth. In the JC case, the transmission as a function of detuning exhibits the characteristic vacuum Rabi splitting, with two minima separated by $2g$, where g is the qubit-cavity coupling strength, and the effective phase shift displays π discontinuities at the reflection maxima, confirming the consistency between the phase and amplitude response. These results may find application in the realization of high-efficiency optical switches at the single-photon level, or in proof-of-concept demonstrations of quantum machine learning and quantum simulation.

L'interferometro di Mach-Zehnder è un elemento centrale in ottica e fotonica integrata, con applicazioni che spaziano dalla metrologia di precisione all'ottica quantistica. Il dispositivo divide un segnale ottico in due cammini e li ricombina: l'uscita delle due porte dipende dallo sfasamento tra i bracci, che può essere sfruttato per instradare il segnale verso l'una o l'altra porta. Con lo sviluppo di piattaforme nanofotoniche integrate, è oggi possibile realizzare interferometri in cui il segnale è un singolo fotone propagante in guida d'onda, e lo sfasamento è indotto dall'interazione con un singolo emettitore quantistico accoppiato a uno dei due bracci. In questo contesto, sembra mancare in letteratura una trattazione teorica completa che consideri un singolo fotone in ingresso e un singolo qubit — nella realizzazione tecnologica, un quantum dot semiconduttore — come elemento attivo per il controllo della fase.

In questa tesi viene sviluppato un calcolo completo della risposta di un tale interferometro, modellizzando il quantum dot come un sistema a due livelli (TLS) accoppiato direttamente alla guida d'onda, e successivamente come un sistema di Jaynes–Cummings (JC) in cui l'emettitore è inserito in una cavità ottica a sua volta accoppiata alla guida. Il formalismo adottato è quello dei time bins, che discretizza il campo fotonico in modi temporali e riduce la dinamica a un modello collisionale risolubile passo per passo. Per il caso del TLS viene derivata una soluzione analitica in forma chiusa per le probabilità di trasmissione, riflessione e lo sfasamento in funzione del detuning, e il confronto con una simulazione numerica e con un'integrazione Runge–Kutta indipendente conferma la validità del metodo. Il cuore del lavoro è l'estensione al sistema JC, per il quale non esiste una soluzione analitica: la simulazione time-bin costituisce in questo caso l'unico strumento di indagine e permette di esplorare la risposta dell'interferometro al variare dell'accoppiamento qubit-cavità e della bandwidth dell'impulso.

I risultati mostrano che in entrambe le configurazioni il singolo fotone può essere instradato dalla porta di trasmissione alla porta di riflessione con efficienza prossima all'unità, quando la bandwidth dell'impulso è sufficientemente stretta rispetto alla larghezza di riga del sistema. Nel caso JC, la trasmissione in funzione del detuning presenta il caratteristico vacuum Rabi splitting, con due minimi separati di $2g$, dove g è la costante di accoppiamento qubit-cavità, e lo sfasamento effettivo mostra discontinuità di π in corrispondenza dei massimi di riflessione, confermando la coerenza tra risposta in fase e in ampiezza. Questi risultati possono trovare applicazione nella realizzazione di switch ottici ad alta efficienza a livello di singolo fotone, o in dimostrazioni proof-of-concept di quantum machine learning e simulazione quantistica.

Contents

Introduction

Photons propagating through free space do not interact with one another. This linearity, while enabling long-distance transmission of quantum information, prevents the direct realization of photon-photon gates and nonlinear optical operations at the single-quantum level [CVL14]. In conventional optical media, nonlinear effects become appreciable only when the number of photons involved is large, because the interaction cross-section between a single photon and a single atom in free space is exceedingly small — of order λ^2/d^2, where λ is the optical wavelength and d the transverse confinement of the beam [CVL14]. Reaching the regime of quantum nonlinear optics, in which the propagation of light depends measurably on whether one or two photons are present, requires enhancing this interaction probability to values approaching unity. Two complementary strategies have been pursued. The first employs high-finesse optical cavities, where a photon bounces between mirrors many times and the effective interaction probability scales with the cooperativity parameter, $\eta \approx F\lambda^2/d^2$ [CVL14], and thus with the cavity finesse, F. The second confines light to sub-wavelength dimensions in nanophotonic waveguides, suppressing unwanted radiation channels and funnelling the emission of the emitter into a single guided mode [LMS15]. In both cases, the key figure of merit is the probability that a single propagating photon interacts with a single quantum emitter during a single pass. When this probability approaches unity, the absorption of one photon saturates the emitter and alters its response to a second photon arriving within the excited-state lifetime, producing a strongly nonlinear optical response at the level of individual quanta [CVL14]. Solid-state implementations based on semiconductor quantum dots embedded in photonic nanostructures have proven particularly promising in this respect, combining near-unity light-matter coupling efficiencies with the scalability of nanofabrication technology [LMS15]

Among solid-state quantum emitters, semiconductor quantum dots occupy a distinctive position. A quantum dot is a nanometre-scale heterostructure in which electrons and holes are confined in all three spatial dimensions, resulting in a discrete, atom-like energy spectrum [LMS15]. Self-assembled InGaAs quantum dots grown by molecular-beam epitaxy on GaAs substrates are among the most widely studied platforms for quantum-optics experiments at optical frequencies. Their opti-

cal transitions can be made nearly lifetime-limited at cryogenic temperatures, where phonon-induced decoherence is suppressed and the emission linewidth approaches the Fourier-transform limit [Upp+21]. When embedded in a photonic-crystal waveguide, a quantum dot couples preferentially to the guided mode. The figure of merit for this coupling is the β-factor, defined as the fraction of the total spontaneous emission rate directed into the waveguide mode; near-unity values have been reported in photonic-crystal waveguide geometries [LMS15; Upp+21]. Such high coupling efficiencies make waveguide-coupled quantum dots behave as strongly nonlinear optical elements at the single-photon level: a single resonant photon is reflected with high probability, while two-photon wavepackets are partly transmitted due to the saturation of the emitter [Upp+21]. An additional degree of control is provided by the DC Stark effect. By applying a static electric field across a *p-i-n* diode structure in which the quantum dot is embedded, the exciton transition energy can be tuned electrically over a range of several linewidths [Hal+18]. This enables fast, reversible switching of the quantum dot into and out of resonance with the waveguide mode, with measured switching times as short as 80 ns [Hal+18]. The combination of near-unity β-factors, transform-limited emission, and electrical tunability makes waveguide-coupled quantum dots a mature platform for the investigation of single-photon nonlinear phenomena in integrated photonic circuits.

The nonlinear response of a waveguide-coupled quantum emitter manifests itself most directly in the phase and amplitude of the transmitted and reflected fields. For a single photon at resonance with a two-level emitter in a waveguide, the transmission coefficient acquires a phase shift whose maximum value is $\pi/2$ in the ideal case of unity β-factor, while the photon is predominantly reflected [SF09; Upp+21]. When the emitter is coupled to a single-mode cavity that is in turn side-coupled to the waveguide, instead, the transmission spectrum exhibits a richer structure. Shen and Fan provided an exact analytical solution for the single-photon transport in this configuration, showing that when the cavity mode and the atomic transition are in resonance condition, the transmission spectrum displays two dips separated by $2g$, where g is the atom-cavity coupling strength — a signature of the vacuum Rabi splitting [SF09]. At the Rabi-split frequencies $\omega = \Omega \pm g$, the photon is completely reflected. A particularly striking feature emerges when the atom is far detuned from the cavity resonance: the transmission at the cavity frequency drops to zero while remaining unity at the atomic frequency, such that the system acts as a single-photon switch controlled by the atomic transition frequency [SF09].

An experimental observation of the emitter-induced phase shift in a waveguide geometry was recently reported by Staunstrup *et al.* [Sta+24]. In this experiment, a Mach-Zehnder interferometer of approximately 3 m in length was built on top of a closed-cycle cryostat, with one arm containing a GaAs photonic-crystal waveg-

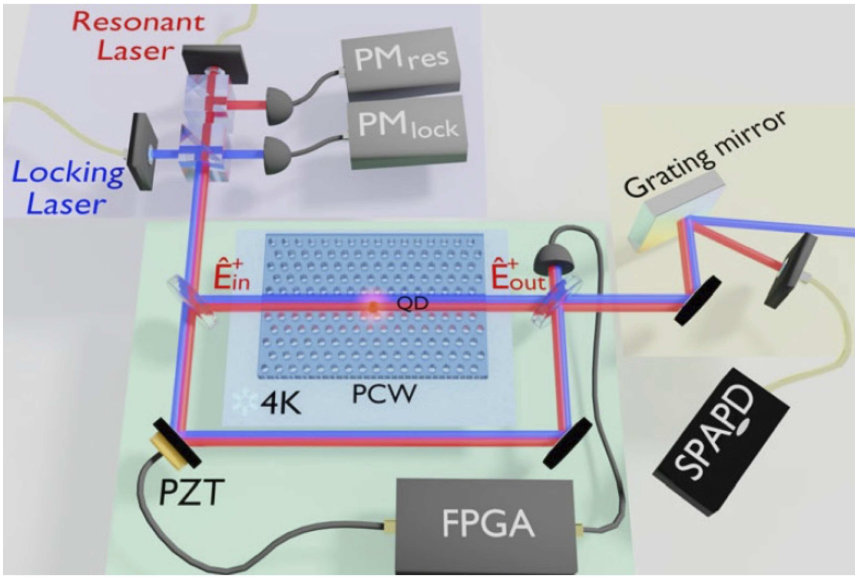

Figure 1: Schematic illustration of the quantum Mach-Zehnder interferometer employed in the experiment of Ref. [Sta+24]. A weak coherent beam (few photons on average) enters the first beam splitter into an equal superposition of the beam traveling in free space, and the beam traveling thorugh a photonic crystal waveguide, in which it interacts with a single quantum dot. Figure adapted from the original work in [Sta+24].

uide with a single embedded InGaAs quantum dot. A scheme of this state-of-art experiment is reported in Fig. 1 , as taken from the original reference. By sweeping the frequency of a weak coherent laser across the quantum dot resonance and measuring the interferometric signal, a phase shift of $0.19\pi \pm 0.03$ radians was directly extracted [Sta+24]. The process was shown to be nonlinear in power, and to saturate at the few photon level (although not yet at the single photon level), confirming the quantum character of the interaction [Sta+24]. These results demonstrate that the phase shift induced by a single quantum emitter, combined with the interferometric geometry of a Mach-Zehnder device, provides a viable mechanism for controlling the routing of single photons between the output ports of the interferometer.

The relevance of this type of devices for the current development of quantum technologies is striking. The ability to route single photons between different spatial modes without external control fields is a long-sought capability for scalable photonic quantum networks. In classical optical networks, switching is performed by modulating the refractive index of a material with an intense control beam. At the single-photon level, this approach fails: the control field itself must consist of individual quanta, and the switching must rely on the nonlinear interaction between the control and target photons mediated by a single quantum emitter [CVL14]. Shomroni *et al.* demonstrated the experimental realization of such a scheme using a single ^{87}Rb atom coupled to a chip-based whispering-gallery-mode microresonator [Sho+14]. In

their device, a single reflected control photon toggles the internal state of the atom, deterministically switching the routing of subsequent target photons between the two output ports. The switch operates with a reflection of approximately 65% and a transmission of approximately 90%, with an average of about 1.5 control photons per switching event [Sho+14]. The underlying mechanism is the destructive interference between the incoming field and the field radiated by the atom into the forward direction, which forces the photon to be reflected backward [Sho+14].

The all-optical routing principle applied to single-photon wave packets directly connects to the physics investigated in the present thesis. In fact, the experiments just outlined have constituted the main motivation for the present work: a full theoretical description of a single-photon wavepacket transmitted through a quantum Mach–Zehnder interferometer. What do we mean by "quantum" here? Simple: a Mach-Zehnder interferometer in which a single quantum system is coupled to one of the two interferometer arms, such that the emitter-induced phase shift controls the interference condition at the second beam splitter, thereby determining the probability of detecting the single-photon at each of the two output ports. As shown in the analytical and numerical results of this work, when the pulse bandwidth is sufficiently narrow compared to the system linewidth, the single photon can be routed from the transmission port to the reflection port with near-unity efficiency — realizing, in a different geometry, the same functionality demonstrated by Shomroni *et al.* with the microresonator switch.

In perspective, a natural application domain for single-photon nonlinear elements is quantum machine learning implemented on photonic hardware. In fact, the concept of a quantum optical neural network (QONN) has been already shown to map the architecture of classical neural networks onto integrated photonic circuits, in which linear transformations are realized by meshes of tunable Mach-Zehnder interferometers and nonlinearities are provided by single-site optical interactions [Ste+19]. In the architecture proposed by Steinbrecher *et al.*, each layer consists of an m-mode linear optical unitary, $U(\vec{\theta})$, parameterized by arrays of beam splitters and phase shifters, followed by a single-site Kerr-type nonlinearity that applies a phase quadratic in the photon number [Ste+19]. The network is trained by optimizing the phase parameters to minimize a cost function constructed from input-output state pairs, and it has been shown to learn a range of quantum information processing tasks including quantum optical state compression, black-box quantum simulation, and the implementation of a one-way quantum repeater [Ste+19].

A practical concern in any physical realization of such networks is the effect of fabrication imperfections. Ewaniuk *et al.* investigated the performance of quantum photonic neural networks (QPNNs) in the presence of realistic imperfections, including unbalanced photon loss, imperfect routing, and weak nonlinearities [Ewa+23].

Their analysis shows that even with a sub-optimal $\pi/10$ effective Kerr nonlinearity, a network trained *in situ* can achieve an unconditional fidelity of 0.905 for a Bell-state analyzer, provided the network depth is sufficient [Ewa+23]. The Mach-Zehnder interferometer with an embedded quantum emitter studied in the present thesis constitutes precisely the type of building block required by these architectures: a device in which a tunable, photon-number-dependent phase shift is integrated within the interferometric unit cell.

Despite the experimental and theoretical advances outlined above, a complete theoretical treatment of a Mach-Zehnder interferometer operating with a single input photon and a single qubit — in its technological realization, a semiconductor quantum dot — as the active phase-control element appears to be missing from the literature. The existing theoretical framework of Shen and Fan [SF09] solves the single-photon transport problem for a waveguide coupled to a cavity containing a two-level atom, but does not embed this scattering process within an interferometric device. The experimental work of Staunstrup *et al.* [Sta+24], on the other hand, employs a Mach-Zehnder geometry to measure the phase shift, but uses a weak coherent laser rather than a true single-photon wavepacket, and it does not develop a full quantum-mechanical model of the interferometer response. Ultimately, the present thesis aims to fill this gap. Let us further emphasize that an experiment as the one proposed in this thesis (i.e., following the same scheme as the one in Fig. 1, but having genuine single-photon wavepackets at the input) has not been performed at time of writing, yet.

Here, a complete calculation of the response of a quantum Mach-Zehnder interferometer is developed, by modeling the quantum dot as a two-level system coupled directly to the waveguide and subsequently as a Jaynes-Cummings system in which the emitter is embedded in an optical cavity coupled in turn to the waveguide. For the two-level system, the single-photon scattering problem is solved analytically within the *time-bin framework*, yielding closed-form expressions for the transmission and reflection probabilities and the accumulated phase shift as a function of the detuning [Bun+25; SF09]. For the Jaynes-Cummings system, no analytical closed-form solution is available; the time-bin simulation constitutes the best tool to approach the problem, allowing the interferometer response to be explored as a function of the qubit-cavity coupling and the pulse bandwidth. The results show that in both configurations the single photon can be routed from the transmission port to the reflection port with near-unity efficiency when the pulse bandwidth is sufficiently narrow as compared to the system linewidth, with potential applications in the realization of high-efficiency optical switches at the single-photon level and as proof-of-concept building blocks for quantum photonic neural networks [Ste+19; Ewa+23].

The presentation of this thesis is organized as follows. Chapter 1 introduces the Mach-Zehnder interferometer in the classical and quantum-optical regimes, including the transfer-matrix formalism, the quantization of the electromagnetic field, and single-photon interference (in single-mode approximation). Chapter 2 develops the input-output theory for propagating single-photon pulses (i.e., spectrally distributed single-photon wavepackets), presenting the Hamiltonian formulation of the waveguide-QED system, and it introduces the time-bin formalism, as well as the Jaynes-Cummings model. Chapter 3 derives the analytic solution for the quantum MZI with a single qubit directly coupled to the waveguide. Finally, Chapter 4 presents the numerical time-bin simulation for the MZI with a single qubit coupled to the waveguide arm, validating it against the analytical results previously obtained, and then exploring the full parameter space of the Jaynes-Cummings configuration. Conclusions summarize the main findings and discuss several perspectives for future work.

Chapter 1

The Mach-Zehnder interferometer in Quantum Optics

1.1 The classical Mach-Zehnder interferometer

The optical Mach-Zehnder Interferometer (MZI) occupies a central position in both classical and quantum physics [SZ97]. In the classical regime, the MZI is widely employed for precision measurements of refractive indices, optical path differences, and phase perturbations induced by samples placed in one arm. Unlike the Michelson interferometer, which reflects the beams back along their original paths and recombines them at the same beam splitter [SZ97], the MZI employs a second, spatially distinct beam splitter for recombination. This forward-propagating geometry makes the device particularly suited to integrated photonic implementations, where the two arms correspond to waveguide channels connected by directional couplers. The MZI is a two-beam interferometric device that splits an incoming light field into two spatially separated paths and subsequently recombines them to produce an interference pattern at two distinct output ports. Its standard configuration consists of two beam splitters, labelled as BS_1 and BS_2, two perfectly reflecting mirrors M_1 and M_2, and a phase-shifting element placed in one of the two arms [Kri26]. A light beam entering through one input port of BS_1 is divided into two components that propagate along the upper and lower arms of the interferometer. The mirrors redirect the two beams so that they converge onto BS_2, where they are recombined. Two photodetectors, placed at the output ports of BS_2, register the resulting interference signal. A second input port at BS_1 is also present, even when no external field is injected through it. This port admits vacuum fluctuations in the quantum treatment of the device, a point that will become relevant in Section 1.3.

The geometry of the MZI can be understood as a closed, diamond-shaped optical circuit. BS_1 performs the initial amplitude division: two input fields with complex amplitudes α and β enter the first and the second ports of BS1, respectively. Si-

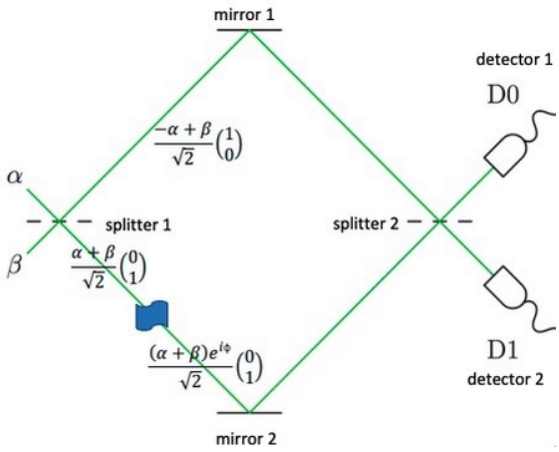

Figure 1.1: Schematic representation of the Mach-Zehnder interferometer. A light field enters through the input ports of beam splitter BS_1, which divides it into two beams propagating along the upper arm (via mirror M_1) and the lower arm (via mirror M_2). A phase-shifting element in the lower arm, depicted in the scheme as as a blue flag between BS1 and M2, imparts a relative phase $e^{i\varphi}$ before the beams are recombined at BS_2. Detectors D0 and D1 register the output signals. Adapted from [Kri26]

multaneously, both the beams are split into two parts each: as a consequence, a superposition of the two input amplitudes is created [Kri26]. These beams travel along the upper arm (via M_1) and the lower arm (via M_2) before arriving at BS_2. If a phase-shifting element is inserted in one of the arms, the beam traversing that arm acquires an additional phase factor $e^{i\varphi}$ relative to the other. The optical path-length difference between the two arms, together with any externally imposed phase shift, determines the relative phase φ that governs the interference condition at the output.

The analysis of the MZI in the classical wave picture, and the corresponding output intensities as a function of the phase difference φ, represent a classical two-beam interference exercise, which is mathematically derived in the following paragraph for completeness.

1.1.1 Operating principle of a classical MZI

The operation of the MZI is analyzed by tracking the complex field amplitude through each optical element. Two input fields with complex amplitudes, respectively α and β, are considered at the two input ports of BS_1, subject to the normalization condition $|\alpha|^2 + |\beta|^2 = 1$ [Kri26]. For a balanced (50:50) beam splitter, the action of BS_1 on the input vector is described by the linear transformation

$$\begin{pmatrix} E_{\text{upper}} \\ E_{\text{lower}} \end{pmatrix} = \frac{1}{\sqrt{2}} \begin{pmatrix} -1 & 1 \\ 1 & 1 \end{pmatrix} \begin{pmatrix} \alpha \\ \beta \end{pmatrix} = \frac{1}{\sqrt{2}} \begin{pmatrix} -\alpha + \beta \\ \alpha + \beta \end{pmatrix}, \tag{1.1}$$

such that each output arm carries an equal superposition of the two input amplitudes. Here, the minus sign assigned to the reflected component of α accounts for the π phase shift, corresponding to a factor of $e^{i\pi} = -1$, acquired upon reflection at the beam splitter interface. Introducing this relative phase is a necessary convention to ensure the unitarity of the transformation, thereby satisfying energy conservation.

The two beams propagate along the upper and lower arms, where the mirrors M_1 and M_2 redirect them toward BS_2 (ideally without losses, i.e., with unit reflectivity independent on the incidence angle). The phase-shifting element placed in the lower arm multiplies the corresponding amplitude by a factor $e^{i\varphi}$, while the upper arm is left unperturbed, 1.1. The field amplitudes arriving at BS_2 are therefore

$$\begin{pmatrix} E_{\text{upper}} \\ E'_{\text{lower}} \end{pmatrix} = \frac{1}{\sqrt{2}} \begin{pmatrix} -\alpha + \beta \\ (\alpha + \beta)\, e^{i\varphi} \end{pmatrix}. \tag{1.2}$$

The second beam splitter BS_2 recombines the two beams. Its action on the field amplitudes arriving from the two arms is given by

$$\begin{pmatrix} E_{\text{D0}} \\ E_{\text{D1}} \end{pmatrix} = \frac{1}{\sqrt{2}} \begin{pmatrix} 1 & 1 \\ 1 & -1 \end{pmatrix} \frac{1}{\sqrt{2}} \begin{pmatrix} -\alpha + \beta \\ (\alpha + \beta)\, e^{i\varphi} \end{pmatrix} = \frac{1}{2} \begin{pmatrix} -\alpha + \beta + (\alpha + \beta)\, e^{i\varphi} \\ -\alpha + \beta - (\alpha + \beta)\, e^{i\varphi} \end{pmatrix}, \tag{1.3}$$

where D0 and D1 label the two output ports [Kri26].

In a typical experimental configuration, light enters through a single input port. Setting $\beta = 0$ and $|\alpha|^2 = 1$ in Eq. (1.3), the output amplitudes reduce to

$$E_{\text{D0}} = \frac{\alpha}{2} \left(e^{i\varphi} - 1 \right), \qquad E_{\text{D1}} = -\frac{\alpha}{2} \left(e^{i\varphi} + 1 \right). \tag{1.4}$$

The intensities registered by the two detectors are obtained as the squared moduls of the output amplitudes. Using the identity $|e^{i\varphi} - 1|^2 = 2(1 - \cos\varphi) = 4\sin^2(\varphi/2)$ and the analogous expression for the sum, one finds

$$I_{\text{D0}} = I_0 \sin^2\!\left(\frac{\varphi}{2}\right), \qquad I_{\text{D1}} = I_0 \cos^2\!\left(\frac{\varphi}{2}\right), \tag{1.5}$$

where $I_0 = |\alpha|^2$ is the input intensity. The total output intensity satisfies $I_{\text{D0}} + I_{\text{D1}} = I_0$ for any value of φ, as required by energy conservation.

Equations (1.5) encode the full interference behaviour of the device. When $\varphi = 0$ (or any even multiple of π), all the light exits through D1 and none reaches D0: the interferometer is set at a bright fringe for one port and a dark fringe for the other. When $\varphi = \pi$ (or any odd multiple), the situation is reversed. For intermediate values of the phase shift the intensity is distributed between the two detectors continuously. This phase-dependent redistribution of the output intensity is the operating principle behind all interferometric sensing and switching applications of the MZI [SZ97].

1.1.2 Transfer-matrix formalism for the classical MZI

The behaviour of the MZI can be cast in a compact algebraic form by representing each optical element as a 2×2 matrix that acts on a two-component column vector of field amplitudes. Let the state of the field at any cross-section of the interferometer be described by the vector

$$\mathbf{E} = \begin{pmatrix} E_{\text{upper}} \\ E_{\text{lower}} \end{pmatrix}, \tag{1.6}$$

where E_{upper} and E_{lower} denote the complex amplitudes in the upper and lower arms, respectively. Each optical component maps an input vector to an output vector through multiplication by a transfer matrix, so the overall transformation of the interferometer is obtained as an ordered product of the individual matrices.

The first beam splitter BS_1 is characterized by the matrix

$$M_{\text{BS}_1} = \frac{1}{\sqrt{2}} \begin{pmatrix} -1 & 1 \\ 1 & 1 \end{pmatrix}, \tag{1.7}$$

which encodes the fact that the reflected component acquires a π phase shift while the transmitted component does not [Lou00; GAF10]. The input beams α and β entering through the two ports of BS_1 are represented as $\mathbf{E}_{\text{in}} = (\alpha,\, \beta)^T$, with the normalisation $|\alpha|^2 + |\beta|^2 = 1$. After the splitting, the field vector becomes

$$\mathbf{E}_{\text{after BS}_1} = M_{\text{BS}_1}\, \mathbf{E}_{\text{in}} = \frac{1}{\sqrt{2}} \begin{pmatrix} -\alpha + \beta \\ \alpha + \beta \end{pmatrix}. \tag{1.8}$$

A phase-shifting element placed in one of the two arms is described by a diagonal matrix. If the phase shifter sits in the lower arm and introduces a phase φ, the corresponding matrix reads

$$M_{\text{PS}} = \begin{pmatrix} 1 & 0 \\ 0 & e^{i\varphi} \end{pmatrix}. \tag{1.9}$$

An analogous expression holds when the phase shifter is placed in the upper arm: the diagonal entries are simply exchanged. The mirrors M_1 and M_2 redirect the beams towards BS_2 without altering the amplitudes, so their effect reduces to the identity in this idealised treatment. The second beam splitter BS_2 is described by

$$M_{\text{BS}_2} = \frac{1}{\sqrt{2}} \begin{pmatrix} 1 & 1 \\ 1 & -1 \end{pmatrix}. \tag{1.10}$$

Note that BS_1 and BS_2 are represented by different matrices; physically, this reflects the fact that the two beam splitters are traversed in opposite senses with respect to the propagation direction of the reflected beam.

The total transfer matrix of the MZI is the ordered product

$$M_{\mathrm{MZI}} = M_{\mathrm{BS}_2}\, M_{\mathrm{PS}}\, M_{\mathrm{BS}_1}. \tag{1.11}$$

Carrying out the multiplication explicitly yields

$$M_{\mathrm{MZI}} = \frac{1}{2}\begin{pmatrix} -(1-e^{i\varphi}) & (1+e^{i\varphi}) \\ -(1+e^{i\varphi}) & (1-e^{i\varphi}) \end{pmatrix}. \tag{1.12}$$

For a single input beam entering port 1 only ($|\alpha|^2 = 1$, $|\beta|^2 = 0$), the output amplitudes at detectors D0 and D1 are obtained from the first column of M_{MZI}. The detection probabilities reduce to

$$P(\mathrm{D0}) = \left|\frac{-(1-e^{i\varphi})}{2}\right|^2 = \sin^2\!\left(\frac{\varphi}{2}\right), \qquad P(\mathrm{D1}) = \left|\frac{-(1+e^{i\varphi})}{2}\right|^2 = \cos^2\!\left(\frac{\varphi}{2}\right), \tag{1.13}$$

which are identical to the results derived previously through the sequential application of the individual beam-splitter transformations. The matrix formulation, however, has a distinct practical advantage: it allows the transfer function of complex multi-element configurations to be built up by simple matrix multiplication.

The transfer-matrix formalism presented here provides the algebraic foundation upon which the quantum-mechanical treatment of the MZI will be constructed. In the quantum description, the complex field amplitudes are promoted to annihilation operators, and the beam-splitter matrices become unitary input–output relations for bosonic modes; this transition is the subject of Section 1.3.

1.2 Quantization of the electromagnetic field

A single mode of the free electromagnetic field oscillates at angular frequency ω determined by the dispersion relation $\omega = c\,|\mathbf{k}|$, where $\mathbf{k}$ is the wave vector. The total energy stored in such a mode, integrated over the quantisation volume V, can be written in terms of a dimensionless complex amplitude $\alpha(t)$ as [Lou00; GAF10]

$$H = \hbar\omega\,|\alpha(t)|^2. \tag{1.14}$$

The variable α encodes both the magnitude and the phase of the field, and its equation of motion, $\dot{\alpha} = -\mathrm{i}\omega\,\alpha$, describes a simple harmonic oscillation. This classical structure is made explicit by separating α into its real and imaginary parts through two real variables Q and P,

$$\alpha = \frac{1}{\sqrt{2\hbar}}\big(Q + \mathrm{i}\,P\big), \tag{1.15}$$

so that the Hamiltonian becomes

$$H = \frac{\omega}{2}\big(Q^2 + P^2\big). \tag{1.16}$$

This is the Hamiltonian of a one-dimensional harmonic oscillator with unit mass and frequency ω. Hamilton's equations, $\dot{Q} = \omega P$ and $\dot{P} = -\omega Q$, reproduce the original field dynamics, which confirms that Q and P are canonically conjugate variables.

The transition to quantum mechanics follows the standard canonical prescription: Q and P are promoted to Hermitian operators satisfying $[\hat{Q}, \hat{P}] = \mathrm{i}\hbar$, and the complex amplitude α is replaced by the annihilation operator

$$\hat{a} = \frac{1}{\sqrt{2\hbar}}\big(\hat{Q} + \mathrm{i}\,\hat{P}\big), \tag{1.17}$$

together with its adjoint, the creation operator $\hat{a}^\dagger$ [Lou00]. From the commutator of $\hat{Q}$ and $\hat{P}$ it automatically follows that

$$[\hat{a},\, \hat{a}^\dagger] = 1, \tag{1.18}$$

which is the fundamental bosonic commutation relation of quantum optics. The quantized Hamiltonian, expressed through these operators, reads

$$\hat{H} = \hbar\omega\left(\hat{a}^\dagger\hat{a} + \frac{1}{2}\right), \tag{1.19}$$

i.e., the quantized Hamiltonian operator for a simple harmonic oscillator of fundamental frequency ω. We further notice that the additional constant $\hbar\omega/2$ with respect to the classical expression in Eq. (1.14) represents the zero-point energy of the harmonic oscillator: it reflects the fact that the ground state of the quantized oscillator possesses a residual, irreducible energy even when no photons are present in the field [SZ97], which is a remarkable result of quantum theory.

Although the discussion has been focussing on a single mode, so far, the quantization scheme naturally extends to the full electromagnetic field spectrum. In fact, each mode of the continuous spectrum, which can be labelled by its wave vector $\mathbf{k}$ and polarisation λ, is associated with its own independent pair of creation and destruction operators, respectively $\hat{a}_{\mathbf{k}}$ and $\hat{a}^\dagger_{\mathbf{k}}$, while the quantized electric field operator becomes a sum (or, better, an integral) over all such modes. In the absence of nonlinear effects, understanding the basic physics of the single harmonic oscillator means understanding also the full quantized electromagnetic field.

Coming back to the single-mode field, the product $\hat{n} = \hat{a}^\dagger\hat{a}$ is a Hermitian oper-

ator called the number operator. Its eigenvalue equation,

$$\hat{n}\,|n\rangle = n\,|n\rangle, \qquad n = 0,\, 1,\, 2,\, \ldots \tag{1.20}$$

defines the Fock states (or photon-number states) $|n\rangle$, which form a complete orthonormal basis for the Hilbert space of the single mode oscillator [SZ97], i.e.,

$$\langle m|n\rangle = \delta_{mn}, \qquad \sum_{n=0}^{\infty} |n\rangle\langle n| = \mathbb{1}. \tag{1.21}$$

In terms of the number operator, the Hamiltonian in Eq. (1.19) can be simply written as $\hat{H} = \hbar\omega\,(\hat{n} + 1/2)$, such that its energy eigenvalues are simply given as $E_n = (n + 1/2)\,\hbar\omega$. The quantum number is an integer n, which is simply interpreted as the number of photons occupying the mode.

The action of the operators $\hat{a}$ and $\hat{a}^\dagger$ on a Fock state is straightforwardly derived from the commutation relation (1.18), and it reads

$$\hat{a}\,|n\rangle = \sqrt{n}\,|n-1\rangle, \qquad \hat{a}^\dagger\,|n\rangle = \sqrt{n+1}\,|n+1\rangle\,. \tag{1.22}$$

The operator $\hat{a}$ removes one photon from the field, $\hat{a}^\dagger$ adds one. This is why they are called annihilation and creation operators, respectively. Repeated application of $\hat{a}^\dagger$ to the ground state generates the entire Fock basis of number states, expressed as:

$$|n\rangle = \frac{(\hat{a}^\dagger)^n}{\sqrt{n!}}\,|0\rangle. \tag{1.23}$$

The state $|0\rangle$, called the vacuum, contains no photons. It is defined by the condition $\hat{a}\,|0\rangle = 0$, and its eigenenergy $E_0 = \hbar\omega/2$ is entirely due to zero-point fluctuations. Although the expectation value of the electric field vanishes in the vacuum, $\langle 0|\hat{E}|0\rangle = 0$, its variance does not[Lou00; SZ97]:

$$\langle 0|\hat{E}^2|0\rangle = 2\,|\mathscr{E}|^2\left(\frac{1}{2}\right) \neq 0\,, \tag{1.24}$$

in which $\mathscr{E} = (\hbar\omega/2\varepsilon_0 V)^{1/2}$ is the single-photon field amplitude. These vacuum fluctuations have measurable consequences — they enter the second input port of a beam splitter whenever it is left open, as it will explicitly appear in the quantum treatment of the MZI developed in Sec. 1.3.

The single-photon state $|1\rangle = \hat{a}^\dagger|0\rangle$ describes a field that carries exactly one quantum of energy, with total eigenenergy given by $E_1 = 3\hbar\omega/2$, and it is the state of primary interest for the single-photon interference experiments discussed in the remainder of this chapter.

1.3 Quantized description of the beam splitter

In the quantum description of the beam splitter operation, each input and output port is associated with a single bosonic mode of the electromagnetic field. For example, two independent input modes, described by annihilation operators $\hat{a}$ and $\hat{b}$, enter the device from opposite sides; the two output modes are then described by two further operators, respectively $\hat{c}$ and $\hat{d}$, as they emerge after the interaction. A scheme of the relevant degrees of freedom is represented in Fig. 1.2 The beam splitter is characterized by a single parameter, η, called the *transmissivity*, which essentially quantifies the fraction of the input intensity that is transmitted through the beam splitter [GK23; Lou00].

In the Heisenberg picture, the beam splitter acts as a linear transformation that maps the input operators onto the output operators. The transformation explicitly reads

$$\hat{c} = \sqrt{\eta}\,\hat{a} + \sqrt{1-\eta}\,\hat{b}, \tag{1.25}$$

$$\hat{d} = \sqrt{\eta}\,\hat{b} - \sqrt{1-\eta}\,\hat{a}\,, \tag{1.26}$$

in which the relative minus sign accounts for the π phase shift acquired upon reflection at one of the two surfaces [Lou00][Jac23]. In matrix notation, the transformation can be straightforwardly respresented as

$$\begin{pmatrix} \hat{c} \\ \hat{d} \end{pmatrix} = \begin{pmatrix} \sqrt{\eta} & \sqrt{1-\eta} \\ -\sqrt{1-\eta} & \sqrt{\eta} \end{pmatrix} \begin{pmatrix} \hat{a} \\ \hat{b} \end{pmatrix} . \tag{1.27}$$

The 2×2 matrix must be unitary, since the output modes are required to satisfy the same bosonic algebra as the input modes. Such a condition can be verified directly by direct substitution. As an example, the commutator of $\hat{c}$ with its adjoint gives

$$[\hat{c},\,\hat{c}^\dagger] = \eta\,[\hat{a},\hat{a}^\dagger] + (1-\eta)\,[\hat{b},\hat{b}^\dagger] = \eta + (1-\eta) = 1\,, \tag{1.28}$$

in which the the cross terms vanish because $\hat{a}$ and $\hat{b}$ belong to independent modes, and so $[\hat{a},\hat{b}^\dagger] = 0$. An identical calculation yields $[\hat{d},\hat{d}^\dagger] = 1$. The output modes must also be mutually independent. In fact, the commutator between the two different outputs is

$$[\hat{c},\,\hat{d}^\dagger] = \sqrt{\eta(1-\eta)}\,[\hat{a},\hat{a}^\dagger] - \sqrt{\eta(1-\eta)}\,[\hat{b},\hat{b}^\dagger] = 0, \tag{1.29}$$

which confirms that $\hat{c}$ and $\hat{d}$ describe two independent bosonic modes, as required. All remaining commutators ($[\hat{c},\hat{d}]$, etc.) vanish as well. Therefore, the beam-splitter transformation is a legitimate canonical transformation: it preserves the full bosonic commutation algebra.

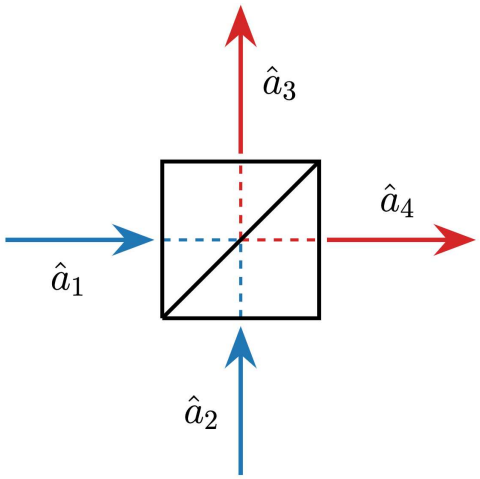

Figure 1.2: Schematic representation of a quantum beam splitter element[Jac23]. Two input modes impinge on the device from independent directions, while two output modes emerge after the interaction. Solid arrows denote transmitted components, dashed arrows denote reflected components. The diagonal line represents the partially reflecting surface characterized by the transmissivity, η. In the notation adopted in the text, operators are changed as $\hat{a}_1 \to \hat{a}$, $\hat{a}_2 \to \hat{b}$ (input modes) and $\hat{a}_3 \to \hat{d}$, $\hat{a}_4 \to \hat{c}$ (output modes).

From a physical standpoint, the unitarity of the transformation guarantees photon-number conservation. An equivalent way to state this fact is the following: the total number operator is the same before and after the beam splitter, i.e.,

$$\hat{c}^\dagger \hat{c} + \hat{d}^\dagger \hat{d} = \hat{a}^\dagger \hat{a} + \hat{b}^\dagger \hat{b}\,. \tag{1.30}$$

No photons are created or destroyed by the device, they are only redistributed between the two output channels.
An equivalent formulation of the quantized beam splitter is related to the definition of a Hamiltonian and a time evolution operator associated to the given transformation. In fact, it is easy to show that the relations (1.25)–(1.26) can also be derived from a two-mode interaction Hamiltonian of the form $\hat{H}_{\mathrm{BS}} \propto (\hat{a}^\dagger \hat{b} + \hat{b}^\dagger \hat{a})$, which describes the coherent exchange of excitations between the two modes [SZ97; Jac23; GK23]. The unitary operator generated by this Hamiltonian, $\hat{U} = \exp\!\left[-\mathrm{i}\hat{H}_{\mathrm{BS}} t/\hbar\right]$, acts on the input operators through the transformations $\hat{c} = \hat{U}^\dagger \hat{a}\, \hat{U}$ and $\hat{d} = \hat{U}^\dagger \hat{b}\, \hat{U}$, thus recovering precisely the linear relations above.

On the other hand, the Heisenberg-picture formulation of Eqs. (1.25)–(1.26) has a clear structural parallel with the classical transfer-matrix description developed in Sec. 1.1: the 2×2 matrix in Eq. (1.27) plays the same algebraic role as the classical beam-splitter matrices, M_{BS_1} and M_{BS_2}, but now the entries of the column vector are field operators rather than complex amplitudes.

The most common configuration encountered in interferometric setups is the bal-

anced beam splitter, which is formally obtained by setting $\eta = 1/2$ in the expressions above. The input–output relations derived in the previous subsection reduce to

$$\hat{c} = \frac{1}{\sqrt{2}}\big(\hat{a} + \hat{b}\big), \qquad \hat{d} = \frac{1}{\sqrt{2}}\big(\hat{b} - \hat{a}\big), \tag{1.31}$$

so that each output mode receives equal contributions from both inputs. The transmission and reflection probabilities are identical, and the relative π-phase shift between the two terms is preserved by the unitarity constraint discussed above [GK23].

Consider now a single photon entering the beam splitter from the port described by the operator $\hat{a}$, while the port described by the operator $\hat{b}$ is left in the vacuum state, such that the input state is described by $|1\rangle_a|0\rangle_b$. Because the photon is an indivisible quantum of energy, it cannot be split into two half-photons at the outputs. Instead, the unitary evolution of the beam splitter places the photon in a coherent superposition of the two paths, according to the unitary transformation [MS16]:

$$\hat{U}\,|1\rangle_a|0\rangle_b = \sqrt{\eta}\,|1\rangle_a|0\rangle_b - \sqrt{1-\eta}\,|0\rangle_a|1\rangle_b \quad \xrightarrow{\eta=1/2} \quad \frac{1}{\sqrt{2}}\big(|1\rangle_a|0\rangle_b - |0\rangle_a|1\rangle_b\big). \tag{1.32}$$

The state on the right-hand side is a path superposition: a measurement performed at either output ports will register the full photon with probability 1/2, yet no fractions of a photon are ever detected. The vacuum input at port $\hat{b}$ is not a mere placeholder. Although no real photons enter through that port, the vacuum mode participates in the unitary mixing performed by the beam splitter and directly affects the quantum state of the output [GK23]. It is interesting to notice that omitting it from the description would inevitably break the unitarity of the transformation.

While probing the beam splitter with a single input photon gives results that are aligned with the classical description, somehow, a striking departure from any classical analogy appears when both input ports are simultaneously fed with a single photon, i.e., assuming the two-photon input state $|1\rangle_a|1\rangle_b$. A naïve argument based on independent coin flips would predict that in half of the events one photon exits from each port. However, the quantum calculation tells a different story. Expanding the product of the transformed creation operators and setting $\eta = 1/2$, one obtains:

$$\hat{U}\,|1\rangle_a|1\rangle_b = \frac{1}{\sqrt{2}}\big(|2\rangle_a|0\rangle_b - |0\rangle_a|2\rangle_b\big)\,. \tag{1.33}$$

This is a striking result: the two photons always leave the beam splitter together, i.e., they are both transmitted or both reflected, and the coincidence count at the two output ports vanishes. This *photon bunching* is a signature of the Hong–Ou–Mandel (HOM) effect, and it arises from destructive interference between the transmission–transmission and reflection–reflection amplitudes. The cancellation of the $|1,1\rangle$ com-

ponent has no classical counterpart, and it can actually be interpreted as one of the clearest experimental demonstrations of the bosonic nature of photons [GAF10; Jac23], very interestingly. We will not be concerned with the two-photon excitation scheme in this thesis, which might represent a future development of the work, in fact.

1.4 Single-photon interference in the MZI

The quantum description of the MZI is straightforwardly constructed by cascading the three unitary operations that a photon encounters along the device: the first beam splitter operator, $\hat{U}_{\mathrm{BS1}}$, then a phase shift acquired in one of the two arms, $\hat{U}_{\varphi}$, and finally the second beam splitter $\hat{U}_{\mathrm{BS2}}$. The total evolution operator thus reads [SZ97; GK23]

$$\hat{U}_{\mathrm{MZ}} = \hat{U}_{\mathrm{BS2}}\, \hat{U}_{\varphi}\, \hat{U}_{\mathrm{BS1}}\,. \tag{1.34}$$

We will now assume that a single photon is injected into the input port $\hat{a}$ while port $\hat{b}$ is initialized in its vacuum state, such that the overall initial state is $|1\rangle_a|0\rangle_b$. The first beam splitter, assumed to be balanced at $\eta = 1/2$, produces the path superposition already derived in Sect. 1.3:

$$\hat{U}_{\mathrm{BS1}}\,|1,0\rangle = \frac{1}{\sqrt{2}}\Big(|1,0\rangle - |0,1\rangle\Big)\,. \tag{1.35}$$

At this stage the photon has no definite path inside the interferometer; its state is in a coherent superposition of occupying the upper and the lower arm [MS16].

The component $|1,0\rangle$ propagates along the arm that contains the phase-shifting element: a path-length difference, or an external device, introduces a relative phase φ through the operator $\hat{U}_{\varphi} = e^{i\varphi\,\hat{a}^{\dagger}\hat{a}}$, whose generator is the photon-number operator of that mode [GK23]. Because $\hat{a}^{\dagger}\hat{a}$ returns 1 on $|1,0\rangle$ and 0 on $|0,1\rangle$, the state after the phase shifter becomes

$$\hat{U}_{\varphi}\,\frac{1}{\sqrt{2}}\Big(|1,0\rangle - |0,1\rangle\Big) = \frac{1}{\sqrt{2}}\Big(e^{i\varphi}\,|1,0\rangle - |0,1\rangle\Big)\,. \tag{1.36}$$

The two path components recombine at the second beam splitter. In the Mach–Zehnder geometry the light impinges on BS_2 from the opposite side with respect to BS_1, which exchanges the port that acquires the reflection phase. The resulting single-photon transformations are:

$$\hat{U}_{\mathrm{BS2}}\,|1,0\rangle = \frac{1}{\sqrt{2}}\Big(|1,0\rangle + |0,1\rangle\Big), \qquad \hat{U}_{\mathrm{BS2}}\,|0,1\rangle = \frac{1}{\sqrt{2}}\Big(|0,1\rangle - |1,0\rangle\Big). \tag{1.37}$$

Applying Eq. (1.37) to the state of Eq. (1.36) and collecting terms yields the output

state of the interferometer:

$$\hat{U}_{\mathrm{MZ}}\,|1,0\rangle = \frac{1}{2}\Big[\Big(e^{i\varphi}+1\Big)\,|1,0\rangle + \Big(e^{i\varphi}-1\Big)\,|0,1\rangle\Big]$$
$$= e^{i\varphi/2}\Big(\cos\frac{\varphi}{2}\,|1,0\rangle + i\sin\frac{\varphi}{2}\,|0,1\rangle\Big)\,. \tag{1.38}$$

The global phase $e^{i\varphi/2}$ carries no observable consequence. The detection probabilities at the two output ports follow immediately from the squared moduli of the coefficients[GK23]:

$$p(D_1) = \cos^2\frac{\varphi}{2}\,, \qquad p(D_2) = \sin^2\frac{\varphi}{2}\,. \tag{1.39}$$

When $\varphi = 0$ the photon exits deterministically from port D_1: constructive interference channels the full probability amplitude into one output while destructive interference suppresses the other. As φ is varied continuously, the click rates at the two detectors trace out complementary sinusoidal fringes. These expressions are formally identical to the classical intensity fractions derived in Sect. 1.1 for a coherent beam traversing the same interferometer [Kri26], yet they are produced here by individual quanta arriving one at a time, and can only have a probabilistic interpretation. The single photon, having no definite trajectory inside the interferometer, interferes with itself [MS16].

1.4.1 Interference and "which-path" information

The periodic phase-dependent fringes derived previously rely on the fact that no information is available about which of the two arms the single photon actually traversed. In fact, whenever the path becomes distinguishable, the interference disappears. A simple way to reveal the path is to remove the second beam splitter altogether, as schematically depicted in Fig. 1.3. In that configuration, only one component of the photon path state can reach each detector: the component travelling along the upper arm (U) is projected into D_1, while the one travelling along the lower arm (L) goes into D_2. Which-path information (WPI) is therefore known for every detection event, and each detector clicks with probability 1/2 irrespective of the phase φ [MS16].

The same suppression of fringes occurs when two orthogonal polarizers are inserted in the arms of the interferometer, one transmitting the vertical polarization and the other the horizontal one, respectively. The polarisation degree of freedom now tags each path with a distinguishable internal state, and the photon's path and polarisation become entangled. Since the two polarisation components are orthogonal, the cross terms that produce interference vanish: the detection probability at each output port becomes 1/4 per polarisation channel, and 1/2 in total, which is again independent of φ [MS16].

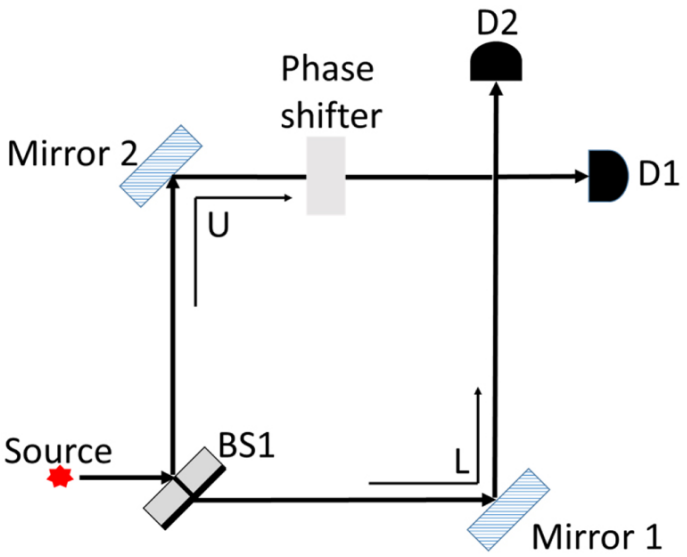

Figure 1.3: Schematic representation of the single-photon Mach-Zehnder interferometer with the second beam splitter removed. In this configuration, the which-path information is fully accessible: a click at detector D_1 corresponds deterministically to the photon having traversed the upper path (U), while a click at D_2 corresponds to the lower path (L). This predictability results in the complete loss of interference fringes. Adapted from [MS16].

These observations are particular instances of a general wave–particle duality relation. The Greenberger–Yasin inequality provides a quantitative bound on the trade-off between path knowledge and fringe contrast, and it is simply formulated as follows [GK23][SZ97]:

$$\mathcal{P}^2 + \mathcal{V}^2 \leq 1\,, \tag{1.40}$$

in which $\mathcal{P}$ is the path predictability, and $\mathcal{V}$ the fringe visibility. For a pure quantum state, the bound is saturated and the relation becomes an equality. In order to understand the origin of these expressions, we can refer to the standard definition of fringe visibility, $\mathcal{V} = (p_{\max} - p_{\min})/(p_{\max} + p_{\min})$, where $p_{\max}$ and $p_{\min}$ are the maximum and minimum detection probabilities at a given output port as the phase φ is varied [GK23]. For a Mach-Zehnder interferometer with a first beam splitter of transmissivity η and a balanced second beam splitter, the probability of the photon taking the transmitted or reflected path is η and $1-\eta$, respectively. The quantum interference between these two paths leads to an output detection probability of $p = 1/2 \pm \sqrt{\eta(1-\eta)}\cos\varphi$. Inserting the maximum and minimum values of this probability into the definition of $\mathcal{V}$ directly yields $\mathcal{V} = 2\sqrt{\eta(1-\eta)}$.

On the other hand, the path predictability $\mathcal{P}$ is defined as the absolute difference between the a priori probabilities of the photon taking the two paths [GK23], which translates to $\mathcal{P} = |\eta - (1-\eta)| = |2\eta - 1|$.

By squaring and adding these two fundamental quantities, one straightforwardly

recovers the Greenberger-Yasin equality: $\mathcal{P}^2 + \mathcal{V}^2 = (2\eta - 1)^2 + 4\eta(1 - \eta) = 1$. The two limiting cases are enlightening: a balanced beam splitter ($\eta = 1/2$) gives $\mathcal{P} = 0$ and $\mathcal{V} = 1$, corresponding to maximum interference (i.e., maximal visibility) and no path knowledge. On the contrary, a fully transmitting element ($\eta = 1$) gives $\mathcal{P} = 1$, and condequently $\mathcal{V} = 0$, corresponding to the knowledge of a well defined path for the photon, and hence a complete disappearance of interference fringes at the output of the MZI.

A remarkable consequence of this framework is that the loss of interference is not caused by an uncontrolled disturbance on the photon. If the which-path marker is measured in a basis that is conjugate to the one that encodes the path, the distinguishing information is erased, and interference reappears. This phenomenon is known as the *quantum erasure* [KH23; DNR98]. In the Mach–Zehnder setting, a qubit Q can be coupled to the interferometer such that its state records which arm the photon took: $|0\rangle_Q$ for the upper arm, and $|1\rangle_Q$ for the lower arm. After the phase shifter and the qubit interaction, the state then becomes $\Big(e^{i\varphi}|1,0\rangle|0\rangle_Q - |0,1\rangle|1\rangle_Q\Big)/\sqrt{2}$. Recombination at BS_2 then yields the joint photon–qubit state

$$|\Psi\rangle = \frac{1}{2}\Big[e^{i\varphi}\Big(|1,0\rangle + |0,1\rangle\Big)\,|0\rangle_Q \;+\; \Big(|1,0\rangle - |0,1\rangle\Big)\,|1\rangle_Q\Big]. \tag{1.41}$$

If the qubit is measured in the computational basis, $\{|0\rangle, |1\rangle\}$, the photon path is revealed and the marginal detection probabilities are $p(D_1) = p(D_2) = 1/2$, with no dependence on φ. If instead the qubit is measured in the conjugate basis, i.e., $|\pm\rangle = (|0\rangle \pm |1\rangle)/\sqrt{2}$, the which-path information is erased. The conditional detection probabilities then recover a phase-dependent pattern: for a qubit outcome $|+\rangle$ one obtains $p(D_1, +) = \cos^2(\varphi/2)/2$ and $p(D_2, +) = \sin^2(\varphi/2)/2$, while for $|-\rangle$ the roles of $\cos^2$ and $\sin^2$ are exchanged. The total probability, summed over both qubit outcomes, remains $1/2$ at each port. The fringes are visible only when the photon detection is conditioned on the qubit result. Interference has not been created or destroyed; it was present in the correlations all along and made observable by the choice of measurement basis.

1.5 Experimental implementations of MZI: from free-space to integrated photonics examples

The modular character makes the transfer-matrix approach particularly natural in integrated photonic implementations of the MZI. Different material platforms currently employ the MZI as an essential component for their functionalities, in particular silicon-on-insulator (SOI), silicon nitride (SiN), III-V compounds (e.g., AlGaAs integrated circuits), just to name the ones related to the semiconductor technology.

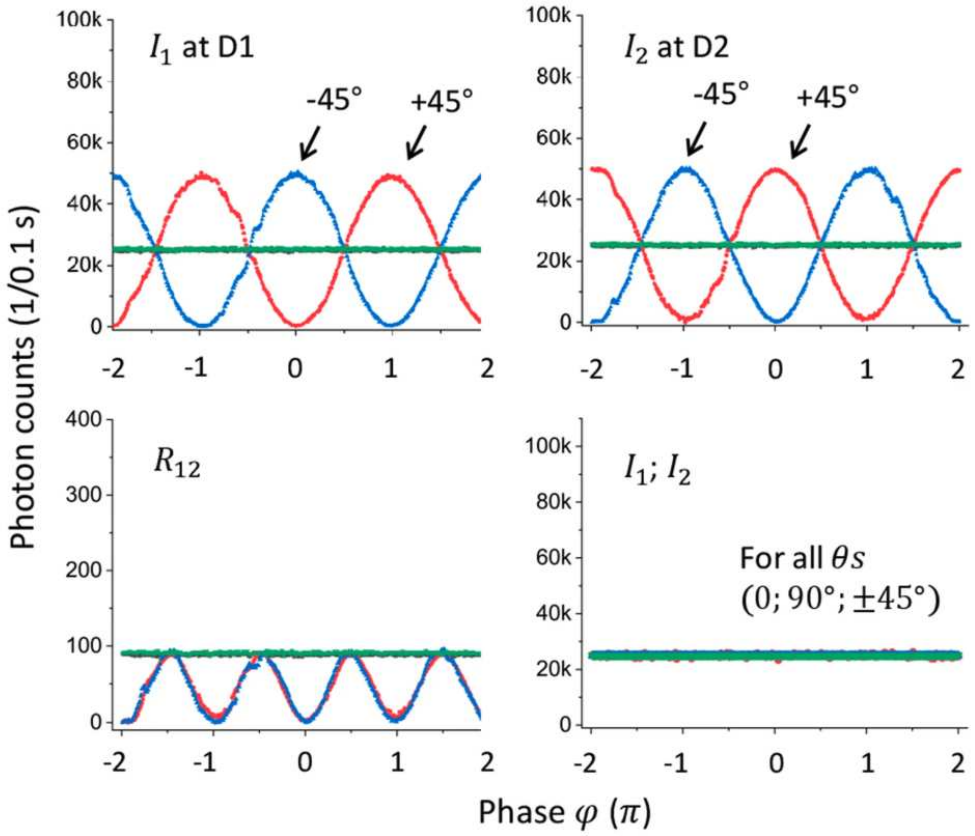

Figure 1.4: Experimental observation of classical macroscopic interference fringes in a free-space Mach-Zehnder interferometer. A continuous-wave laser is used as the coherent source. The complementary sinusoidal signals at the two output ports (D1 and D2) are recorded as a function of the relative phase shift induced by sweeping the voltage of a piezoelectric transducer (PZT). Adapted from [KH23].

In all these realizations, each beam splitter is typically realized by a directional coupler or a multimode interference (MMI) coupler, and the two arms are single-mode ridge waveguides connected by these coupling elements, as it will be shown in the following.

Before going into integrated configurations, and in order to provide a concrete example of the aforementioned free-space transfer-matrix theory in an actual experimental setup, we hereby refer to a standard classical MZI measurement, such as the one reported by Kim and Ham [KH23]. In their macroscopic free-space setup, a coherent continuous-wave (CW) laser is injected into the first bulk beam splitter. One of the mirrors is mounted on a piezoelectric transducer (PZT). By applying a sweeping voltage to the PZT, the optical path length of one arm is precisely varied at the sub-wavelength scale, continuously scanning the relative phase φ. Photodetectors placed at the two output ports (D1 and D2) record the intensities. As predicted by the classical intensity fractions derived in Eq. (1.5), the measured output signals exhibit perfectly complementary sinusoidal interference fringes as a function of the

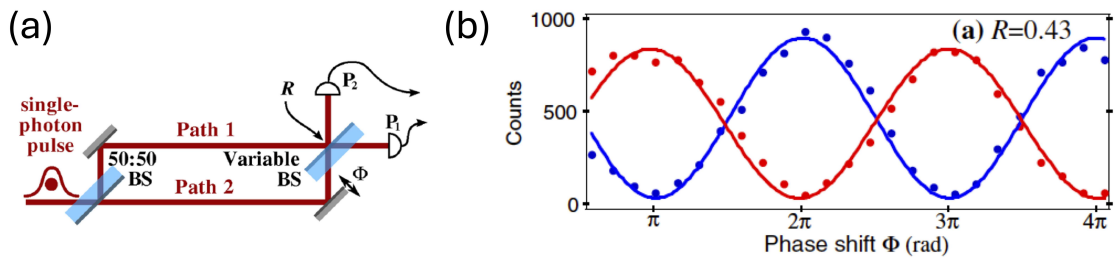

Figure 1.5: (a) Scheme of the free-space MZI with single-photon input: A single-photon pulse is sent into a MZI composed of a balanced input beam splitter (BS) and a variable output one (VBS). The reflection coefficient of this second VBS is an adjustable parameter (R); the single-photon photodetectors P1 and P2 allow to record single photon counts, thus building the interference pattern. (b) Interference fringes at the output ports measured for $R = 0.43$ as a function of the adjustable phase Φ, each point is recorded with 1.9 s acquisition time; detectors dark counts, corresponding to a rate of 60 Hz each, have been substracted to the data. Original panels adapted from Ref. [Jac+08].

applied PZT voltage. The experimental results are reported in Fig. 1.4, showing a nice correspondence with the theoretical prediction.

A very interesting extension of the experiment reported above is performed by employing quantum states of light, such as pure single photons instead of classical input beams. As a matter of fact, interference with individual quanta has been demonstrated even in educational settings [Bon21]. Here, we report another historical experiment performed by using a true source of single photons - i.e., a single nitrogen vacancy center in a diamond nanocrystal, emitting single photon streams with almost 90% efficiency [Jac+08]. A scheme of this experiment is shown in Fig. 1.5(a): a clock-triggered single-photon source based on the photoluminescence of a single N-V color center; the linearly polarized single-photon pulses are then directed to a polarization MZI, in which the input polarization beam splitter (BS) splits the light pulse into two spatially separated components of equal amplitudes, associated with the two orthogonal polarizations; the two beams then propagate in free space for 48 m, and recombined through a variable reflectivity beam splitter. The relative phase between the two paths can be adjusted by finely tuning the position of one of the two mirrors. The experimentally recorded interference fringes are beautifully shown in Fig. 1.5(b), also offering a striking visual demonstration of the wave-particle duality and the superposition principle for single photons.

The experimental demonstrations of wave interference shown above establish the baseline of the interferometric device both at the level of classical and quantum input states. However, bench-top free-space setups are highly sensitive to thermal drifts, air currents, and mechanical vibrations, thus requiring constant and rigorous realignment. This intrinsic instability represents the primary motivation for trans-

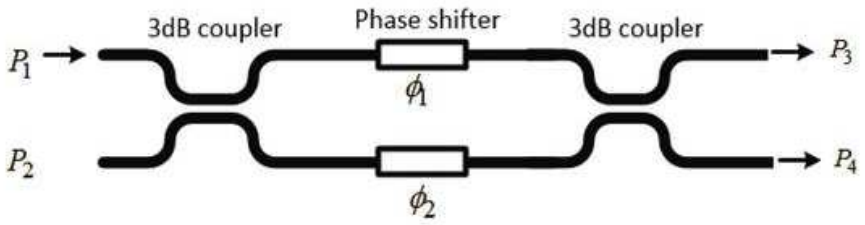

Figure 1.6: Schematic illustration of an integrated MZI cell based on two 3 dB directional couplers on a silicon-on-insulator platform. Two independent phase shifters ϕ_1 and ϕ_2 are placed in the upper and lower arm, respectively, allowing full control of the differential phase. P_1, P_2 denote the input ports and P_3, P_4 the output ports. Adapted from [Le18].

ferring interferometric geometries into monolithic, scalable on-chip architectures. In this respect, the correspondence between the free-space and waveguide descriptions is straightforward: the 2×2 coupler matrix replaces the beam-splitter matrix, and the waveguide phase accumulation replaces the free-space optical path-length difference. In integrated photonics implementations, two independent phase shifters (ϕ_1 and ϕ_2) may be inserted in both arms for individual tuning of the differential phase between the two arms [Le18]. A generic scheme implementing a tuneable MZI in integrated waveguides is shown in Fig. 1.6 From a technological standpoint, SOI or SiN platforms typically employ thermal phase shifters, which locally alter the refractive index of the material by heating it. A directional coupler in integrated photonic implementations operates through evanescent-field overlap between two closely spaced single-mode waveguides; its power splitting ratio is set by the coupling length and the gap between the neighboring waveguides (once the group velocity of the propagating beams is fixed).

Fabrication of directional couplers, however, requires tight dimensional control, because the coupling ratio is very sensitive to small variations of the gap width [Le18]. MMI-based couplers offer a practical alternative: they exhibit large fabrication tolerance, wide operation bandwidth and compact footprint, making them attractive for scalable photonic circuits. The SOI platform, for example, is particularly well suited for these devices. The large refractive-index contrast between the silicon core and the oxide cladding allows sharp waveguide bends and dense component integration, while full compatibility with complementary metal-oxide-semiconductor (CMOS) fabrication processes ensures scalability and low manufacturing cost [Le18]. On the SOI platform the MZI cell has been established as a basic building block for photonic circuits serving applications ranging from optical switching and filtering to quantum computing and reconfigurable unitary transformations. In the following, we show a few examples of MZI realized in different technological platforms: SOI, GaAs, and more recently LiNb.

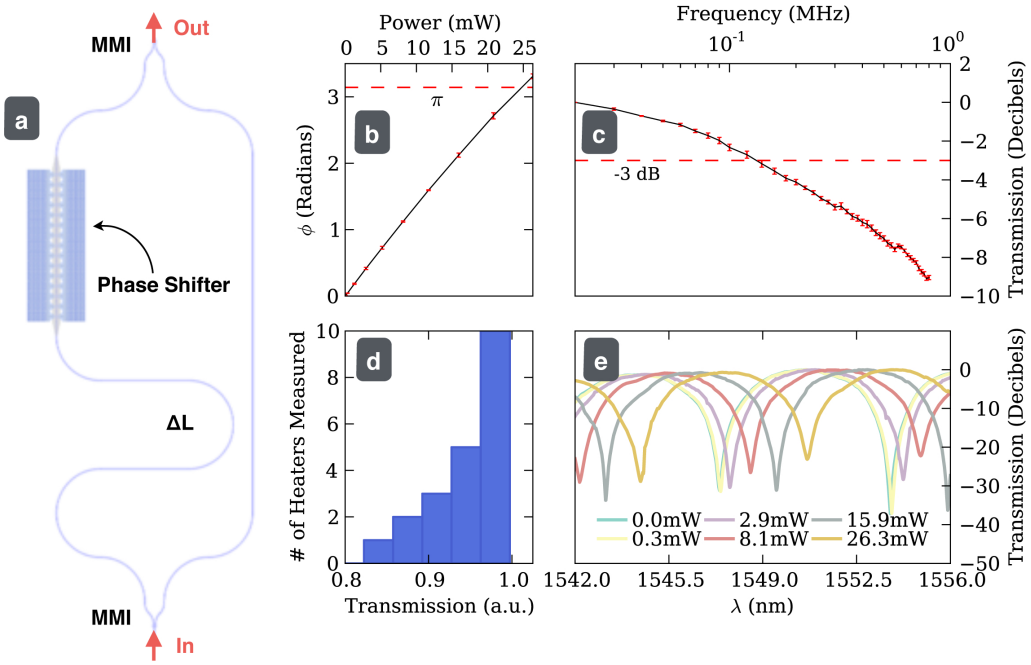

Figure 1.7: Experimental characterization of a thermo-optic phase shifter embedded in a SOI-based MZI: (a) Schematic layout of the unbalanced MZI test structure; (b) Measured phase shift versus dissipated power; (c) Average MZI amplitude response vs. driving frequency; (d) Histogram of the transmission measured across multiple devices on the same wafer; (e) Transmission spectra of the MZI recorded around 1550 nm (telecom band) for different applied heating powers, showing the continuous shift of the interference fringes. Original panels adapted from Ref. [Har+14].

We start this survey by showing a practical demonstration from Harris *et al.*, who have demonstrated an efficient thermo-optic phase shifter embedded in an unbalanced Mach-Zehnder interferometer [Har+14]. The schematic experimental configuration and the key results are summarized in Fig. 1.7. In this experiment, modulation is achieved by applying a voltage to a resistive heater, which changes the local temperature and thus the refractive index of the silicon waveguide in one of the two MZI arms. By recording the transmission spectra around the 1550 nm wavelength for different power dissipation levels, clear high-visibility sinusoidal interference fringes are observed as a function of wavelength. In addition, in Fig. 1.7 the continuous shift of the interference spectra as a function of the applied heating power can also be appreciated, which perfectly mirrors the classical macroscopic behavior. This confirms the reliability of the transfer-matrix description for on-chip components in SOI material platforms.

Along similar lines, another beautiful demonstration of MZI pattern formation at the output of an integrated device is reported in Fig. 1.8. This experiment, in particular, has been performed at the Quantum Photonics Laboratory here at the Department of Physics "A. Volta" of the University of Pavia. In fact, the relevance of these experiments stems from the fact that is performed in a radically

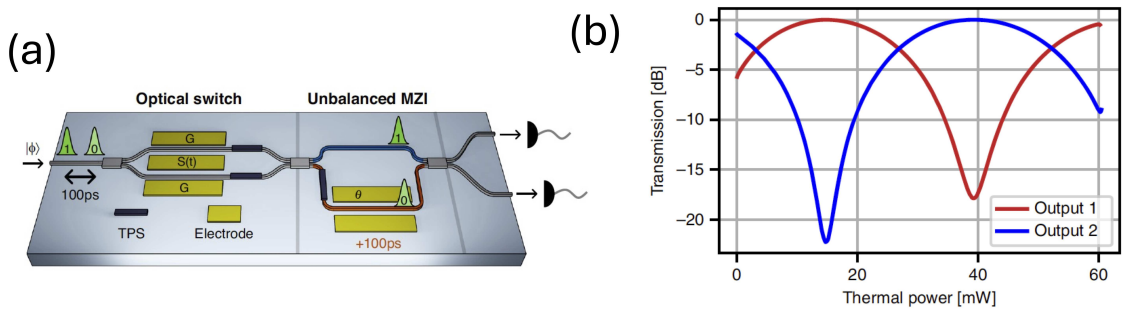

Figure 1.8: (a) Schematic of the thin-film LiNb-on-insulator (LNOI) platform with electro-optical modulators and thermal phase shifters; (b) linear characterization of the unbalanced MZI section of the device, showing nice interference fringes at the two output ports as a function of the relative phase accumulated between the two arms (tuning parameter: thermal power). Adapted from [Ber+26].

different material platform, Lithium Niobate (LiNb), quite popular in the integrated photonics literature lately thanks to its superior electro-optical nonlinear properties. Above all, this experiment is performed by injecting single-photon pulses, and in this respect it is the quantum photonic integrated counterpart of the result shown in Fig. 1.5. Single-photons are generated externally and injected into the device through edge coupling. Here we focus on the unbalanced MZI section of the device, whose linear characterization is shown in Fig. 1.8(b), where the nice interference fringes at the output ports are reported in the dB scale transmission (showing about 20 dB extinction ratios), as a function of the thermal power applied to the phase shifter and nicely reproducing the canonical MZI expectation.

Finally, we also report an interesting experiment realized in III-V semiconductor technology, namely GaAs waveguides operated in the transparency window (telecom band). The schematic MZI is shown in Fig. 1.9(a). In this case, the device is probed by simultaneously injecting pairs of single-photons in the two input arms [Wan+14]. In the MZI, the relative phase between the two propagating waveguides is finely tuned by an applied voltage through the electro-optic Pockels effect of GaAs. A nice interference figure is measured and the results are reported in Fig. 1.9. The unbalance between the two output ports is due to the non-perfect 50:50 beam splitting condition obtained from the two directional couplers. Overall, also in this case the integrated MZI is shown to the display the expected behavior as a function of the tuning knob (in this case, an external voltage).

1.5.1 The Quantum Mach–Zehnder Interferometer

We now go back to briefly outline the recent experimental results already mentioned in the Introduction, and representing the main motivation behind the present thesis. In particular, we hereby refer to a version of the MZI in which the classical phase

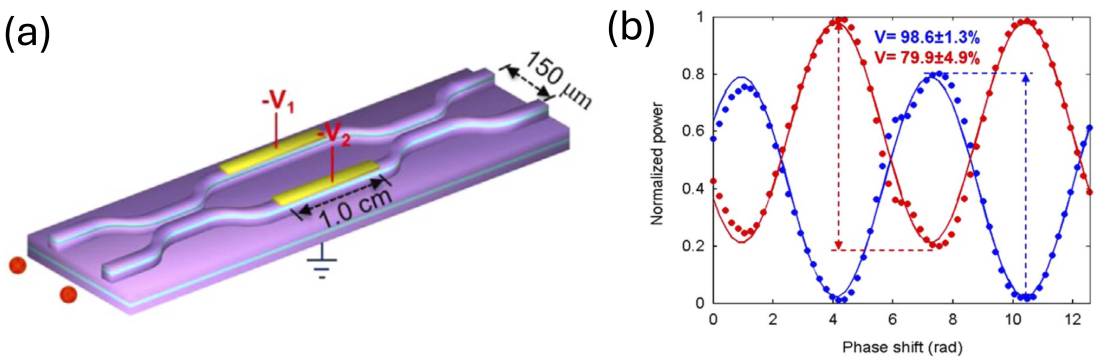

Figure 1.9: (a) Scheme of the GaAs on AlGaAs device with integrated MZI voltage controlled through Pockels effect; (b) measured output at the two ports, showing interference fringes typical of the MZI response. Panels are adapted from the results reported in Ref. [Wan+14].

shifter element that, as seen above, can be implemented in various ways according to the specific experimental setup employed, is replaced by a quantum system. This, in addition to the excitation of the system via a quantum state of light, justifies our definition of a quantum MZI. The key reference in this respect, as already introduced, is the one from Staunstrup *et al.*, summarized in Fig. 1.10, in which the first phase shift induced by a single quantum dot in a MZI has been reported.

From a theoretical point of view, the quantum-mechanical analysis of the integrated MZI is carried out with minimal modification as compared to the general treatment described in this chapter. First, the quantised electromagnetic field inside a single-mode waveguide of length L is described by the Hamiltonian [SK24]

$$\hat{H} = L \sum_n \int_{-\infty}^{\infty} \hbar\omega(\beta) \left[\hat{a}_n^\dagger(\beta)\, \hat{a}_n(\beta) + \frac{1}{2} \right] \frac{d\beta}{2\pi}\,, \tag{1.42}$$

in which $\beta = \frac{2\pi}{\lambda}$ is the wave vector along the waveguide axis, and $\omega(\beta)$ the corresponding angular frequency. For a single-mode guide, the index n reduces to a single term. A realistic single-photon excitation is modelled as a Gaussian wave packet with envelope $A(z) = (2\pi)^{-1/4} \exp(-z^2/4)$, which enters port 1 of the waveguide MZI while port 2 carries the vacuum state. The expectation value of the photon flux operator $\hat{F}(z,t) = v_g\, \hat{b}^\dagger(z,t)\, \hat{b}(z,t)$ at the two output ports is found to be [SK24]

$$\langle \hat{F}_3 \rangle = v_g\, |A(z - v_g t)|^2\, \sin^2\phi\,, \qquad \langle \hat{F}_4 \rangle = v_g\, |A(z - v_g t)|^2\, \cos^2\phi\,, \tag{1.43}$$

where v_g is the group velocity of the guided mode and ϕ the phase shift introduced in one arm. The sinusoidal dependence on ϕ reproduces the interference pattern obtained for the idealised single-mode treatment of Sect. 1.4, confirming that the waveguide MZI preserves the same quantum interference behaviour. The Gaussian

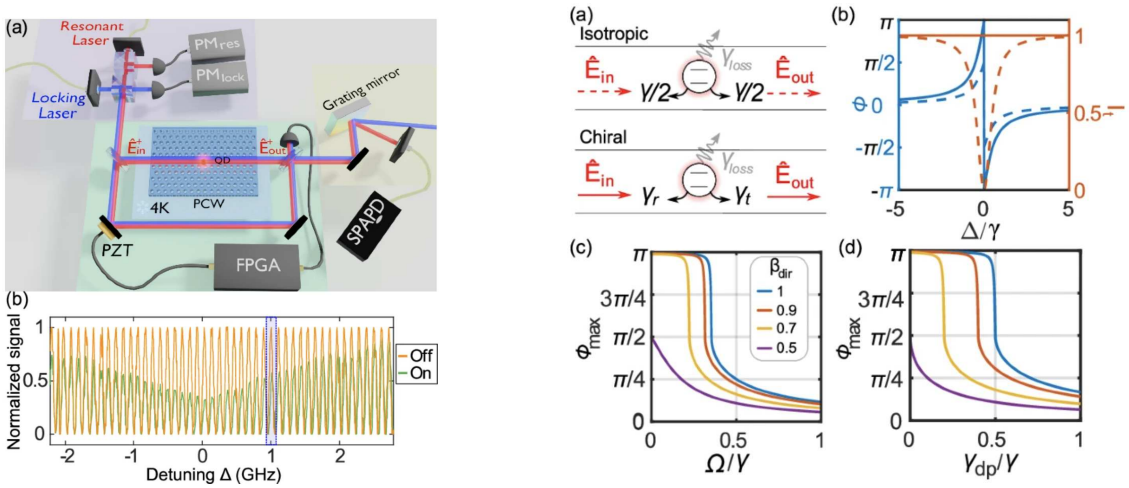

Figure 1.10: (i) Experimental setup for the interferometric measurement of the phase shift induced by a single quantum dot in a photonic crystal waveguide, cooled to 4 K inside a fibre-based Mach–Zehnder interferometer. (ii) Isotropic and chiral coupling configurations: panels (a) and (b) show the scattering geometry and the corresponding phase shift as a function of detuning for both cases, with a maximum of $\pi/2$ (isotropic) and π (chiral); panels (c) and (d) show the dependence of $\phi_{\max}$ on the driving Rabi frequency and the pure dephasing rate, respectively. Adapted from [Sta+24].

envelope $|A(z - v_g t)|^2$ modulates the flux in space and time without altering the phase-dependent splitting ratio.

The phase shift φ appearing in the interferometric equations derived so far has been treated as an externally tuneable parameter. A qualitatively different regime is reached when the phase is generated by the interaction of the guided photon with a single quantum emitter, such as a quantum dot or a trapped atom, embedded in one arm of the waveguide interferometer, as it happens, e.g., in Ref. [Sta+24]. In this configuration, the strong transverse confinement of the guided mode and the suppression of emission into radiative channels yield light–matter coupling efficiencies approaching unity [Sta+24]. The resulting optical nonlinearity operates at the level of individual photons: a single-photon wavepacket acquires a measurable phase shift upon scattering off the emitter, while a two-photon component experiences a different shift due to the saturation of the two-level transition. The theoretical framework for this class of photon-by-photon nonlinearities was established by Chang, Vuletić and Lukin [CVL14].

The steady-state transmission coefficient of a waveguide coupled to a single lifetime-limited quantum emitter with decay rate γ is characterised by the β-factor, defined as the fraction of the total emission funneled into the guided mode. In the isotropic (bidirectional) coupling geometry, the phase shift is expressed as $\phi = \arg(t)$, where t is the ratio of the output to the input field operators. On resonance, the

maximum achievable single-photon phase shift approaches $\pi/2$ in the limit $\beta \to 1$. For $\beta < 1$ the maximum phase shift occurs at a finite light–emitter detuning $\Delta = \pm\gamma\sqrt{1-\beta^2}/2$ and is given by [Sta+24]

$$|\phi|_{\max} = \arctan\left(\frac{\beta}{2\sqrt{1-\beta^2}}\right). \tag{1.44}$$

A chiral (unidirectional) coupling geometry, in which the emitter radiates preferentially into a single propagation direction, lifts this restriction: the maximum phase shift can in principle reach π, which is the condition required for deterministic quantum phase gates, see Fig. 1.10.

In fact, Staunstrup *et al.* reported the first direct interferometric measurement of such a phase shift in a nanophotonic platform. A single self-assembled InGaAs quantum dot was embedded in a GaAs photonic crystal waveguide and placed inside one arm of a ~ 3 m long fibre-based MZI, cooled to 4 K. By sweeping the frequency of a weak coherent probe across the quantum-dot resonance, and recording the interference signal at the output, the authors were able to infer a phase shift of $0.19\pi \pm 0.03$ radians. The process saturates at a mean photon flux of approximately $n_c \simeq 0.39$ photons interacting with the quantum dot during its lifetime, confirming the nonlinear character of the interaction at the single-photon level.

The remainder of this thesis is dedicated to a theoretical description of physical systems that can be practically realized as in the platform above: a semiconductor quantum dot deterministically coupled to a photonic crystal waveguide integrated into an on-chip MZI, and driven by a single-photon pulse. The theoretical framework developed in this chapter provides the foundation for the quantitative analysis presented in the following chapters.

Chapter 2

Input-output theory of propagating single-photon pulses coupled to quantum systems

2.1 Overview

In Chapter 1 we have shown that the response of a waveguide Mach–Zehnder interferometer is established by the phase difference acquired between the propagating photons in the two arms. When this phase originates from the scattering of a single photon off a localized quantum system, a theoretical framework connecting the incoming and outgoing propagating fields is required. This chapter develops such a theoretical framework, which will then be used in the rest of the thesis to analyse the behavior of such quantum Mach–Zehnder interferometer. In particular, Section 2.2 introduces the input–output formalism of Gardiner and Collett [GC85] and establishes the general relation between input and output field operators. Section 2.3 specializes the formalism to a two-level quantum emitter coupled to a one-dimensional waveguide, defining the corresponding full system Hamiltonian. In Section 2.4 we show that the same problem can be reformulated in terms of discrete temporal modes, and we applies this discretization to derive the single-photon scattering dynamics induced by coupling of the propagating mode with the localized quantum emitter, together with the corresponding input–output relation. This formulation is essential to be then able to generalize the formalism to the full quantum MZI. Finally, Section 2.5 introduces a more complex local quantum system, by including single-mode cavity coherently interacting with the emitter via the Jaynes–Cummings Hamiltonian, thereby setting the stage for the numerical analysis of the quantum MZI embedding such a quantum system in one of the two arms, which will be discussed in Chapter 4.

2.2 Input-output formalism for open quantum systems

In a classical or semiclassical setting, the phase φ accumulated along the MZI arms is an externally imposed parameter. A qualitatively different situation arises when the phase is generated by the coherent interaction of a propagating single photon with a localized quantum system — such as a two-level emitter or a cavity-coupled qubit — placed inside one arm of the interferometer. In this regime, the photon can be partially absorbed and re-emitted by the scatterer, acquiring a frequency-dependent phase shift that encodes the spectral response of the local system [CVL14]. Describing this process requires a framework that relates the quantum state of the outgoing field to that of the incoming field, while properly accounting for the irreversible coupling between the propagating mode and the localized degrees of freedom. The *input–output formalism* [GPZ92; ZG97; KM19], originally formulated by Gardiner and Collett [GC85], provides exactly this connection. In the following treatment, largely based on the above-mentioned seminal work [GC85], the formalism is first introduced in general; then, it is specialized to the waveguide quantum electrodynamics (WQED) setting, which is particularly relevant to the present thesis.

The starting point is a standard open quantum system approach: a localized system is assumed to be described by a free Hamiltonian, H_{sys}, and coupled to a continuum of bosonic modes that constitute the electromagnetic environment (bath). In the language of Gardiner and Collett, the total Hamiltonian takes the form

$$H = H_{\text{sys}} + H_f + H_{\text{int}} \,, \tag{2.1}$$

in which H_f describes the free propagation of the continuous field modes,

$$H_f = \hbar \int_{-\infty}^{+\infty} d\omega \, \omega \, b^\dagger(\omega) b(\omega) \,, \tag{2.2}$$

where $b(\omega)$ and $b^\dagger(\omega)$ are the bosonic annihilation and creation operators for the bath modes, satisfying the commutation relation $[b(\omega), b^\dagger(\omega')] = \delta(\omega - \omega')$. The term H_{int} accounts for the energy exchange between the localized system and the field. Assuming the system interacts via a generic operator c, the interaction is assumed to be linear in the field operators and to satisfy energy conservation. The latter condition is explicitly enforced by the *rotating-wave approximation* (RWA), leading to:

$$H_{\text{int}} = i\hbar \int_{-\infty}^{+\infty} d\omega \, \kappa(\omega) \left[c^\dagger b(\omega) - c \, b^\dagger(\omega) \right] \,, \tag{2.3}$$

where $\kappa(\omega)$ represents the frequency-dependent coupling strength. This is a standard assumption that is valid in the weak-coupling regime, according to which the

rapidly oscillating effects of energy non-preserving coupling operators—also commonly referred to as counter-rotating terms—average out to zero and are therefore neglected [For+19]. A third requirement, known as the first Markov approximation, demands that the coupling strength be independent of frequency. Physically, this holds whenever the bandwidth of the pulse largely exceeds any characteristic frequency scale of the system, such that the continuum acts as a memoryless reservoir. Under these conditions, the dynamics of the localized system are fully determined by a single parameter: the spontaneous emission rate γ into the guided mode.

The central result of the formalism is obtained by solving the Heisenberg equations of motion for the field and system operators under the assumptions stated above. Gardiner and Collett define an input field operator, $b_{\text{in}}(t)$, as the free evolution of the bath modes evaluated before the interaction with the localized quantum syste„ satisfying the bosonic commutation relation $[b_{\text{in}}(t),\, b_{\text{in}}^{\dagger}(t')] = \delta(t - t')$. Substituting this definition into the Heisenberg equation for a generic system operator A yields the quantum Langevin equation

$$\dot{A} = -\frac{i}{\hbar}\,[A,\, H_{\text{sys}}] - \left[A,\, c^{\dagger}\right]\left(\frac{\gamma}{2}\,c + \sqrt{\gamma}\,b_{\text{in}}(t)\right) + \left(\frac{\gamma}{2}\,c^{\dagger} + \sqrt{\gamma}\,b_{\text{in}}^{\dagger}(t)\right)[A,\, c]\,. \tag{2.4}$$

It is insightful to consider the simplest case of a single-mode cavity with annihilation operator a and resonance frequency ω_0, for which $[a,\, a^{\dagger}] = 1$ and $H_{\text{sys}} = \hbar\omega_0\, a^{\dagger}a$. In this situation, the Langevin equation reduces to

$$\dot{a} = -i\omega_0\, a - \frac{\gamma}{2}\,a - \sqrt{\gamma}\,b_{\text{in}}(t)\,, \tag{2.5}$$

where the three terms on the right-hand side describe, respectively, the free oscillation at frequency ω_0, the radiative damping at rate $\gamma/2$, and the driving by the input field.

An output field operator $b_{\text{out}}(t)$ is defined analogously by evolving the bath modes forward in time, past the interaction region [GC85]. From the Langevin equation one obtains the boundary condition

$$b_{\text{out}}(t) - b_{\text{in}}(t) = \sqrt{\gamma}\,c(t)\,, \tag{2.6}$$

which relates the outgoing field to the incoming field and the instantaneous state of the system. Eq. (2.6) is independent of the specific form of H_{sys} and applies to any localized system, harmonic oscillator, two-level emitter, or multilevel structure, coupled to the continuum under the three conditions stated above [GC85]. Once H_{sys} is specified and the Langevin equation solved for $c(t)$, the outgoing field is fully determined.

In the remainder of this chapter, the formalism is applied to a one-dimensional

waveguide coupled to a localized quantum system. The bath operators $b_{\text{in}}(t)$ and $b_{\text{out}}(t)$ of the general theory are replaced by the waveguide field operators $w(t)$ and their output counterpart, while the system operator c is identified with the appropriate transition operator of the scatterer. At this stage, it is necessary to formally introduce the quantum emitter as a two-level system (TLS). The system is characterized by two energy levels: a ground state $|g\rangle$ and an excited state $|e\rangle$. These are the eigenstates of the Pauli inversion operator σ_z, with eigenvalues -1 and $+1$, respectively, such that $\sigma_z = |e\rangle\langle e| - |g\rangle\langle g|$. The quantum transitions between these two energy levels are mediated by the atomic lowering (annihilation) and raising (creation) operators, defined as $\sigma = |g\rangle\langle e|$ and $\sigma^\dagger = |e\rangle\langle g|$, respectively.

For a two-level emitter, therefore, the generic local operator is replaced as $c \to \sigma = |g\rangle\langle e|$, and the input–output relation, Eq. (2.6), connects the incoming and outgoing photon amplitudes through the emitter dynamics. The following sections develop this protocol in detail: in Sec. 2.3 the full Hamiltonian of the waveguide-QED system is formulated, while in Sec. 2.4 the field is discretized into temporal modes, deriving the single-photon scattering solution together with the corresponding input–output relation in a discretized form.

The general input–output relation formally written in Eq. (2.6) remains valid when the localized system acquires a more complex internal structure. A configuration of direct relevance to this thesis is that of a single-mode cavity for the electromagnetic field coupled to the waveguide continuum, with a two-level emitter embedded inside the cavity and interacting with the cavity mode via the Jaynes–Cummings coupling Hamiltonian [SF09; OH17]. Since the waveguide field couples to the cavity, the system operator in Eq. (2.6) is identified with the cavity annihilation operator, $c \to a$, while the qubit degrees of freedom enter through the system Hamiltonian H_{sys} and modify the solution of the Langevin equation for $a(t)$. The formulation of this extended problem is the subject of Sec. 2.6.

2.3 Hamiltonian formulation for the waveguide-QED system

The simplest realization of a WQED system consists of a two-level system (TLS) interacting with a continuum of propagating modes confined to a one-dimensional waveguide. Despite its simplicity, this minimal model already captures the essential ingredients of photon scattering, spontaneous emission and interference effects in open quantum systems.

In its most general formulation, the quantum state of a traveling single-photon pulse

can be expressed as [Cic17]:

$$|\psi\rangle = \int d\nu\, \psi(\nu)\, w^\dagger(\nu)\, |\emptyset\rangle, \tag{2.7}$$

where $w^\dagger(\nu)$ denotes the creation operator of a photon with frequency ν, having units of $\sqrt{\text{time}}$. The function $\psi(\nu)$ represents the wavefunction of the pulse and carries the same units, ensuring normalization over the continuum of frequencies. Finally, $|\emptyset\rangle$ corresponds to the vacuum state of the waveguide, i.e., the state with no photons present.
Let us assume to have a generic system S described by a free Hamiltonian $\hat{H}_S$ and coupled to a continuum of bosonic modes (henceforth referred to as the "field"). In our case, we specialize the system S to a two-level emitter, whose free Hamiltonian reads

$$H_{\text{sys}} = \frac{\hbar\nu_0}{2}\, \sigma_z, \tag{2.8}$$

where ν_0 is the transition frequency between the ground and excited states and σ_z is the usual Pauli operator.

The free Hamiltonian of the field can be written as

$$H_f = \hbar \int d\nu\, \nu\, w^\dagger(\nu) w(\nu) \tag{2.9}$$

where $w(\nu)$ and $w^\dagger(\nu)$ are the annihilation and creation operators, respectively, for a photon of frequency ν. The integration extends over the entire continuous spectrum of the field (and the same convention applies to all similar integrals hereafter). The field operators satisfy the standard bosonic commutation relations $[\, w(\nu),\, w^\dagger(\nu')\,] = \delta(\nu - \nu')$ and $[\, w(\nu),\, w(\nu')\,] = [\, w^\dagger(\nu),\, w^\dagger(\nu')\,] = 0$.

This Hamiltonian describes a continuum of propagating modes confined within a one-dimensional waveguide, with each mode corresponding to a frequency component ν of the traveling single-photon pulse. In this framework, the total field energy is obtained by integrating over all possible frequency modes, each contributing an amount $\hbar\nu$ per photon occupation.

The total Hamiltonian of the system can thus be written as the sum of this three contributions:

$$H = H_{\text{sys}} + H_f + H_{\text{int}} \tag{2.10}$$

where, for the interaction between the field and a localized quantum system, such as a two-level system characterized by the transition operators $\sigma = |g\rangle\langle e|$ and $\sigma^\dagger = |e\rangle\langle g|$, we can write:

$$H_{\text{int}} = \hbar \int d\nu\, \left[g(\nu)\, \sigma^\dagger w(\nu) - g^*(\nu)\, \sigma\, w^\dagger(\nu) \right] \tag{2.11}$$

where $g(\nu)$ describes the strength of the coupling between the emitter and each individual mode. In a realistic system, the coupling coefficient $g(\nu)$ may vary with frequency due to the frequency dependence of the photonic density of states and the spatial field profile of the guided mode. However, since the two-level system typically interacts only with a narrow band of frequencies around its transition frequency ν_0, it is reasonable to approximate the coupling as frequency-independent, and we can set

$$g(\nu) = i\sqrt{\frac{\gamma}{2\pi}},$$

These assumptions allow for a Markovian continuum where the decay rate γ denotes the effective coupling rate between the emitter and the waveguide.

In the interaction picture, the field operators evolve in time as $w(\nu, t) = w(\nu)e^{-i\nu t}$, leading to the time-domain representation

$$w(t) = \frac{1}{\sqrt{2\pi}} \int d\nu \, w(\nu) e^{-i\nu t} \tag{2.12}$$

Accordingly, the interaction Hamiltonian becomes [Bun+25]:

$$H_{\text{int}}(t) = i\hbar\sqrt{\gamma} \, [\, \sigma^\dagger w(t) - \sigma w^\dagger(t) \,]. \tag{2.13}$$

This form is particularly convenient, as it removes the explicit frequency dependence of the coupling and it allows to describe the dynamics in terms of localized time modes interacting sequentially with the emitter.

By performing a Fourier transform of the spectral wavefunction $\psi(\nu)$, the single-photon state can equivalently be expressed in the time domain as:

$$|\psi\rangle = \int_{t_i}^{t_f} dt \, \xi^{(1)}(t) \, w^\dagger(t) |\emptyset\rangle, \tag{2.14}$$

where $\xi^{(1)}(t) = \frac{1}{\sqrt{2\pi}} \int d\nu \, \psi(\nu) e^{-i\nu t}$ is the temporal wavefunction of the pulse. The quantity $|\xi^{(1)}(t)|^2$, with units of inverse time, represents the photon flux at time t. Multiplying it by a small timestep Δt gives the probability of detecting the photon within the interval $[t, \, t + \Delta t]$.

A photon propagating in a one-dimensional waveguide is characterized by a dispersion relation between frequency and wavenumber, in general given by $\nu(k) = v_g(k)k$, where $v_g(k) = \frac{d\nu}{dk}$ is the group velocity of the guided mode. For an approximately linear dispersion, v_g can be taken as a constant value, such that time and position are directly related by $x = v_g t$. If the propagation velocity is taken to be the speed of light c (or set to unity in natural units), time and spatial coordinates become directly interchangeable through $t \leftrightarrow x/c$. Hence, under the assumption of linear dispersion, the modes $w(t)$ can be directly mapped to spatial modes of the

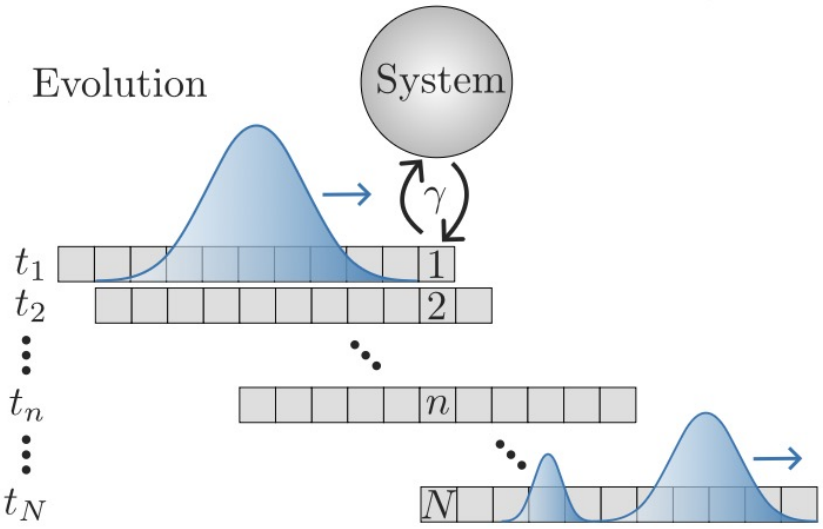

Figure 2.1: A single-photon pulse interacts with a localized quantum system, whose evolution is obtained by allowing each temporal bin to successively interact with the system one at a time. Adapted from [Bun+25].

propagating photon.
In this representation, the emitter interacts only with a single temporal mode $w(t)$ at each instant of time. Hence, the description no longer involves a continuum of frequency modes, but rather a time-dependent Hamiltonian acting locally in time. This reformulation greatly simplifies the physical picture, allowing us to describe the dynamics as a sequence of discrete time bins, each interacting with the localized system individually. Thus, one can simply think of the evolution of the time-binned modes as a moving conveyor belt, Fig.2.1.

In the next two sections, we describe the photon scattering process within the time-bin formalism mentioned above. This formulation provides a clear and intuitive picture of the scattering dynamics, as well as a convenient framework for numerical simulation.

2.4 Time-Bin Formalism and the Scattering Process

Before delving into the detailed derivation, it is important to explicitly state that the time-bin formalism and the associated numerical implementation discussed in this section are heavily inspired by the theoretical framework originally introduced by Heuck *et al.* [HJE20]. This approach was subsequently expanded in the Master's thesis of M. Bundgaard-Nielsen [Bun23] and formalized in the `WaveguideQED.jl` computational package [Bun+25].

Following this established methodology, the continuous single-photon state is initially discretized into a finite set of temporal modes of width Δt, each representing a localized portion (in time) of the wavepacket. In the continuous case, the field operator in the time domain is defined from Eq. (2.12), and it satisfies the canonical commutation relation $[\, w(t), w^\dagger(t') \,] = \delta(t - t')$. We now divide time into discrete intervals, or *time bins*, of width Δt:

$$t_k = k\,\Delta t, \qquad k = 1, 2, \ldots, N.$$

For each bin, we define a corresponding operator that collects the field information within the time interval $[t_k,\, t_k + \Delta t]$ [Gro+18][HJE20]:

$$w_k = \frac{1}{\sqrt{\Delta t}} \int_{t_k}^{t_k+\Delta t} dt\, w(t).$$

The prefactor $1/\sqrt{\Delta t}$ ensures that w_k is dimensionless and preserves the canonical commutation relations. Indeed, computing the commutator between two bins gives:

$$[\, w_j, w_k^\dagger \,] = \frac{1}{\Delta t} \int_{t_j}^{t_j+\Delta t} dt \int_{t_k}^{t_k+\Delta t} dt' \,[\, w(t), w^\dagger(t') \,] = \frac{1}{\Delta t} \int_{t_j}^{t_j+\Delta t} dt \int_{t_k}^{t_k+\Delta t} dt'\, \delta(t-t') = \delta_{jk}\,.$$

This is precisely the discrete bosonic commutation relation: each time bin behaves as an independent mode of the field. When moving from the continuous to the discrete picture, the continuous field operator $w(t_k)$ is replaced by the normalized discrete operator $w_k(t_k)/\sqrt{\Delta t}$, so that the commutation relations remain properly normalized.

This means that the continuous single-photon Fock state becomes

$$|\psi\rangle = \sum_{k=1}^{N} \sqrt{\Delta t}\, \xi(t_k)\, w_k^\dagger |\emptyset\rangle = \sum_{k=1}^{N} \sqrt{\Delta t}\, \xi(t_k)\, |1_k\rangle, \tag{2.15}$$

where we defined the time-bin state as $|1_k\rangle = w_k^\dagger|\emptyset\rangle$. The sum runs up to N, such that $N\Delta t$ corresponds to the total simulation time.

Figure 2.2 illustrates the numerical representation of a single-photon state discretized in time. Along the horizontal axis, each bin corresponds to a discrete time interval $[t_k,\, t_k + \Delta t]$. The operator $w_k^\dagger$ creates a photon within the corresponding time bin, so that each state $|1_k\rangle = w_k^\dagger|\emptyset\rangle$ represents a photon localized in the k-th interval. The overall single-photon state is then a coherent superposition of all these temporal modes, weighted according to the temporal envelope of the photon $\xi(t_k)$.

The discrete form of the interaction Hamiltonian can be written as

$$H_{\text{time}}(t) = \sum_k f_k(t)\, i\hbar \sqrt{\frac{\gamma}{\Delta t}} \left(\sigma^\dagger w_k - \sigma w_k^\dagger \right), \tag{2.16}$$

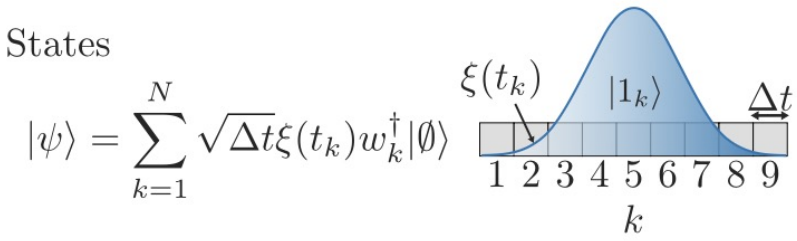

Figure 2.2: Numerical representation of the single-photon state in the time-bin formalism. Figure adapted from the original in Ref. [Bun+25].

where we defined:

$$f_k(t) = \begin{cases} 1, & t_k < t < t_k + \Delta t, \\ 0, & \text{otherwise.} \end{cases} \tag{2.17}$$

In this representation, the Hamiltonian remains constant within each time bin. This picture provides a clear and intuitive interpretation of the dynamics. The field can be viewed as a stream of photon bins that sequentially pass by the emitter, with only one bin interacting with the system at any given time, Fig.2.1.

2.4.1 Photon scattering from a two-level system

In the previous section, we introduced the time-bin formalism. We now apply it to derive the dynamics of a single-photon pulse scattering off a two-level emitter, following the derivation illustrated in [Bun23; HJE20].

The time evolution of the system follows from the Hamiltonian in Eq. (2.16) and the Schrödinger equation $i\hbar\partial_t|\psi\rangle = H|\psi\rangle$. Since the Hamiltonian remains constant within each time bin, we can define the interaction Hamiltonian for the k-th bin as:

$$H_k = i\hbar\sqrt{\frac{\gamma}{\Delta t}}\left(\sigma^\dagger w_k - \sigma w_k^\dagger\right). \tag{2.18}$$

The dynamics within each time interval $[t_{k-1}, t_k]$ are governed by the unitary evolution operator

$$U_k = e^{-\frac{i}{\hbar}H_k\Delta t} \tag{2.19}$$

Since $H_k \propto 1/\Delta t$, we expand the exponential up to first order in Δt:

$$U_k \simeq I - \frac{i\Delta t}{\hbar}H_k - \frac{(\Delta t)^2}{2\hbar^2}H_k^2$$

Keeping only terms to first order in Δt, the corresponding time-evolution operator is:

$$U_k = I + \sqrt{\gamma\Delta t}\,(\sigma^\dagger w_k - \sigma w_k^\dagger) - \frac{\gamma\Delta t}{2}\left[\sigma^\dagger\sigma\, w_k w_k^\dagger\right] \tag{2.20}$$

Note that we omitted the term $\propto \sigma\sigma^\dagger\, w_k^\dagger w_k$ because it results in terms proportional to $\Delta t^{\frac{3}{2}}$ when acting on states with the photon in the waveguide.

We consider the initial state where the emitter is in the ground state $|g\rangle$ and the waveguide contains a single-photon wavepacket with temporal envelope $\xi(t)$:

$$|\psi_0\rangle = \sum_{k=1}^{N} \sqrt{\Delta t}\, \xi(t_k)\, |g\rangle |1_k\rangle. \tag{2.21}$$

By recursively applying the unitary operators U_n to Eq. (14), we obtain the state after n time steps as:

$$|\psi_n\rangle = \sum_{k=n+1}^{N} \sqrt{\Delta t}\, \xi(t_k)\, |g\rangle |1_k\rangle + \sum_{k=1}^{n} \sqrt{\Delta t}\, \xi_{\text{out}}(t_k)\, |g\rangle |1_k\rangle + \psi_e(n)\, |e\rangle |\emptyset\rangle. \tag{2.22}$$

To clarify the physical meaning of this expression, it is essential to distinguish the time bins based on their index k relative to the current evolution step n. At time $t_n = n\Delta t$, the total state is composed of three distinct contributions. The temporal modes with $k \geq n+1$ represent the portion of the incoming wavepacket that is still approaching and has not yet interacted with the emitter; consequently, their probability amplitude remains defined by the original unperturbed envelope $\xi(t_k)$. Conversely, the modes with $k \leq n$ represent the portion of the field that has already passed the emitter. The light-matter interaction modifies their original state, giving rise to a new envelope function $\xi_{\text{out}}(t_k)$, which explicitly defines the scattered (output) field. Finally, the last term $\psi_e(n)$ is the excitation amplitude, representing the probability that the photon has been absorbed from the waveguide, leaving the localized system in the excited state $|e\rangle$.

Relating $\psi_e(n)$ to $\psi_e(n-1)$ leads to the following equation of motion:

$$\frac{d\psi_e(t)}{dt} = -\frac{\gamma}{2}\psi_e(t) + \sqrt{\gamma}\, \xi(t) \tag{2.23}$$

together with the well-known input–output relation [GC85]

$$\xi_{\text{out}}(t_{n+1}) = \xi(t_{n+1}) - \sqrt{\gamma}\, \psi_e(t_n) \tag{2.24}$$

In this case, the derivation of the scattered field is rather systematic. However, one could easily imagine more complex situations. These could involve, for instance, the presence of additional quantum systems coupled to the emitter, the inclusion of extra interaction terms in the Hamiltonian, or simply a frequency detuning between the waveguide pulse and the emitter transition.

In summary, the time-bin formalism provides an intuitive and powerful framework for describing the dynamics of single-photon scattering in one-dimensional

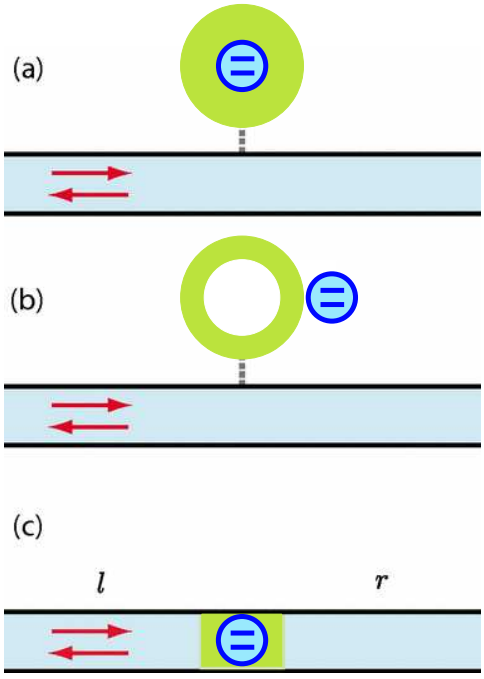

Figure 2.3: Coupling geometries for a cavity containing a two-level emitter interacting with a single-mode waveguide. (a) Side-coupled single-mode microcavity. (b) Side-coupled ring resonator. (c) Direct-coupled configuration. The system considered in this thesis corresponds to panel (a), where the waveguide couples exclusively to the cavity mode and the emitter interacts only with the confined field inside the resonator.

waveguides, laying the foundation for the numerical analysis presented in the next section.

2.5 Photon scattering from a cavity coupled single emitter: Jaynes–Cummings model

In the preceding sections, the localized system consisted of a bare two-level emitter coupled directly to the waveguide continuum. A different architecture arises when the emitter is embedded inside a single-mode optical cavity that is itself coupled to the waveguide, as schematically illustrated in Fig. 2.3 for different models. In all of the schematic examples, the propagating photon does not directly interact with the two-level system. Instead, it couples to the cavity mode, which in turn exchanges excitations with the emitter through the coherent light–matter interaction [SF09]. The system spectrum is therefore characterized by a hierarchy of energy scales: the cavity resonance frequency ω_c, the emitter transition frequency ω_0, the cavity–emitter coupling strength g, and the cavity decay rate into the waveguide κ. As

anticipated in Sec. 2.2, the input–output relation in Eq. (2.6) remains valid in this extended setting, with the system operator identified as the cavity annihilation operator a.

In the absence of the single-mode cavity, the localized system is fully described by the free Hamiltonian of the two-level emitter, $H_{\mathrm{TLS}} = \frac{\hbar\omega_0}{2}\,\sigma_z$, as introduced in Sec. 2.3. The inclusion of the cavity mode adds a bosonic degree of freedom — the confined electromagnetic mode at frequency ω_c — and a coherent coupling between this mode and the emitter. The Hamiltonian of the composite local system takes then the Jaynes–Cummings form (in RWA) [SF09; OH17]

$$H_{\mathrm{sys}} = \hbar\omega_c\, a^\dagger a + \frac{\hbar\omega_0}{2}\,\sigma_z + \hbar g\Big(\sigma_+ a + a^\dagger \sigma_-\Big)\,, \tag{2.25}$$

in which $a^\dagger$ and a are the creation and annihilation operators of the cavity mode satisfying $[a,\, a^\dagger] = 1$, and $\sigma_+ = |e\rangle\langle g|$, $\sigma_- = |g\rangle\langle e|$ are the raising and lowering operators of the emitter. The parameter g is the vacuum Rabi frequency, quantifying the rate of coherent excitation exchange between the cavity photon and the qubit. The coupling between the waveguide modes and the single-mode cavity is described by the interaction Hamiltonian [SF09; OH17]

$$H_{\mathrm{int}} = \hbar\sqrt{\frac{\kappa}{2\pi}}\int_{-\infty}^{+\infty} d\nu\,\Big[w^\dagger(\nu)\,a + a^\dagger\,w(\nu)\Big]\,, \tag{2.26}$$

in which we now define κ as the cavity decay rate into the guided mode[1], and $w(\nu)$ are the waveguide field operators introduced in Sect. 2.3. The interaction is linear in both the cavity and field operators, and it conserves the total number of excitations. A distinctive feature of this architecture is that the two-level emitter does not couple directly to the waveguide: the terms of the form $\int d\nu\,[\sigma_+\,w(\nu) - \sigma_-\,w^\dagger(\nu)]$ that appeared in the bare-emitter Hamiltonian of Sect. 2.3 are now absent. The emitter can only exchange excitations with the cavity mode through the Jaynes–Cummings coupling rate (g), as evident from Eq. (2.25). Therefore, the cavity mode acts as a frequency-selective mediator between the propagating field and the qubit.

Collecting the contributions from the free field, the local system, and the waveguide-cavity coupling, the total Hamiltonian reads

$$\begin{aligned} H_{\mathrm{tot}} = {} & \hbar\int_{-\infty}^{+\infty} d\nu\,\nu\,w^\dagger(\nu)\,w(\nu) + \hbar\omega_c\,a^\dagger a + \frac{\hbar\omega_0}{2}\,\sigma_z \\ & + \hbar g\Big(\sigma_+ a + a^\dagger\sigma_-\Big) + \hbar\sqrt{\frac{\kappa}{2\pi}}\int_{-\infty}^{+\infty} d\nu\,\Big[w^\dagger(\nu)\,a + a^\dagger\,w(\nu)\Big]. \end{aligned} \tag{2.27}$$

[1]Notice that we change notation on purpose, to distinguish between the same coupling rate to a single emitter defined as γ in the previous section, and the current coupling between bosonic modes.

Since in the whole thesis we will assume that the initial state consists of a single photon propagating in the waveguide and the local system in its ground state, the dynamics is confined to the single-excitation subspace. Within this subspace, the system can be found in one of three configurations: the photon in the waveguide with the cavity empty and the emitter in $|g\rangle$, the photon absorbed by the cavity with the emitter in $|g\rangle$, or the cavity empty with the emitter in $|e\rangle$ [SF09]. This restriction reduces the problem to a local Hilbert space spanned by $\{|1_{\mathrm{wg}}, 0_c, g\rangle, |0_{\mathrm{wg}}, 1_c, g\rangle, |0_{\mathrm{wg}}, 0_c, e\rangle\}$.

Ultimately, the interplay between the cavity–emitter coupling and the cavity decay rate determines the scattering response of the system. When $\kappa \gg g$, the photon escapes the cavity before a complete Rabi oscillation can occur; the emitter acts as a weak perturbation and the transmission spectrum is dominated by a single Lorentzian resonance of width κ centered at ω_c. This is the weak-coupling (or Purcell-enhanced regime) [Uts+22]. In the opposite limit, $g > \kappa/4$, the coherent exchange between the cavity photon and the emitter becomes faster than the photon loss rate. The transmission spectrum then develops a doublet structure — the vacuum Rabi splitting — with two peaks separated by $2g$ [SF09] [OH17]. The dimensionless ratio g/κ therefore discriminates between the two regimes and governs the phase response of the system to the incident photon.

In the configuration studied in this thesis, the cavity and the emitter are always tuned to the same resonance frequency, $\omega_c = \omega_0$, and the scattering dynamics is fully characterized by two relevant energy scales, g and κ, respectively. The frequency-dependent response of the system is then explored as a function of the detuning between the photon and the common resonance, $\Delta = \omega - \omega_c$. While exact transmission and reflection amplitudes can be obtained in the stationary single-frequency limit, the time-dependent transport of an arbitrary single-photon wavepacket requires numerical integration of the equations of motion [SF09]. This is carried out within the time-bin formalism of Sect. 2.4, by propagating the full Hamiltonian Eq. (2.27) in the single-excitation subspace. The implementation and results will be presented in Chapter 4.

2.5.1 Dressed states and the polariton basis

Here we limit our analysis to the spectral characteristics of the Jaynes–Cummings Hamiltonian (i.e., no losses included). From Eq. (2.25), it is evident that, given an initial state, the dynamics conserves the total excitation number $N = a^\dagger a + \sigma_+\sigma_-$. Hence, the dynamics relevant to single-photon scattering are confined to the $N = 1$ sector. This is the standard approach to study vacuum Rabi oscillations and single-photon transport in cavity QED [SF09; LMS15]. In this sector, the cavity-qubit

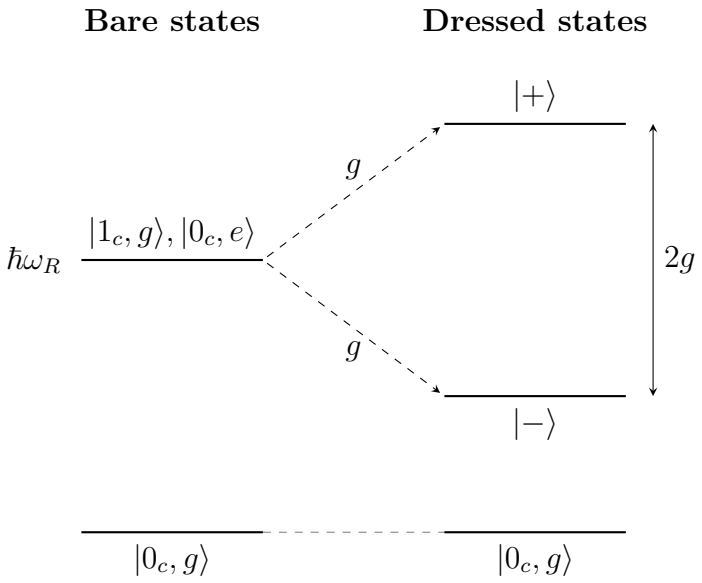

Figure 2.4: Energy level diagram illustrating the formation of the dressed state basis. At resonance ($\omega_c = \omega_0 = \omega_R$), the degenerate bare states $|1_c, g\rangle$ and $|0_c, e\rangle$ couple via the coherent exchange interaction g. This coupling lifts the degeneracy, creating the dressed states $|\pm\rangle$ separated by the vacuum Rabi splitting $2g$.

Hilbert space is two-dimensional and it is spanned by the states

$$|1_c, g\rangle, \qquad |0_c, e\rangle. \tag{2.28}$$

These states denote one photon in the cavity with the qubit in the ground state, and the empty cavity with the excited qubit, respectively. Assuming the resonance condition $\omega_c = \omega_0 \equiv \omega_R$ adopted in this work, the bare cavity and qubit contributions to the JC Hamiltonian give the same diagonal energy $\hbar\omega_R/2$ to both basis vectors. In the frame rotating at ω_R, this common shift is removed. Only the coherent exchange $\hbar g\,(\sigma_+ a + a^\dagger \sigma_-)$ survives. This interaction couples $|1_c, g\rangle$ and $|0_c, e\rangle$ symmetrically with interaction strength $\hbar g$. The diagonalization is straightforward. The eigenstates are the dressed states, or polaritons, as shown in Figure 2.4:

$$|\pm\rangle = \frac{1}{\sqrt{2}}\Big(|1_c, g\rangle \pm |0_c, e\rangle\Big), \tag{2.29}$$

with eigenvalues $\pm\hbar g$ in the rotating frame. These correspond to physical energies $E_\pm = \hbar(\omega_R \pm g)$. The two polaritons are separated by the vacuum Rabi splitting $2g$ [SF09; LMS15]. This splitting is the spectral signature of the coherent hybridization between the cavity and the qubit excitation in the strong coupling regime.

2.5.2 Effective two-level system picture in the single-excitation subspace

The primary goal of this section is to demonstrate that, when restricted to the single-photon regime, the composite Jaynes–Cummings system effectively behaves as a simple two-level emitter, with a modified coupling rate to the continuum as compared to the single-emitter case. This mathematical reduction provides a highly intuitive framework to understand the complex scattering dynamics. This behavior can be easily observed by analyzing the output field equations. The interferometric response of the device is determined by the cavity amplitude $a(t)$ entering the input–output relation

$$\xi_{\text{out}}(t) = \xi_{\text{in}}(t) - \sqrt{\kappa}\, a(t). \tag{2.30}$$

This equation expresses the output field as a coherent superposition of the incoming field field and the cavity re-emission [GC85; Bar+12]. In the single-excitation sector, $a(t)$ has a precise definition: it is the projection of the joint state $|\psi(t)\rangle$ on the cavity-excited basis vector $|1_c, g\rangle$,

$$a(t) = \langle 1_c, g \,|\, \psi(t)\rangle. \tag{2.31}$$

The polariton basis of Eq. (2.29) provides an equivalent description of this two-dimensional cavity-qubit subspace. Inverting Eq. (2.29) yields

$$|1_c, g\rangle = \frac{|+\rangle + |-\rangle}{\sqrt{2}}, \tag{2.32}$$

and substituting this into Eq. (2.31) gives

$$a(t) = \frac{1}{\sqrt{2}}\Big[\langle + \,|\, \psi(t)\rangle + \langle - \,|\, \psi(t)\rangle\Big] = \frac{c_+(t) + c_-(t)}{\sqrt{2}}, \tag{2.33}$$

where $c_\pm(t) \equiv \langle \pm \,|\, \psi(t)\rangle$ are the polariton amplitudes. This decomposition is exact. It is a direct consequence of the unitarity of the basis transformation between $\{|1_c, g\rangle, |0_c, e\rangle\}$ and $\{|+\rangle, |-\rangle\}$. The same logic applied to the qubit-excited basis vector gives $|0_c, e\rangle = (|+\rangle - |-\rangle)/\sqrt{2}$ and the analogous qubit amplitude $b(t) = \langle 0_c, e \,|\, \psi(t)\rangle = [c_+(t) - c_-(t)]/\sqrt{2}$. This term does not enter the input-output relation directly. In Appendix G, this framework is used to reduce the input-output relation on a single-polariton resonance. This reduction recovers an effective two-level emitter picture that we will employ to interpret the time-domain JC scattering response calculated in Chapter 4.

Chapter 3

Quantum MZI with a single qubit: analytic solution

3.1 Overview

While the time-bin formalism provides a robust framework for numerical integration of the Schrödinger equation, as illustrated in the previous chapter, a comprehensive understanding of the light-matter interaction requires a rigorous analytical treatment. In this chapter, we derive the exact analytic solution for the emitter's excitation amplitude by solving the continuous-time equation of motion.

3.2 Analytic solution for the scattering of a two-level emitter in WQED

The dynamics of a single two-level emitter interacting with the single-photon wavepacket is governed by the first-order linear ordinary differential equation (ODE) previously introduced:

$$\frac{d\psi_e(t)}{dt} = -\frac{\gamma}{2}\psi_e(t) + \sqrt{\gamma}\xi(t), \tag{3.1}$$

where $\psi_e(t)$ is the probability amplitude of the emitter being in the excited state, γ is the spontaneous emission rate into the waveguide, and $\xi(t)$ is the temporal envelope of the incident single-photon pulse.

To solve Eq. (3.1), we employ the integrating factor method. First, we rewrite the equation in the standard form for a linear first-order ODE, $\frac{dy}{dt} + a(t)y = f(t)$:

$$\frac{d\psi_e(t)}{dt} + \frac{\gamma}{2}\psi_e(t) = \sqrt{\gamma}\xi(t). \tag{3.2}$$

We then define the integrating factor $\mu(t)$, which is given by the exponential of

the integral of the coefficient multiplying $\psi_e(t)$:

$$\mu(t) = \exp\left(\int \frac{\gamma}{2}\, dt\right) = e^{\frac{\gamma}{2}t}. \tag{3.3}$$

Multiplying both sides of Eq. (3.2) by this integrating factor yields:

$$e^{\frac{\gamma}{2}t}\frac{d\psi_e(t)}{dt} + e^{\frac{\gamma}{2}t}\frac{\gamma}{2}\psi_e(t) = e^{\frac{\gamma}{2}t}\sqrt{\gamma}\xi(t). \tag{3.4}$$

The left-hand side of this expression is precisely the time derivative of the product of the integrating factor and the excitation amplitude. Thus, we can condense the equation into:

$$\frac{d}{dt}\left[e^{\frac{\gamma}{2}t}\psi_e(t)\right] = \sqrt{\gamma}\xi(t)e^{\frac{\gamma}{2}t}. \tag{3.5}$$

To determine the time evolution of the system, we integrate both sides of Eq. (3.5) with respect to a dummy time variable, t', from the initial time $t = 0$ to an arbitrary time t:

$$\int_0^t \frac{d}{dt'}\left[e^{\frac{\gamma}{2}t'}\psi_e(t')\right] dt' = \int_0^t \sqrt{\gamma}\xi(t')e^{\frac{\gamma}{2}t'}\, dt'. \tag{3.6}$$

Evaluating the integral on the left-hand side using the Fundamental Theorem of Calculus, we obtain:

$$\left[e^{\frac{\gamma}{2}t'}\psi_e(t')\right]_0^t = e^{\frac{\gamma}{2}t}\psi_e(t) - e^0\psi_e(0). \tag{3.7}$$

According to the physical setup described in the theoretical framework, the system is initialized with the emitter in its ground state $|g\rangle$ prior to the arrival of the photon. This boundary condition implies $\psi_e(0) = 0$. Applying this to our equation, the expression simplifies to:

$$e^{\frac{\gamma}{2}t}\psi_e(t) = \sqrt{\gamma}\int_0^t \xi(t')e^{\frac{\gamma}{2}t'}\, dt'. \tag{3.8}$$

Finally, by isolating the excitation amplitude $\psi_e(t)$, we arrive at the exact analytical expression for the state of the quantum emitter at any given time t:

$$\psi_e(t) = \sqrt{\gamma}e^{-\frac{\gamma}{2}t}\int_0^t \xi(t')e^{\frac{\gamma}{2}t'}\, dt'. \tag{3.9}$$

This closed-form integral solution provides a complete deterministic description of the emitter's dynamics for an arbitrary input single-photon wavepacket $\xi(t)$. It serves not only as a rigorous theoretical counterpart to our fundamental physical intuition but also as the absolute baseline against which the discrete time-bin numerical methods and standard ODE solvers (such as the RK4 method) must be evaluated and validated.

3.3 Single-photon routing through a quantum MZI with a single qubit in one arm

Having established the exact analytical solution for the scattering of a single photon by the TLS, we can now embed this dynamic interaction within the MZI architecture. As discussed in Chapter 1, the MZI translates phase shifts into measurable spatial routing. Here, we evaluate the full operatorial evolution of the single-photon wavepacket as it propagates through the device, with the TLS located in the upper arm.

We initialize the system by injecting a single-photon wavepacket with temporal envelope $\xi_{in}(t)$ into the first input port (a), while the second input port (b) is in the vacuum state. The initial state of the field is:

$$|\Psi_{in}\rangle = \int dt\, \xi_{in}(t)\hat{a}^\dagger(t)|\emptyset\rangle. \tag{3.10}$$

The photon first encounters a 50:50 beam splitter (BS1). Following the real-valued unitary transformations (Hadamard convention), the creation operator splits into the upper (u) and lower (l) spatial modes without accumulating imaginary phase shifts:

$$\hat{a}^\dagger(t) \to \frac{1}{\sqrt{2}}\left[\hat{u}^\dagger(t) + \hat{l}^\dagger(t)\right]. \tag{3.11}$$

Consequently, the state of the system immediately after BS1 becomes a coherent spatial superposition:

$$|\Psi_1\rangle = \frac{1}{\sqrt{2}}\int dt\, \xi_{in}(t)\left[\hat{u}^\dagger(t) + \hat{l}^\dagger(t)\right]|\emptyset\rangle. \tag{3.12}$$

As the wavepackets propagate, the component in the lower arm travels freely, maintaining its original temporal envelope $\xi_{in}(t)$ (assuming negligible propagation losses and perfectly matched path lengths). Conversely, the wavepacket in the upper arm interacts resonantly with the TLS. As derived in the input-output formalism, this interaction maps the input envelope $\xi_{in}(t)$ into a scattered output envelope $\xi_{out}(t)$. Therefore, the state immediately before the second beam splitter (BS2) is:

$$|\Psi_2\rangle = \frac{1}{\sqrt{2}}\int dt\, \left[\xi_{out}(t)\hat{u}^\dagger(t) + \xi_{in}(t)\hat{l}^\dagger(t)\right]|\emptyset\rangle. \tag{3.13}$$

The two modes are then recombined at BS2. Applying the real-valued beam splitter transformations to both the upper and lower arm operators to map them

into the final output ports c and d:

$$\hat{u}^\dagger(t) \to \frac{1}{\sqrt{2}}\left[\hat{c}^\dagger(t) + \hat{d}^\dagger(t)\right], \tag{3.14}$$

$$\hat{l}^\dagger(t) \to \frac{1}{\sqrt{2}}\left[\hat{c}^\dagger(t) - \hat{d}^\dagger(t)\right]. \tag{3.15}$$

Substituting these transformations into $|\Psi_2\rangle$, we obtain the final state of the system:

$$|\Psi_{out}\rangle = \frac{1}{2}\int dt \left\{\xi_{out}(t)\left[\hat{c}^\dagger(t) + \hat{d}^\dagger(t)\right] + \xi_{in}(t)\left[\hat{c}^\dagger(t) - \hat{d}^\dagger(t)\right]\right\}|\emptyset\rangle. \tag{3.16}$$

Expanding and grouping the terms associated with each output port, the expression simplifies to:

$$|\Psi_{out}\rangle = \frac{1}{2}\int dt \left\{\left[\xi_{out}(t) + \xi_{in}(t)\right]\hat{c}^\dagger(t) + \left[\xi_{out}(t) - \xi_{in}(t)\right]\hat{d}^\dagger(t)\right\}|\emptyset\rangle. \tag{3.17}$$

From this final state, we can extract the time-dependent detection probabilities (or photon fluxes) at the two output ports. The intensity at the two output ports c and d are given by:

$$P_c(t) = \frac{1}{4}\left|\xi_{out}(t) + \xi_{in}(t)\right|^2, \tag{3.18}$$

$$P_d(t) = \frac{1}{4}\left|\xi_{out}(t) - \xi_{in}(t)\right|^2. \tag{3.19}$$

These equations capture the device's operational principle. The dynamic phase and amplitude modulations encoded within $\xi_{out}(t)$ by the quantum emitter are directly translated into macroscopic intensity variations at the output ports. In the absence of the TLS ($\xi_{out}(t) = \xi_{in}(t)$), perfect destructive interference occurs at port d ($P_d = 0$), and all light exits through port c.

3.4 Analytic Integration for a Gaussian Wavepacket

To evaluate the exact dynamics of the quantum emitter, we explicitly solve the integral in the equation of motion for an incident single-photon Gaussian wavepacket. The temporal envelope of the incoming photon is defined as:

$$\xi(t) = \sqrt{\frac{2}{\tau_G}}\left(\frac{\ln 2}{\pi}\right)^{\frac{1}{4}} e^{-2\ln 2\frac{(t-t_0)^2}{\tau_G^2}} \tag{3.20}$$

where τ_G characterizes the pulse width and t_0 represents the central arrival time. Substituting this wavepacket into the general integral solution for the emitter's ex-

citation amplitude, we obtain:

$$\psi_e(t) = \sqrt{\gamma}\sqrt{\frac{2}{\tau_G}}\left(\frac{\ln 2}{\pi}\right)^{\frac{1}{4}} e^{-\frac{\gamma}{2}t}\int_0^t e^{-2\ln 2\frac{(t'-t_0)^2}{\tau_G^2}} e^{\frac{\gamma}{2}t'}dt' \tag{3.21}$$

To compute this integral, it is convenient to aggregate the arguments of the exponential functions within the integrand. Let $E(t')$ denote this combined argument. Expanding the quadratic term yields:

$$E(t') = -\frac{2\ln 2}{\tau_G^2}(t'^2 - 2t_0t' + t_0^2) + \frac{\gamma}{2}t' \tag{3.22}$$

We proceed by completing the square to express $E(t')$ in the form $-a(t'-\mu)^2 + K$, defining the coefficient $a = \frac{2\ln 2}{\tau_G^2}$. Equating the linear coefficients allows us to identify the shifted center of the Gaussian profile, μ:

$$2a\mu = 2at_0 + \frac{\gamma}{2} \implies \mu = t_0 + \frac{\gamma\tau_G^2}{8\ln 2} \tag{3.23}$$

Subsequently, we determine the residual constant K by balancing the time-independent terms:

$$-a\mu^2 + K = -at_0^2 \implies K = a(\mu^2 - t_0^2) \tag{3.24}$$

By substituting $\mu = t_0 + \frac{\gamma}{4a}$, the constant K evaluates to:

$$K = \frac{\gamma}{2}t_0 + \frac{\gamma^2\tau_G^2}{32\ln 2} \tag{3.25}$$

With the square completed, the integral can be elegantly recast in terms of the shifted temporal coordinate. Factoring the constant term e^K out of the integral and grouping it with the external decay exponential $e^{-\frac{\gamma}{2}t}$, the excitation amplitude becomes:

$$\psi_e(t) = \sqrt{\gamma}\sqrt{\frac{2}{\tau_G}}\left(\frac{\ln 2}{\pi}\right)^{\frac{1}{4}} e^{-\frac{\gamma}{2}(t-t_0)+\frac{\gamma^2\tau_G^2}{32\ln 2}}\int_0^t e^{-\frac{2\ln 2}{\tau_G^2}(t'-\mu)^2}dt' \tag{3.26}$$

This definite integral is readily resolved via the substitution $x = \frac{\sqrt{2\ln 2}}{\tau_G}(t'-\mu)$, mapping the expression to the standard error function, $\mathrm{erf}(z) = \frac{2}{\sqrt{\pi}}\int_0^z e^{-x^2}dx$. By applying the transformed integration limits $x(t)$ and $x(0)$, we derive the final closed-form analytical expression for the emitter's excitation amplitude. To enhance the readability of the formula, we can express the exponential argument in terms of the previously defined constant K, noting that $-\frac{\gamma}{2}(t-t_0) + \frac{\gamma^2\tau_G^2}{32\ln 2} = -\frac{\gamma}{2}t + K$. Furthermore, by algebraically simplifying and aggregating the constant prefactors,

the equation elegantly condenses to:

$$\psi_e(t) = \mathcal{C}_G\, e^{-\frac{\gamma}{2}t+K}\left[\operatorname{erf}\left(\frac{(t-\mu)\sqrt{2\ln 2}}{\tau_G}\right) - \operatorname{erf}\left(-\frac{\mu\sqrt{2\ln 2}}{\tau_G}\right)\right], \tag{3.27}$$

where the global amplitude coefficient simplifies to $\mathcal{C}_G = \frac{\sqrt{\gamma}}{2}\left(\frac{\pi\tau_G^2}{\ln 2}\right)^{\frac{1}{4}}$. This deterministic solution rigorously describes the transient excitation and subsequent radiative decay of the TLS, capturing the finite-bandwidth effects and the dynamic interaction induced by the single-photon wavepacket. It is worth noting that a mathematically equivalent time-domain analytical solution for the Gaussian wavepacket, similarly expressed in terms of error functions, was also derived by Chen *et al.* in the context of optimizing single-photon absorption in one-dimensional nanophotonic waveguides [Che+11].

While the parameterization of the Gaussian wavepacket in terms of the Full Width at Half Maximum (FWHM), denoted as τ_G, is ubiquitous in experimental settings due to its direct measurability, rigorous theoretical treatments generally favor the standard statistical formulation of the Gaussian distribution, that is, the one parametrized by the standard deviation σ.

Adopting the standard deviation offers profound conceptual and mathematical advantages. Primarily, σ directly defines the quantum mechanical uncertainty in the photon's arrival time, $\Delta t = \sigma$ [SZ97][GK23]. Furthermore, operating with σ streamlines the transition to the frequency domain via the Fourier transform, yielding a symmetric Gaussian spectral profile with standard deviation $\sigma_\omega = 1/(2\sigma)$. This natural symmetry greatly simplifies the evaluation of the Heisenberg uncertainty limit, $\Delta t \Delta\omega \geq 1/2$, without the burden of unwieldy numerical prefactors.

To bridge the experimental and theoretical formalisms, we establish the exact mapping between the intensity FWHM, τ_G, and the amplitude standard deviation, σ. By equating the exponential arguments of the probability density profiles, $|\xi(t)|^2$, derived from both representations, we find:

$$\frac{(t-t_0)^2}{2\sigma^2} = 4\ln 2\frac{(t-t_0)^2}{\tau_G^2} \tag{3.28}$$

which readily yields the fundamental relation:

$$\tau_G = 2\sigma\sqrt{2\ln 2} \tag{3.29}$$

By substituting this relation into the initial wavepacket definition, all the intricate numerical constants cancel out elegantly. This allows us to recast the incident

field amplitude into its canonical standard form:

$$\xi(t) = \left(\frac{1}{2\pi\sigma^2}\right)^{\frac{1}{4}} e^{-\frac{(t-t_0)^2}{4\sigma^2}} \tag{3.30}$$

This strictly normalized expression ensures $\int |\xi(t)|^2 dt = 1$ and serves as a cleaner, more intuitive theoretical baseline for evaluating the exact analytical dynamics of the emitter.

By substituting this canonical Gaussian envelope into the general integral solution, the analytical evaluation proceeds via completing the square in the exponent. The mathematical derivation is considerably streamlined in this parameterization. The shifted temporal center of the interaction naturally reduces to $\mu = t_0 + \gamma\sigma^2$. Evaluating the definite integral through the substitution $x = \frac{t'-\mu}{2\sigma}$ directly yields the closed-form excitation amplitude:

$$\psi_e(t) = \sqrt{\gamma}\left(\frac{\pi\sigma^2}{2}\right)^{\frac{1}{4}} e^{-\frac{\gamma}{2}(t-t_0)+\frac{\gamma^2\sigma^2}{4}} \left[\operatorname{erf}\left(\frac{t-\mu}{2\sigma}\right) - \operatorname{erf}\left(-\frac{\mu}{2\sigma}\right)\right] \tag{3.31}$$

This formulation perfectly recovers the exact deterministic dynamics of the quantum dot while providing a mathematically elegant and physically transparent parameterization of the finite-bandwidth effects.

3.5 Dependence on photon-qubit detuning and Rotating Frame Transformation

In the standard waveguide QED scattering model presented thus far, the interaction between the single-photon wavepacket and the two-level emitter has been treated under the assumption of perfect resonance. However, a rigorous and comprehensive description must account for a finite frequency detuning between the incident optical field and the atomic transition.

Let ω_0 denote the resonant transition frequency of the two-level system (TLS) and ω be the central carrier frequency of the incident single-photon wavepacket. The total Hamiltonian of the system can be decomposed into three fundamental contributions, $H_{TOT} = H_{sys} + H_f + H_{int}$. For the sake of convenience, we set the energy of the ground state $|g\rangle$ to zero. The free Hamiltonian of the TLS is expressed as $H_{sys} = \hbar\omega_0\sigma^\dagger\sigma$, where $\sigma^\dagger\sigma$ is the excitation number operator. The continuous field in the waveguide is described by $H_f = \hbar\int d\nu\, \nu w^\dagger(\nu)w(\nu)$, and the standard dipole interaction is given by $H_{int} = i\hbar\int d\nu\, g(\nu)[\sigma^\dagger w(\nu) - \sigma w^\dagger(\nu)]$, where $g(\nu) \approx \sqrt{\gamma/2\pi}$ under the assumption of a flat spectral density around the resonance.

To factor out the high-frequency optical oscillations and explicitly isolate the

dynamic effect of the detuning $\Delta = \omega_0 - \omega$, it is analytically necessary to transition into a rotating reference frame. To do so, we define a unitary transformation operator that rotates both the atomic system and the continuous field modes at the carrier frequency ω:

$$U(t) = \exp\left[i\omega t\left(\sigma^\dagger\sigma + \int d\nu\, w^\dagger(\nu)w(\nu)\right)\right]. \tag{3.32}$$

The dynamics of the state vector in this rotating frame, defined as $|\psi'\rangle = U(t)|\psi\rangle$, are governed by the Schrödinger equation. Taking the exact time derivative yields $i\hbar\partial_t|\psi'\rangle = \left(i\hbar\dot{U}U^\dagger + UH_{TOT}U^\dagger\right)|\psi'\rangle$, which defines the effective Hamiltonian in the rotating frame:

$$H' = UH_{TOT}U^\dagger + i\hbar\dot{U}U^\dagger. \tag{3.33}$$

We systematically apply this transformation to the individual components of the total Hamiltonian. The gauge term associated with the time derivative of the unitary operator yields $i\hbar\dot{U}U^\dagger = -\hbar\omega\sigma^\dagger\sigma - \hbar\omega\int d\nu\, w^\dagger(\nu)w(\nu)$. Combining this with the free energy terms, the system and field Hamiltonians in the rotating frame become:

$$H'_{sys} = \hbar(\omega_0 - \omega)\sigma^\dagger\sigma = \hbar\Delta\sigma^\dagger\sigma, \tag{3.34}$$

$$H'_f = \hbar\int d\nu\,(\nu - \omega)w^\dagger(\nu)w(\nu). \tag{3.35}$$

Crucially, because the transformation rotates both the atomic operators and the field operators equally ($U\sigma^\dagger U^\dagger = \sigma^\dagger e^{-i\omega t}$ and $Uw(\nu)U^\dagger = w(\nu)e^{i\omega t}$), the interaction Hamiltonian H_{int} commutes completely with the rotation operator, retaining its original time-independent form.

To bridge this representation with the time-bin formalism, we adopt the Slowly Varying Envelope Approximation (SVEA) [SK24; Ran24]. Physically, this approximation assumes that the spectral bandwidth of the single-photon wavepacket is extremely narrow compared to its central optical carrier frequency ω. As a consequence, the temporal envelope of the field varies much more slowly than the rapid underlying optical oscillations. This temporal scale separation allows us to factor out the high-frequency carrier and mathematically define the continuous time-domain field operators purely in terms of their slowly varying envelope. By absorbing the free evolution of the detuned field modes, we define the wavepacket envelope operators as $\tilde{w}(t) = \frac{1}{\sqrt{2\pi}}\int d\nu\, w(\nu)e^{-i(\nu-\omega)t}$. This strictly localizes the interaction, yielding a localized effective interaction Hamiltonian $H'_{int}(t) = i\hbar\sqrt{\gamma}(\sigma^\dagger\tilde{w}(t) - \sigma\tilde{w}^\dagger(t))$.

Within the time-bin formalism, the total effective Hamiltonian H'_k dictates the discrete unitary propagator U_k for each temporal mode of width Δt. Including the

detuning term, the local Hamiltonian for the k-th bin is:

$$H'_k = \hbar\Delta\sigma^\dagger\sigma + i\hbar\sqrt{\frac{\gamma}{\Delta t}}\left(\sigma^\dagger w_k - \sigma w_k^\dagger\right). \tag{3.36}$$

Expanding the unitary evolution operator $U_k = \exp(-iH'_k\Delta t/\hbar)$ to first order in Δt, we obtain:

$$U_k \simeq I - i\Delta\,\Delta t\sigma^\dagger\sigma + \sqrt{\gamma\Delta t}\left(\sigma^\dagger w_k - \sigma w_k^\dagger\right) - \frac{\gamma\Delta t}{2}\sigma^\dagger\sigma w_k w_k^\dagger. \tag{3.37}$$

We now apply this propagator to the relevant sub-spaces to evaluate the state evolution. When the photon is absorbed, the evolution of the excited state is given by:

$$U_k|e\rangle|\emptyset\rangle = \left(1 - i\Delta\,\Delta t - \frac{\gamma}{2}\Delta t\right)|e\rangle|\emptyset\rangle - \sqrt{\gamma\Delta t}|g\rangle|1_k\rangle. \tag{3.38}$$

Conversely, when the emitter is in the ground state and interacts with the incident photon, the evolution is:

$$U_k|g\rangle|1_k\rangle = |g\rangle|1_k\rangle + \sqrt{\gamma\Delta t}|e\rangle|\emptyset\rangle. \tag{3.39}$$

By taking the continuum limit $\Delta t \to 0$ of the resulting discrete finite-difference equations, the differential equation governing the excited state probability amplitude $\psi_e(t)$ rigorously acquires a complex frequency shift:

$$\frac{d\psi_e(t)}{dt} = -\left(i\Delta + \frac{\gamma}{2}\right)\psi_e(t) + \sqrt{\gamma}\xi(t). \tag{3.40}$$

This operatorial derivation demonstrates that the detuning Δ naturally emerges from the gauge transformation, effectively acting as an imaginary frequency component that dynamically couples to the dissipative radiative decay of the quantum emitter. Following the mathematical framework established in Section 3.1, the exact analytical solution to the detuned differential equation (Eq. 3.40) is obtained via the integrating factor method. The general integral solution for the emitter's excitation amplitude is formally identical to the resonant case, albeit acquiring a complex phase winding:

$$\psi_e(t) = \sqrt{\gamma}e^{-\left(i\Delta+\frac{\gamma}{2}\right)t}\int_0^t \xi(t')e^{\left(i\Delta+\frac{\gamma}{2}\right)t'}dt'. \tag{3.41}$$

We evaluate this integral explicitly for the incident single-photon Gaussian wavepacket utilizing its canonical standard deviation parameterization $\xi(t)$, which reads $\xi(t) = (2\pi\sigma^2)^{-1/4}\exp[-(t-t_0)^2/4\sigma^2]$. The integration proceeds by completing the square in the exponent. Crucially, the presence of the detuning shifts the effective temporal center of the interaction into the complex plane, defining a generalized shifted center

$\mu_D = t_0 + \sigma^2(\gamma + 2i\Delta)$.

By factoring out the resulting complex constants and resolving the integral via the standard error function, we derive the exact, closed-form expression for the detuned excitation amplitude:

$$\psi_e(t) = \sqrt{\gamma}\left(\frac{\pi\sigma^2}{2}\right)^{\frac{1}{4}} e^{-\left(i\Delta+\frac{\gamma}{2}\right)(t-t_0)+\frac{\sigma^2}{4}(\gamma+2i\Delta)^2}\left[\operatorname{erf}\left(\frac{t-\mu_D}{2\sigma}\right) - \operatorname{erf}\left(-\frac{\mu_D}{2\sigma}\right)\right]. \quad (3.42)$$

This comprehensive deterministic solution fully captures both the finite-bandwidth effects dictated by σ and the dynamical phase modulations induced by the frequency mismatch Δ. It is worth noting that the evaluation of the error function with complex arguments is numerically straightforward and natively supported by standard computational libraries. For instance, it is readily computed via the Faddeeva function implementation `scipy.special.wofz` in the SciPy ecosystem [Vir+20; Sci24]. This computational accessibility makes the derived analytical result directly applicable and highly efficient for validating detuned time-bin numerical simulations.

3.6 Transmission/Reflection Probabilities and Phase Accumulation

Having obtained the exact analytical expression for the emitter's excitation amplitude $\psi_e(t)$ in the presence of detuning, we can now determine the macroscopic outcome of the scattering process within the MZI. Specifically, we are interested in the total integrated probabilities of detecting the single photon at the output ports c and d.

As derived in Section 3.2, the time-dependent intensities at the output ports are given by $P_c(t) = \frac{1}{4}|\xi_{out}(t) + \xi_{in}(t)|^2$ and $P_d(t) = \frac{1}{4}|\xi_{out}(t) - \xi_{in}(t)|^2$. In the following discussion, P_c will be referred to as the transmission probability, as it represents the default routing path for an unperturbed wavepacket experiencing perfect constructive interference. Conversely, P_d will be designated as the reflection probability, since it captures the fraction of the field that is dynamically scattered into the otherwise dark port strictly due to the interaction with the quantum emitter. To evaluate these quantities, we leverage the fundamental input-output relation of waveguide QED, $\xi_{out}(t) = \xi_{in}(t) - \sqrt{\gamma}\psi_e(t)$. Substituting this into the expression for the transmission-like port d, the incident field perfectly cancels out, yielding a direct proportionality to the emitter's excitation probability:

$$P_d(t) = \frac{1}{4}|-\sqrt{\gamma}\psi_e(t)|^2 = \frac{\gamma}{4}|\psi_e(t)|^2 \quad (3.43)$$

The total probability $\mathcal{P}_d$ of the photon being routed to port d is the time integral

of this intensity over the entire scattering event. While integrating the complex time-domain solution is mathematically cumbersome, we can vastly simplify the problem by transitioning to the frequency domain. Utilizing Parseval's theorem [Mor17], we can express the total probability as an integral over the spectral components:

$$\mathcal{P}_d = \frac{\gamma}{4}\int_{-\infty}^{+\infty} |\psi_e(t)|^2 dt = \frac{\gamma}{4}\frac{1}{2\pi}\int_{-\infty}^{+\infty} |\tilde{\psi}_e(\omega)|^2 d\omega \tag{3.44}$$

To proceed, we must first determine the spectral intensity of the incident Gaussian wavepacket, $|\tilde{\xi}_{in}(\omega)|^2$. The temporal envelope of the normalized Gaussian pulse is given by $\xi_{in}(t) = \mathcal{N} e^{-\frac{t^2}{4\sigma^2}}$, where the normalization constant is $\mathcal{N} = \frac{1}{\sqrt{\sigma}}(\frac{1}{2\pi})^{1/4}$. The Fourier transform is defined as:

$$\tilde{\xi}_{in}(\omega) = \int_{-\infty}^{+\infty} \mathcal{N} e^{-\frac{t^2}{4\sigma^2}} e^{i\omega t} dt \tag{3.45}$$

This can be resolved using the standard Gaussian integral relation $\int e^{-at^2} e^{ikt} dt = \sqrt{\frac{\pi}{a}} e^{-\frac{k^2}{4a}}$. By setting $a = \frac{1}{4\sigma^2}$ and $k = \omega$, the resulting spectral amplitude allows us to compute the squared modulus:

$$|\tilde{\xi}_{in}(\omega)|^2 = 2\sigma\sqrt{2\pi} e^{-2\sigma^2\omega^2} \tag{3.46}$$

Next, we evaluate the emitter's excitation in the frequency domain. By applying the Fourier transform to the time-domain equation of motion derived previously, the differential equation transforms into a simple algebraic relation:

$$-i\omega\tilde{\psi}_e(\omega) = -\left(\frac{\gamma}{2} + i\Delta\right)\tilde{\psi}_e(\omega) + \sqrt{\gamma}\tilde{\xi}_{in}(\omega) \tag{3.47}$$

Isolating $\tilde{\psi}_e(\omega)$ and computing its squared modulus yields a Lorentzian response centered around the detuning Δ:

$$|\tilde{\psi}_e(\omega)|^2 = \frac{\gamma|\tilde{\xi}_{in}(\omega)|^2}{(\frac{\gamma}{2})^2 + (\omega - \Delta)^2} \tag{3.48}$$

Substituting this and the Gaussian spectral intensity back into the Parseval integral for $\mathcal{P}_d$, we obtain the exact integral formulation for the routing probability:

$$\mathcal{P}_d = \frac{\gamma^2}{8\pi}\int_{-\infty}^{+\infty} \frac{2\sigma\sqrt{2\pi} e^{-2\sigma^2\omega^2}}{(\frac{\gamma}{2})^2 + (\omega - \Delta)^2} d\omega \tag{3.49}$$

This integral represents the convolution of a Gaussian spectral profile (originating from the finite bandwidth of the incident wavepacket) and a Lorentzian resonance (characterizing the natural lineshape of the two-level emitter). To solve this analytically, we perform the variable substitution $x = \sqrt{2}\sigma\omega$, which implies $d\omega = \frac{1}{\sqrt{2}\sigma} dx$.

Factoring out the constants, the integral maps perfectly to a well-known analytical form related to the Faddeeva function, $W(z)$ [AS64]:

$$\int_{-\infty}^{+\infty} \frac{e^{-x^2}}{a^2 + (x-y)^2} dx = \frac{\pi}{a} \mathrm{Re}[W(y + ia)] \tag{3.50}$$

By comparing the denominators, we identify the scaled parameters $y = \sqrt{2}\sigma\Delta$ and $a = \frac{\gamma\sigma}{\sqrt{2}}$. Replacing these into the analytical solution, the total routing probability to port d elegantly reduces to a closed-form expression:

$$\mathcal{P}_d = \gamma\sigma\sqrt{\frac{\pi}{2}} \mathrm{Re}\left[W\left(\sqrt{2}\sigma\left(\Delta + i\frac{\gamma}{2}\right)\right)\right] \tag{3.51}$$

From a physical perspective, the real part of the Faddeeva function exactly defines the Voigt profile, see Appendix B. This result conceptually seals the quantum scattering problem: the macroscopic switching efficiency of the MZI is deterministically governed by the Voigt profile, encapsulating the overlap between the photon's continuous-mode spectral distribution and the broadened atomic resonance of the quantum dot.

Finally, assuming a lossless beam splitter and perfect waveguide-to-emitter coupling efficiency, the unitarity of the total system is preserved. Consequently, the probability of detecting the photon at the transmission-like port c is simply the complement:

$$\mathcal{P}_c = 1 - \mathcal{P}_d \tag{3.52}$$

Beyond the macroscopic routing probabilities, the interaction with the two-level emitter crucially imprints a dynamic, frequency-dependent phase shift on the propagating single-photon wavepacket. In the context of quantum information processing, this phase accumulation is the fundamental mechanism that enables the two-level system to operate as a coherent phase shifter within the MZI.

Since the incident single photon is not perfectly monochromatic but possesses a finite bandwidth, different spectral components accumulate different phase shifts. To rigorously define the global, effective phase shift Φ_{eff} measured at the output ports, we must evaluate the macroscopic transmission amplitude $\mathcal{T}$. This quantity is formally defined as the overlap integral between the incident unscattered wavepacket and the scattered output field:

$$\mathcal{T} = \frac{1}{2\pi} \int_{-\infty}^{+\infty} \tilde{\xi}_{in}^*(\omega) \tilde{\xi}_{out}(\omega) d\omega \tag{3.53}$$

By substituting the frequency-domain input-output relation, $\tilde{\xi}_{out}(\omega) = \tilde{\xi}_{in}(\omega) -$

$\sqrt{\gamma}\tilde{\psi}_e(\omega)$, into the overlap integral, we obtain:

$$\mathcal{T} = \frac{1}{2\pi}\int_{-\infty}^{+\infty} |\tilde{\xi}_{in}(\omega)|^2 d\omega - \frac{1}{2\pi}\sqrt{\gamma}\int_{-\infty}^{+\infty} \tilde{\xi}^*_{in}(\omega)\tilde{\psi}_e(\omega)d\omega \tag{3.54}$$

The first term is simply the normalization of the incident wavepacket, which equals unity. The second term defines the complex macroscopic scattering response of the emitter, which we denote as $\mathcal{Z}(\Delta)$. Recalling the algebraic solution for $\tilde{\psi}_e(\omega)$, we can write:

$$\mathcal{Z}(\Delta) = \frac{1}{2\pi}\int_{-\infty}^{+\infty} \frac{\gamma|\tilde{\xi}_{in}(\omega)|^2}{\frac{\gamma}{2} + i(\Delta - \omega)}d\omega \tag{3.55}$$

At first glance, the denominator of this integral is linear in the complex plane, whereas the integral for the macroscopic transmission probability $\mathcal{P}_d$ derived in the previous section featured a strictly real, squared denominator. However, rationalizing the complex fraction reveals a profound physical connection inherent to the Optical Theorem [SN17]. As established in general scattering theory, this fundamental theorem dictates that the total probability of scattering (extinction) is directly proportional to the imaginary part of the forward scattering amplitude. In our one-dimensional waveguide geometry, this principle manifests elegantly:

$$\frac{1}{\frac{\gamma}{2} + i(\Delta - \omega)} = \frac{\frac{\gamma}{2} - i(\Delta - \omega)}{\left(\frac{\gamma}{2}\right)^2 + (\Delta - \omega)^2} \tag{3.56}$$

The real part of this rationalized integrand is precisely the Lorentzian profile governing the absorptive routing dynamics. Complementary to this, the imaginary part of the integrand dictates the dispersive properties of the interaction, directly governing the phase accumulation of the propagating field without contributing to the net transfer of population between the optical ports. By comparing the prefactors derived previously, we find that the real part of the complex response is exactly twice the macroscopic reflection probability, $\mathrm{Re}[\mathcal{Z}(\Delta)] = 2\mathcal{P}_d$. This fundamental factor of 2 ensures the conservation of probability across the interferometer ports. Consequently, the full complex response yields the Faddeeva function $W(z)$ scaled by this additional factor:

$$\mathcal{Z}(\Delta) = 2\gamma\sigma\sqrt{\frac{\pi}{2}}W\left(\sqrt{2}\sigma\left(\Delta + i\frac{\gamma}{2}\right)\right) \tag{3.57}$$

With the complex transmission amplitude fully determined as $\mathcal{T} = 1 - \mathcal{Z}(\Delta)$, the effective macroscopic phase shift Φ_{eff} accumulated by the single photon is physically defined as the argument (or phase angle) of $\mathcal{T}$:

$$\Phi_{eff} = \arg(\mathcal{T}) = \arg\left(1 - \mathcal{Z}(\Delta)\right) \tag{3.58}$$

By separating $\mathcal{Z}(\Delta)$ into its real and imaginary parts, the accumulated phase shift can be explicitly written in terms of the standard arctangent function:

$$\Phi_{eff} = \arctan\left(\frac{-\mathrm{Im}[\mathcal{Z}(\Delta)]}{1-\mathrm{Re}[\mathcal{Z}(\Delta)]}\right) \tag{3.59}$$

This complete formulation highlights a crucial physical distinction between perturbative optics and the exact Waveguide QED regime. In standard weak-coupling scenarios, the macroscopic routing probability is negligible ($\mathrm{Re}[\mathcal{Z}] \ll 1$), and the effective phase shift simplifies to the purely dispersive term, $\Phi_{eff} \approx \arctan(-\mathrm{Im}[\mathcal{Z}]) \approx -\mathrm{Im}[\mathcal{Z}]$.

However, for a quantum emitter with a near-unity coupling efficiency to a nanophotonic waveguide (i.e., a β-factor approaching 1; in this respect, see Sect. 1.5), the dynamical interaction regime is fundamentally governed by the detuning Δ. Near resonance ($\Delta \approx 0$), the interaction becomes highly non-perturbative. Here, the real part of the response becomes macroscopic. Crucially, as dictated by energy conservation, $\mathrm{Re}[\mathcal{Z}(\Delta)]$ can exceed unity (reaching up to 2 in the monochromatic limit). Physically, this means the unscattered coherent background of the incident wavepacket, represented by $1 - \mathrm{Re}[\mathcal{Z}(\Delta)]$, is not merely depleted, but can be completely canceled and driven to negative values by the resonant scattering process. As this denominator shrinks, crosses zero, and becomes negative, the macroscopic transmission amplitude enters the left half of the complex plane. This dynamic allows the relative weight of the out-of-phase scattered component $-\mathrm{Im}[\mathcal{Z}(\Delta)]$ to be massively amplified, pushing the accumulated phase beyond the bounds of the standard right-half plane ($[-\pi/2, \pi/2]$).

Consequently, the accumulated phase is a highly non-linear response driven by the intricate coupling between absorption and dispersion. Conversely, as we scan the detuning far from resonance ($|\Delta| \gg \gamma$), the real part naturally vanishes, and the system smoothly transitions back to a purely dispersive, weakly interacting regime. This demonstrates how the finite bandwidth of the photon intertwines with the complex atomic polarizability, yielding a deterministic phase winding that sweeps across different physical quadrants as a function of Δ.

Chapter 4

Quantum MZI with a cavity-coupled qubit: numerical solution

4.1 Numerical framework: time-bin discretization

The time-bin formalism introduced in Section 2.4 provides a natural framework for the numerical simulation of single-photon scattering in waveguide-QED systems. The discretization of the continuous Fock state into N temporal modes of width Δt reduces the problem from a continuum of bosonic modes to a finite-dimensional Hilbert space, where the interaction between the propagating field and the localized quantum system is local in time, and can be computed step by step. In Chapter 3, this framework was exploited analytically to derive closed-form expressions for the scattering of a single-photon pulse off a TLS embedded in a MZI. The present chapter further extends this analysis to the case where the emitter is coupled to a single-mode optical cavity through the Jaynes–Cummings interaction, a configuration for which, to our knowledge, no analytical closed-form solution is available. A fully numerical approach is therefore required, and the time-bin discretization provides the best suited algorithmic backbone for this purpose.

4.1.1 Numerical process workflow

The computational procedure follows the collision model picture [Gro+18]: the propagating single-photon wavepacket is represented as a sequence of N time bins, each playing the role of an independent bath ancilla that interacts with the localized quantum system exactly once before being discarded. At every time step n, the interaction Hamiltonian H_n, constructed as a sparse matrix acting on the single-excitation subspace, is exponentiated over the interval Δt to yield the unitary propagator U_n.

The updated state vector is then obtained via the action $|\psi_n\rangle = U_n |\psi_{n-1}\rangle$, computed through a Krylov-subspace method (`expm_multiply` from the SciPy library) that evaluates the matrix-vector product $e^{-iH_n\Delta t}|\psi\rangle$ directly, without constructing the full matrix exponential (see Appendix F, line 4 for the import and the main loop for its repeated application). This sequential procedure is repeated for $n = 0, 1, \ldots, N-1$, producing the complete time evolution of the system one bin at a time.

A key simplification arises from restricting the dynamics to the single-excitation subspace. Since the initial state consists of one photon in the waveguide and the localized system in its ground state, the total excitation number is conserved by the Hamiltonian. At any time step n, the excitation can reside in one of the N waveguide time bins or in the internal degrees of freedom of the local system: the excited state $|e\rangle$ for the bare emitter, or the cavity mode and the qubit excited state for the Jaynes–Cummings (JC) configuration. In its most compact representation, the quantum state is therefore fully described by a vector of $N + d$ complex amplitudes, where d is the number of internal degrees of freedom ($d = 1$ for the TLS, $d = 2$ for the JC system). Specific implementations may adopt a larger, redundant layout, as discussed in Sect. 4.4. The corresponding Hamiltonian H_n at each step is a sparse matrix with $\mathcal{O}(1)$ non-zero off-diagonal entries, since only the n-th time bin couples to the local system at step n (see the functions `construct_H_n` and `construct_H_n_jc` in Appendix F, lines 103 and 128, respectively).

The accuracy of the time-bin discretization is controlled by the bin width Δt, which must be small enough to resolve the fastest dynamical scale in the problem. For a Gaussian wavepacket with temporal width σ, this translates into the requirement $\Delta t \ll \sigma$, ensuring that the pulse envelope is quasi-constant within each bin and that the piecewise-constant approximation of the Hamiltonian remains valid. The code enforces this condition explicitly through a runtime check (see Appendix F, lines 26 and 54). In the limit $\Delta t \to 0$, the discrete collision model recovers the continuous-time dynamics governed by the Lindblad master equation [Gro+18] [Cic17]. At finite Δt, the convergence has been verified systematically by Bundgaard-Nielsen et al. [Bun+25], who computed the integrated squared deviation between the numerical output wavefunction $\xi_{\text{out}}^{(N)}(t)$ and the exact analytical solution, $\varepsilon(N) = \int |\xi_{\text{out}}^{(N)}(t) - \xi_{\text{out}}^{\text{exact}}(t)|^2 \, dt$, and showed that this error decreases monotonically as the number of bins N is increased at fixed total simulation time.

The following sections apply this framework to two configurations of the MZI: first with a bare two-level emitter, where the numerical results are validated against an independent Runge–Kutta integration (Appendix E) and against the analytic solution derived in Chapter 3, and then with the full JC system.

4.2 Two-level system phase shifter: Hamiltonian construction and MZI assembly

The first system considered is the bare two-level emitter coupled directly to the waveguide, as treated analytically in Chapter 3. Within the time-bin framework introduced in Section 4.1, the interaction Hamiltonian at step n takes the form derived in Section 2.4:

$$H_n = i\hbar\sqrt{\frac{\Gamma}{\Delta t}}\left(\sigma^\dagger\, w_n - \sigma\, w_n^\dagger\right) + \hbar\Delta\,\sigma^\dagger\sigma, \tag{4.1}$$

where Γ is the spontaneous emission rate into the guided mode, $\Delta = \omega_p - \omega_0$ is the detuning between the photon carrier frequency and the emitter transition, and w_n is the annihilation operator for the n-th time bin. The coupling prefactor $i\sqrt{\Gamma/\Delta t}$ is the signature of the time-bin discretization discussed in Section 4.1. In the code, this prefactor is set as `pref = 1j * np.sqrt(Gamma/dt)` (Appendix F, line 115), as we work with $\hbar = 1$, and the full sparse Hamiltonian is assembled in block form by the function `construct_H_n` (line 103). The MZI requires a two-arm field representation. The state vector has dimension $1 + 2N$: one vacuum component, N amplitudes for the upper arm (waveguide a), and N for the lower arm (waveguide b) (Appendix F, line 66). The beam-splitter Hamiltonian for the n-th time bin reads

$$H_n^{\mathrm{BS}} = \frac{i\pi}{4\,\Delta t}\left(w_{b,n}^\dagger\, w_{a,n} - w_{a,n}^\dagger\, w_{b,n}\right), \tag{4.2}$$

whose exponentiation yields the Hadamard mixing matrix

$$e^{-iH_n^{\mathrm{BS}}\Delta t} = \frac{1}{\sqrt{2}}\begin{pmatrix} 1 & -1 \\ 1 & 1 \end{pmatrix} \tag{4.3}$$

in the subspace $\{|1_{a,n}\rangle,\, |1_{b,n}\rangle\}$ (Appendix F, line 82).

At each time step n, the simulation executes the three-stage MZI sequence: the first beam splitter splits the input photon between the two arms, the upper arm undergoes the TLS interaction governed by H_n in Eq. (4.1), and the second beam splitter recombines the two paths. The output amplitudes at the reflection and transmission ports are extracted after BS2 as $\xi_{\mathrm{refl}}(t_{n+1}) = \psi_{\mathrm{field}}[n+1]/\sqrt{\Delta t}$ and $\xi_{\mathrm{trans}}(t_{n+1}) = \psi_{\mathrm{field}}[N+n+1]/\sqrt{\Delta t}$, respectively. The integrated probabilities are then obtained as $P_{\mathrm{trans}} = \sum_n |\xi_{\mathrm{trans}}(t_n)|^2\,\Delta t$ and similarly for P_{refl} (Appendix F, function `run_one_tls`, line 197).

The validation of this numerical scheme is presented in the following section, where the results are compared with the closed-form solution derived in Chapter 3.

4.3 Two-level system phase shifter: numerical results and validation with analytic solution

As a preliminary validation step, the time-bin simulation was compared against an independent Runge–Kutta (RK4) integration of the Schrödinger equation in the continuum limit. The two methods show excellent agreement across the full parameter range explored. The details of this comparison are reported in Appendix E (Fig. E.1). Having established the consistency of the numerical framework, the simulation results are now systematically compared with the closed-form analytical solution derived in Chapter 3.

The simulations utilize a Gaussian input pulse where the full width at half maximum (FWHM) of the intensity profile, denoted as τ_g, is chosen as the fundamental unit of time. All physical parameters are subsequently expressed in a dimensionless form scaled by this reference. The input pulse is centered at $t_0/\tau_g = 5.0$. The numerical propagation is performed over a temporal grid with a step size of $\Delta t/\tau_g = 0.005$ and a total duration of $t_{\max}/\tau_g = 15.0$, which corresponds to $N = 3001$ time bins. Under this choice of units, the dimensionless spectral bandwidth of the pulse is $\Delta\omega_{\text{pulse}}\tau_g \approx 2.77$. The dimensionless spontaneous emission parameter $\Gamma\tau_g$ is varied across the values $\{0.5,\ 1.0,\ 1.45,\ 1.9,\ 3.0\}$. This selection spans from the weak-coupling regime to values well above the critical coupling condition $\Gamma_c\tau_g \approx 1.45$, where the forward-propagating field in the interaction arm is completely extinguished at resonance (Appendix D). Finally, the dimensionless emitter–field detuning $\Delta\tau_g$ is swept in the range $[-10, 10]$ with a step size of 0.1.

Figure 4.1 shows the scattered field intensity $|\xi_{\text{out}}(t)|^2$ on the interaction arm of the interferometer for three values of the dimensionless spontaneous emission parameter: $\Gamma\tau_g = 0.5$, 1.45, and 3.0. Each panel displays five dimensionless detunings $\Delta\tau_g = 0$, 1, 2, 3.5, 5 alongside the input Gaussian envelope (shaded area). Solid curves are the analytical solution of Chapter 3, while triangular markers are the time-bin simulation. The agreement is exact across the entire parameter space.

A common feature of all three panels is the progressive recovery of the input pulse shape as the detuning increases. The scattering response of the emitter is peaked at $\Delta\tau_g = 0$ and falls off as a Lorentzian with half-width $\Gamma\tau_g/2$. For $\Delta\tau_g \gg \Gamma\tau_g/2$ the emitter is effectively transparent. At smaller detunings, a larger fraction of the pulse spectrum overlaps with the emitter resonance and the output wavepacket becomes appreciably distorted. The crossover between these two regimes shifts to higher $\Delta\tau_g$ as $\Gamma\tau_g$ increases, following the broadening of the Lorentzian linewidth. At $\Gamma\tau_g = 0.5$, for instance, the curve at $\Delta\tau_g = 3.5$ nearly coincides with the input; at $\Gamma\tau_g = 3.0$ the same detuning still produces a visible deviation.

The physical origin of the distortion is apparent from the input–output relation

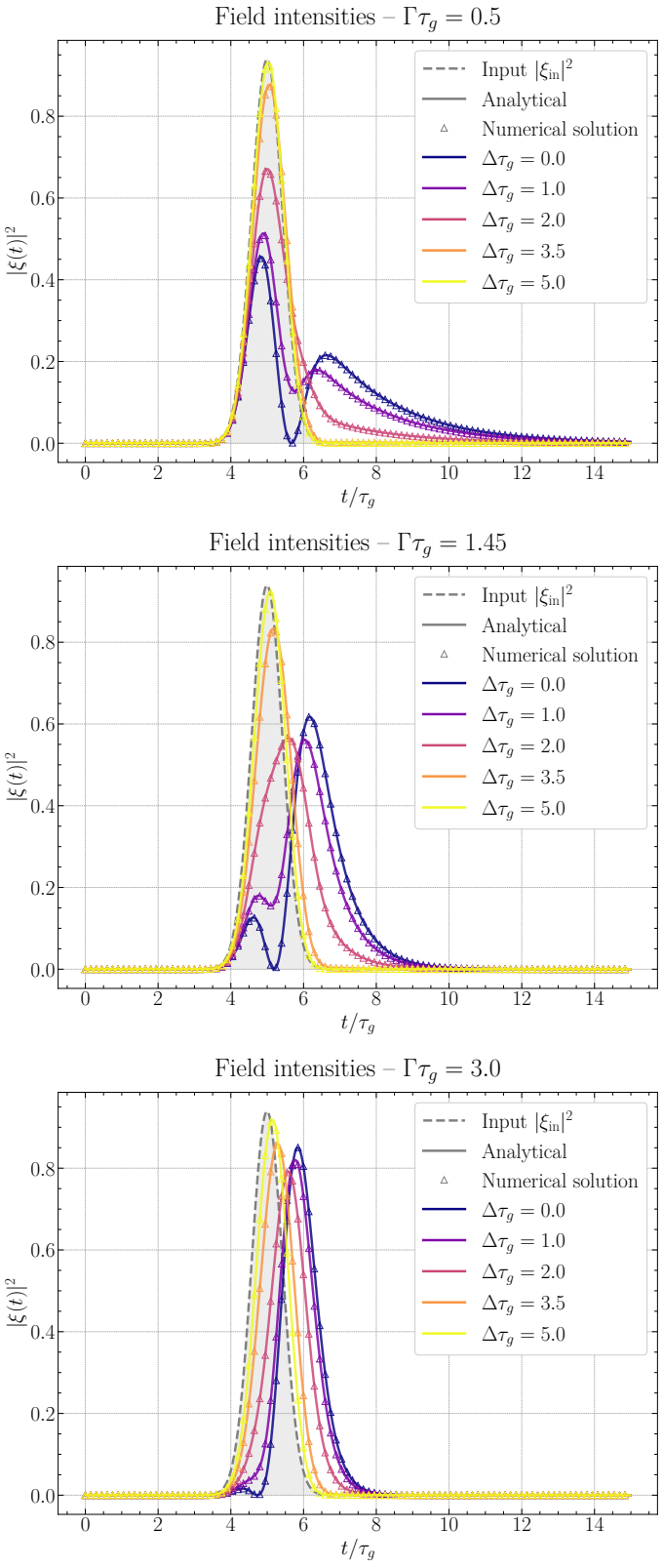

Figure 4.1: Scattered field intensity on the TLS within the interaction arm, quantified by $|\xi_{\text{out}}(t)|^2$, for $\Gamma\tau_g = 0.5$ (top), $\Gamma\tau_g = 1.45$ (middle), and $\Gamma\tau_g = 3.0$ (bottom), corresponding to $\Gamma/\Delta\omega_{\text{pulse}} \approx 0.18$, 0.52, and 1.08, respectively. Each panel shows results for five different values of dimensionless detuning ($\Delta\tau_g$); the shaded area is the input Gaussian envelope. Solid curves: analytic solutions (see Chapt. 3). Triangular markers: time-bin MZI simulation.

(Eq. 2.24): the output field is the superposition of the input and the re-emitted field, $\xi_{\text{out}}(t) = \xi_{\text{in}}(t) - \sqrt{\Gamma}\,\psi_e(t)$. At resonance ($\Delta\tau_g = 0$) the two contributions carry no relative phase. At a specific instant their amplitudes match exactly and the output intensity drops to zero. This complete destructive interference produces the characteristic double-peaked structure visible in all of the three panels at $\Delta\tau_g = 0$. For $\Delta\tau_g \neq 0$ the re-emitted field accumulates a phase $e^{-i(\Delta\tau_g)(t/\tau_g)}$ relative to the input, the cancellation is only partial, and the zero disappears.

The strength of the interaction is governed by the ratio $\Gamma/\Delta\omega_{\text{pulse}}$, where $\Delta\omega_{\text{pulse}} = \sqrt{2\ln 2}/\sigma$ is the spectral FWHM of the Gaussian wavepacket. At $\Gamma\tau_g = 0.5$ the emitter linewidth is much narrower than the pulse bandwidth and only a small spectral fraction interacts: the first peak remains comparable to the second. As $\Gamma\tau_g$ increases to 1.45, the coupling term $\sqrt{\Gamma}\,\psi_e$ grows faster and cancels the input more effectively, suppressing the first peak well below the second. The trend reaches its extreme at $\Gamma\tau_g = 3.0$, with $\Gamma/\Delta\omega_{\text{pulse}} \approx 1.08$, where the emitter is spectrally broader than the photon: nearly the entire pulse content falls within the resonance, the first peak is almost completely suppressed, and the output is dominated by the re-emission.

After the input pulse has passed, $\xi_{\text{in}} \to 0$ and the output reduces to $\xi_{\text{out}} = -\sqrt{\Gamma}\,\psi_e$. From Eq. (2.23), in the absence of the driving field the excitation amplitude decays as $\psi_e \propto e^{-(\Gamma\tau_g)(t/\tau_g)/2}$, so the output intensity falls off as $e^{-(\Gamma\tau_g)(t/\tau_g)}$. This exponential tail is the temporal signature of spontaneous emission into the guided mode. Its duration is set by the dimensionless lifetime $2/(\Gamma\tau_g)$: at $\Gamma\tau_g = 0.5$ the tail extends over several pulse widths, while at $\Gamma\tau_g = 3.0$ the re-emission is concentrated in a narrow window immediately following the input. The total energy carried by the tail grows with $\Gamma\tau_g$, since a broader linewidth captures a larger spectral fraction of the photon. However, this energy is released over a shorter time, yielding higher instantaneous intensity over a more compact interval.

A further effect visible in all panels, including the curves at large detuning where no double-peaked structure appears, is the systematic shift of the output wavepacket toward later times with respect to the input. This group delay is a direct consequence of the subtraction in Eq. (2.24): the re-emitted field $\sqrt{\Gamma}\,\psi_e(t)$ builds up with a finite response time set by the excitation dynamics of Eq. (2.23), and is therefore delayed relative to ξ_{in}. The resulting asymmetric subtraction suppresses the leading edge of the pulse more than the trailing edge, displacing the output envelope to later times. The effect is stronger at smaller detunings and larger $\Gamma\tau_g$, where the interaction is more intense.

Figure 4.2 displays the integrated detection probabilities at the two output ports of the interferometer — transmission P_c and reflection P_d — as functions of the dimensionless detuning $\Delta\tau_g$, for all five values of $\Gamma\tau_g$. These quantities are governed by the complex scattering response $\mathcal{Z}(\Delta\tau_g)$ derived in Section 3.6, with $P_d = \frac{1}{2}\text{Re}[\mathcal{Z}]$

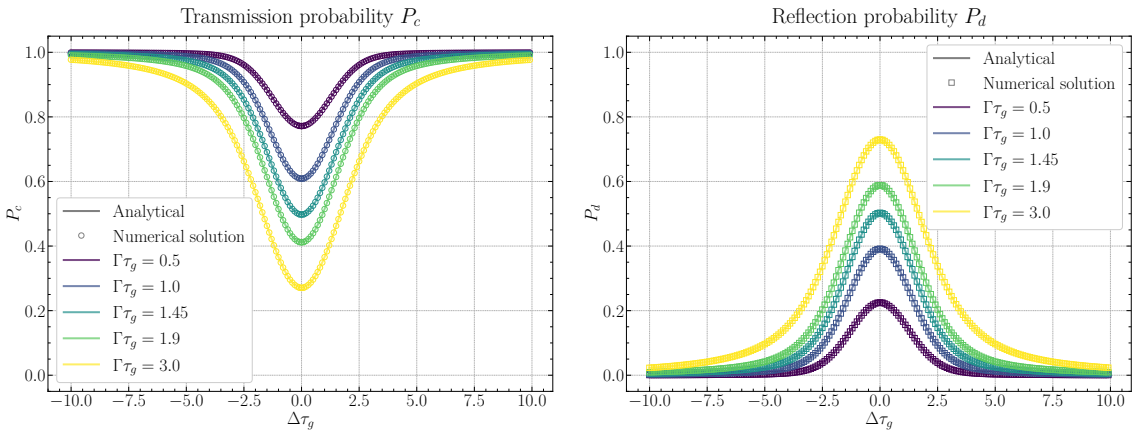

Figure 4.2: Transmission (P_c, left) and reflection (P_d, right) probabilities calculated at the output ports of the MZI as functions of the dimensionless detuning ($\Delta\tau_g$), for five different values of $\Gamma\tau_g$. Solid curves: analytic Faddeeva solution, as defined in Eq. (3.51). Open markers: results of the full time-bin MZI simulation.

and $P_c = 1 - P_d$; the factor $\frac{1}{2}$ originates from the two balanced beam splitters of the MZI. Solid curves correspond to the closed-form Faddeeva solution, Eq. (3.51). Open markers are the time-bin simulation and the agreement is exact over the full detuning range.

For $|\Delta\tau_g| \gg \Gamma\tau_g/2$ the scattering response vanishes, $\mathcal{Z} \to 0$, and the interferometer reduces to the balanced case with no differential phase between its arms: $P_c \to 1$ and $P_d \to 0$. Both figures confirm this limit. All five curves converge to $P_c \approx 1$ and $P_d \approx 0$ for $|\Delta\tau_g| \gtrsim 7$, regardless of $\Gamma\tau_g$. At resonance ($\Delta\tau_g = 0$) the interaction is strongest and a fraction of the photon is routed to the reflection port. The reflection probability $P_d(0)$ grows monotonically with $\Gamma\tau_g$, ranging from approximately 0.22 at $\Gamma\tau_g = 0.5$ to 0.73 at $\Gamma\tau_g = 3.0$. This trend is governed by the ratio $\Gamma/\Delta\omega_{\text{pulse}}$: a larger $\Gamma\tau_g$ broadens the Lorentzian linewidth of the emitter, so that a greater spectral fraction of the Gaussian wavepacket falls within the resonance and contributes to the scattering response. At $\Gamma/\Delta\omega_{\text{pulse}} \approx 1.08$ ($\Gamma\tau_g = 3.0$), however, the emitter linewidth only marginally exceeds the pulse bandwidth, and a sizeable portion of the photon spectrum still lies outside the resonance. The routing therefore remains incomplete. The analytical expression for $\mathcal{P}_d$ reported in Eq. (3.49) is the convolution of the Gaussian photon spectrum with the Lorentzian response of the emitter. In the monochromatic limit ($\Delta\omega_{\text{pulse}} \to 0$), the Gaussian acts as a spectral δ-function and samples the Lorentzian at its peak; the entire photon spectrum falls within the resonance and $P_d \to 1$. The narrow-bandwidth simulations reported below, performed with a five-fold reduction in the pulse bandwidth, confirm this trend.

Figure 4.3 shows the effective phase shift $\Phi_{\text{eff}} = \arg(1 - \mathcal{Z}(\Delta\tau_g))$ accumulated by the single photon after the scattering event, as predicted by Eq. (3.58). The profile

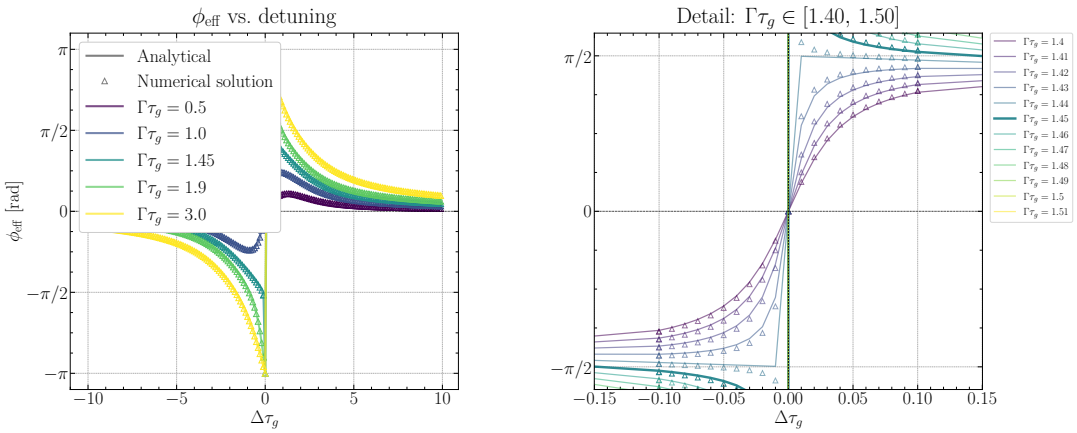

Figure 4.3: Effective phase shift Φ_{eff} as a function of the dimensionless detuning ($\Delta\tau_g$) calculated for five different values of $\Gamma\tau_g$ (left). The right panel details the transition near the critical coupling parameter $\Gamma_c\tau_g \approx 1.45$, with $\Gamma\tau_g$ swept in steps of 0.01. Solid curves: analytical Faddeeva solution. Triangular markers: time-bin MZI simulation.

is antisymmetric in $\Delta\tau_g$, reflecting the odd symmetry of the dispersive component of $\mathcal{Z}(\Delta\tau_g)$, and vanishes at large detuning where $\mathcal{Z} \to 0$. Solid curves are the analytical Faddeeva solution; triangular markers are the time-bin simulation. The agreement holds across the full parameter range, including the region near $\Delta\tau_g = 0$ where the phase varies rapidly.

The behaviour near $\Delta\tau_g = 0$ is governed by the ratio between $\Gamma\tau_g$ and the critical coupling parameter $\Gamma_c\tau_g$ (in this respect, see Appendix D). Below $\Gamma_c\tau_g$, the re-emitted field $\sqrt{\Gamma}\,\psi_e$ at resonance is weaker than the input; the transmitted field is reduced in amplitude but retains the same sign, and $\Phi_{\text{eff}}(0) = 0$. At $\Gamma\tau_g = \Gamma_c\tau_g \approx 1.45$ the two fields match exactly: the forward-propagating amplitude vanishes and the phase is undefined. Above $\Gamma_c\tau_g$, the re-emitted field exceeds the input and the subtraction in Eq. (2.24) overshoots the cancellation and the transmitted field acquires the opposite sign. This sign reversal corresponds to $\Phi_{\text{eff}}(0) = \pm\pi$, visible in the curves at $\Gamma\tau_g = 1.9$ and 3.0. The right panel of Figure 4.3 zooms into the region $\Gamma\tau_g \in [1.40, 1.51]$ near resonance. For $\Gamma\tau_g < \Gamma_c\tau_g$ the phase crosses zero smoothly at $\Delta\tau_g = 0$. As $\Gamma\tau_g$ increases toward $\Gamma_c\tau_g$, the transition becomes progressively sharper until, at $\Gamma\tau_g = 1.45$, a discontinuous jump appears with a slight inconsistency between the analytical and numerical curves in the immediate vicinity of the discontinuity. For $\Gamma\tau_g > \Gamma_c\tau_g$ the sign of the slope reverses and the phase at resonance settles to $\pm\pi$. This narrow scan provides a direct numerical confirmation of the critical coupling value derived analytically in Appendix D.

The same analysis is repeated with a five-fold reduction in the pulse spectral bandwidth. Figure 4.4 shows the transmission and reflection probabilities for $\Gamma\tau_g = 7.25$, 9.5, and 15.0, yielding $\Gamma/\Delta\omega_{\text{pulse}} \approx 2.6$, 3.4, and 5.4 respectively. At resonance,

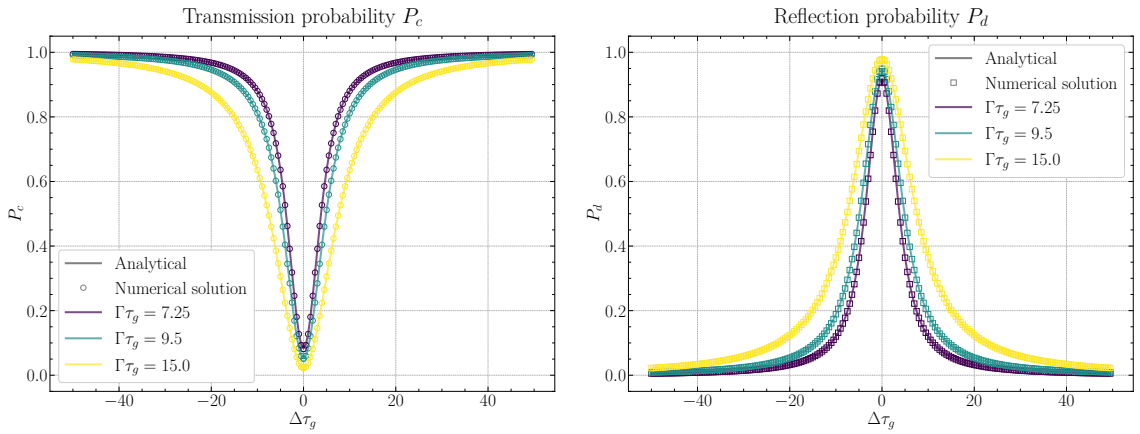

Figure 4.4: Transmission (P_c, left) and reflection (P_d, right) probabilities calculated at the output ports of the MZI for the narrower bandwidth case, considering three different values of $\Gamma\tau_g$. Solid curves: analytic Faddeeva solution (see Chapt. 3). Open markers: results of the full time-bin MZI simulation.

$P_d(0)$ approaches unity for all three values of $\Gamma\tau_g$, a marked increase over the broader bandwidth case. The profiles are also narrower in $\Delta\tau_g$, as the reduced spectral width of the photon resolves the Lorentzian lineshape with greater selectivity. This result admits a direct interpretation in the time domain.

A narrower bandwidth corresponds to a longer pulse in time, which drives the emitter for a duration well exceeding its dimensionless radiative lifetime, $2/(\Gamma\tau_g)$. The excitation amplitude, ψ_e, can therefore build up fully, and the re-emitted field, $\sqrt{\Gamma}\,\psi_e$, reaches the amplitude of the input pulse over its entire duration. The cancellation in Eq. (2.24) becomes nearly complete at resonance: the forward-propagating field is almost entirely extinguished and the photon is almost fully routed to the dark port.

Let us stress that the results of the time-bin simulation and the analytic Faddeeva solution are in excellent quantitative agreement across all the considered observables — wavepacket profiles, detection probabilities, and phase shifts — and over the entire parameter space explored. The quantum MZI response to a bare TLS as phase shifting element in one of the two arms already exhibits near-unity single-photon routing when the pulse bandwidth is sufficiently narrow. However, since it might be difficult to couple a single TLS to the waveguide mode with unit efficiency, in the next section we are going to extend the model of a quantum MZI to account for a Jaynes–Cummings Hamiltonian in the MZI arm, having in mind the single TLS embedded inside an optical resonator that is directly coupled to the waveguide. While the latter configuration might be easier to achieve experimentally with large waveguide-resonator coupling, the mode also introduces a further energy scale to the problem, namely the vacuum Rabi coupling g, to be considered as a further control parameter for our quantum MZI.

4.4 Jaynes–Cummings phase shifter: Hamiltonian construction and MZI assembly

The system considered in this section is the Jaynes–Cummings configuration of Sect. 2.5: a single-mode optical cavity is side-coupled to the waveguide at rate κ and exchanges excitations with a two-level qubit at the vacuum Rabi frequency g. The numerical framework of Sect. 4.1 applies without modification. What changes is the composition of the localized subsystem, which now hosts two internal degrees of freedom, the cavity mode and the qubit, rather than the single emitter of Sect. 4.2. The parameters of the first scan are collected in Appendix F. The cavity decay rate κ is established as the fundamental frequency scale, so that all physical quantities are expressed as dimensionless ratios. The vacuum Rabi coupling is swept across $g/\kappa \in \{0.1, 1.0, 5.0\}$ (Appendix F, line 39), spanning the bare-cavity limit, the Purcell regime ($g \ll \kappa$), the onset of strong coupling ($g \sim \kappa$), and the deep strong coupling regime ($g \gg \kappa$). The input Gaussian wavepacket, constructed by the function `pulse_shape` (Appendix F, line 61), has a dimensionless temporal standard deviation $\sigma\kappa = \sqrt{2\ln 2} \approx 1.18$, chosen so that its spectral FWHM matches the cavity linewidth, $\Delta\omega_{\mathrm{pulse}}/\kappa = \sqrt{2\ln 2}/(\sigma\kappa) = 1$. The pulse is centred at $\kappa t_0 = 9$ on a temporal grid with step $\kappa\Delta t = 0.02$ extending up to $\kappa t_{\max} = 30$, for a total of $N = 1501$ bins. Cavity and qubit are tuned to a common resonance, $\omega_c = \omega_0$, so that the scattering response depends on a single detuning $\Delta = \omega_p - \omega_c$ between the photon carrier and the cavity–qubit resonance, swept across $\Delta/\kappa \in [-8, 8]$ in steps of 0.05 (Appendix F, line 42) [Sch+07].

The handling of the localized subsystem differs from the bare-emitter case in the layout of the state vector. For the two-level system of Sect. 4.2, the dynamics was propagated on a $2(N+1)$-dimensional vector with a block structure separating a ground sector and an excited sector of $N+1$ components each, encoding the field in the upper arm together with the emitter state (`psi_tls` in `run_one_tls`, Appendix F, line 201). This representation is redundant. The conservation of the total excitation number restricts the physical dynamics to a subspace of minimal dimension $N+1$; the doubling to $2(N+1)$ in the implementation comes from writing the Hamiltonian as an explicit block matrix with separate ground and excited sectors. The Jaynes–Cummings simulation adopts instead the most compact representation compatible with the single-excitation constraint. The state vector `psi_sys` has dimension $N+2$: the first N entries store the photon amplitude in each waveguide bin, one entry tracks the cavity excitation, and one entry tracks the qubit excited state (Appendix F, lines 131–133 and 280). Despite carrying one extra internal degree of freedom relative to the TLS, the JC state vector is therefore smaller in dimension ($N+2$ against $2(N+1)$), which translates into a lighter Hamiltonian application

at each step.

Within the time-bin framework of Sect. 4.1, the Hamiltonian governing the local subsystem at step n takes the form

$$H_n^{\mathrm{JC}} = i\hbar\sqrt{\frac{\kappa}{\Delta t}}\,(a^\dagger w_n - w_n^\dagger a) + \hbar g\,(a^\dagger\sigma_- + \sigma_+ a) + \hbar\Delta\,(a^\dagger a + \sigma_+\sigma_-), \tag{4.4}$$

where a and $a^\dagger$ are the cavity ladder operators, $\sigma_\pm$ are the qubit raising and lowering operators, and w_n is the annihilation operator of the n-th waveguide time bin. The first term encodes the waveguide-cavity coupling, with the same $\sqrt{\kappa/\Delta t}$ prefactor signature of the time-bin discretization that appeared in the TLS case of Eq. 4.1 with Γ replaced by κ. The second term is the Jaynes–Cummings coupling, exchanging excitations between cavity and qubit at the vacuum Rabi rate g. No direct waveguide-qubit coupling is present. The qubit interacts with the propagating field only through the cavity, in accordance with the side-coupled architecture of Sect. 2.5. Both internal modes carry the same detuning Δ on the diagonal, as required by the condition $\omega_c = \omega_0$. In the code the sparse $(N+2)\times(N+2)$ Hamiltonian is assembled by the function `construct_H_n_jc` (Appendix F, line 128). The non-zero entries are four off-diagonal couplings at positions (n, N), (N, n), $(N, N+1)$, $(N+1, N)$ and two diagonal terms on the cavity and qubit slots (Appendix F, lines 142–148).

The MZI assembly is identical to the TLS case of Sect. 4.2. The two-arm field representation is unchanged. The field vector has dimension $1+2N$, with one vacuum component, N amplitudes for the upper arm and N for the lower arm (Appendix F, line 66). The beam-splitter Hamiltonian H_n^{BS} keeps the form of Eq. (4.2), with the same Hadamard mixing matrix on the subspace $\{|1_{a,n}\rangle, |1_{b,n}\rangle\}$. At each step n, the loop executes the three-stage sequence: the first beam splitter distributes the photon between the two arms, the upper arm evolves under H_n^{JC} of Eq. (4.4), and the second beam splitter recombines the two paths. The n-th bin amplitude is synchronised between ψ_{field} and ψ_{sys} before and after the JC step (Appendix F, lines 290 and 294). After BS2 the output amplitudes at the reflection and transmission ports are extracted as $\xi_{\mathrm{refl}}(t_{n+1}) = \psi_{\mathrm{field}}[n+1]/\sqrt{\Delta t}$ and $\xi_{\mathrm{trans}}(t_{n+1}) = \psi_{\mathrm{field}}[N+n+1]/\sqrt{\Delta t}$; the integrated probabilities $P_{\mathrm{trans}} = \sum_n |\xi_{\mathrm{trans}}(t_n)|^2 \Delta t$ and P_{refl} are accumulated as the loop proceeds (Appendix F, function `run_one_jc`, line 275). The internal cavity and qubit amplitudes are stored at each step (Appendix F, lines 296–297). The numerical results obtained with this scheme are presented in Sect. 4.5.

4.5 Numerical results for the quantum MZI with a Jaynes–Cummings phase shifter

The numerical results obtained with the simulation framework of Sect. 4.4 are now reported. The first set of scans explores the regime where the pulse bandwidth matches the cavity linewidth, $\Delta\omega_{\text{pulse}} = \kappa$. The parameter set matches the one specified in Sect. 4.4: $\sigma\kappa = \sqrt{2\ln 2} \approx 1.18$, $\kappa t_0 = 9$, $\kappa t_{\max} = 30$, $\kappa\Delta t = 0.02$. The dimensionless photon-cavity detuning Δ/κ is swept across $[-8, 8]$ in steps of 0.05.. The vacuum Rabi coupling takes three distinct values: $g/\kappa = 0.1, 1.0, 5.0$. These specific values sample the Purcell regime, the onset of strong coupling, and the deep strong coupling regime, respectively. The analysis first examines the scattered wavepacket on the JC arm. Then, it evaluates the output port amplitudes. Finally, it addresses the integrated detection probabilities and the effective phase shift as functions of Δ and g.

Figure 4.5 shows the scattered field intensity, calculated as $|\xi_{\text{out}}(t)|^2$, on the JC arm of the MZI interferometer for three different values of the vacuum Rabi coupling. Each panel displays three representative detunings, namely $\Delta = 0$, κ, and 5κ, alongside the input Gaussian envelope (shaded area). These three regimes evidently exhibit distinct dynamical signatures. They are detailed in the remainder of this section.

The three panels shown in Fig. 4.5 essentially cover all the cavity-emitter coupling regimes introduced in Sect. 2.5. For $g = 0.1\kappa$, the vacuum Rabi coupling remains well below the cavity decay rate. Consequently, the photon escapes back into the waveguide before the interaction can transfer the excitation to the qubit. The cavity and qubit eigenstates remain essentially decoupled. The qubit acts simply as a small perturbation that modifies the cavity scattering response through the Purcell effect [LMS15]. As g crosses the strong coupling threshold $g \gtrsim \kappa/4$, the cavity and qubit wave functions hybridize into two polariton eigenstates:

$$|\pm\rangle = \frac{1}{\sqrt{2}}\Big(|1_c, g\rangle \pm |0_c, e\rangle\Big). \tag{4.5}$$

These states possess energies $E_\pm = \pm g$ relative to the bare cavity-qubit resonance. They are separated by the vacuum Rabi splitting $2g$ [SF09; LMS15]. The middle panel ($g = \kappa$) sits at the onset of strong coupling, just above the threshold. The bottom panel ($g = 5\kappa$) represents the deep strong coupling regime, where the polaritons are well resolved relative to the cavity linewidth.

A notable feature in Fig. 4.5 is the double-peaked structure displayed by the $\Delta = \kappa$ curve in the middle panel ($g = \kappa$) and the $\Delta = 5\kappa$ curve in the bottom panel ($g = 5\kappa$). In both cases, the detuning matches one of the polariton frequencies,

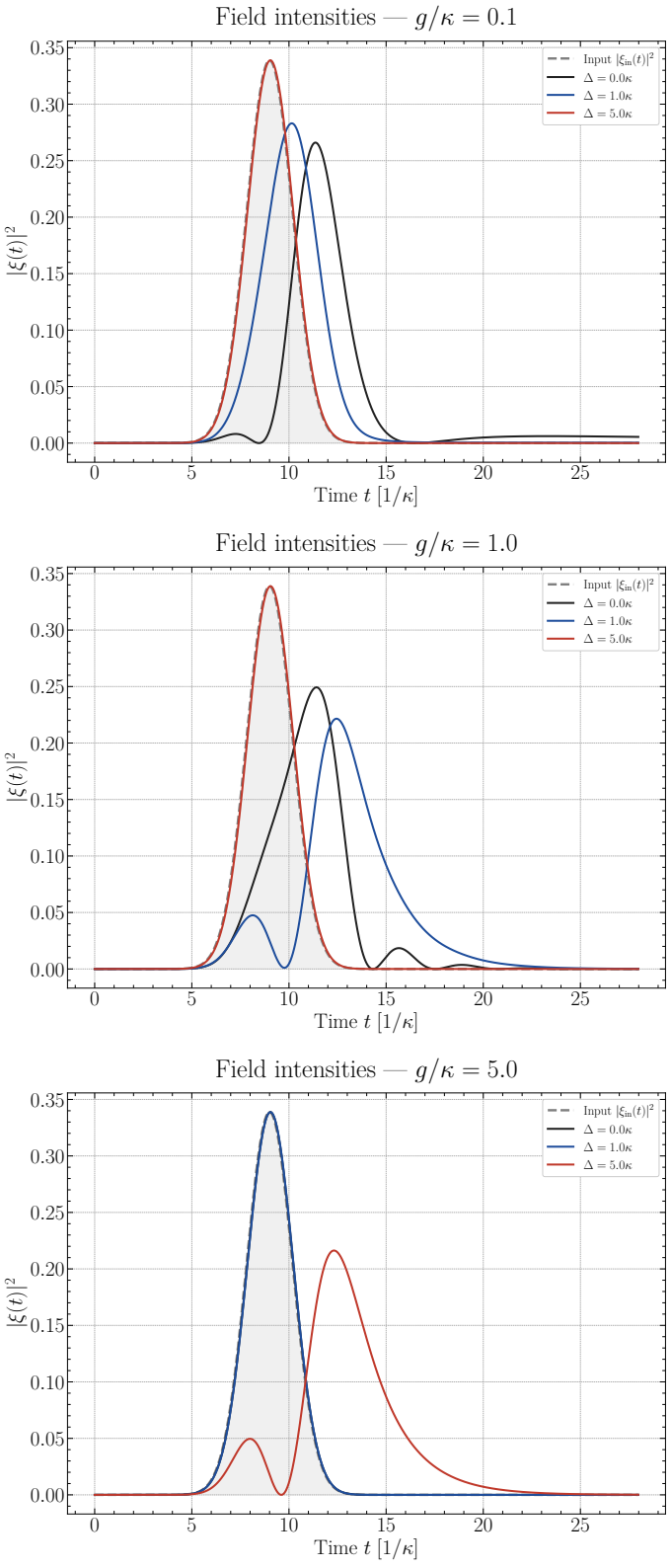

Figure 4.5: Scattered field intensities within the JC arm of the MZI, quantified by $|\xi_{\text{out}}(t)|^2$, calculated for $g/\kappa = 0.1$ (top, Purcell regime), 1.0 (middle, onset of strong coupling), and 5.0 (bottom, deep strong coupling), with the cavity linewidth fixed at $\kappa = 1$. Each panel shows three values of the detuning $\Delta = \omega_p - \omega_c$; the shaded area represents the input Gaussian envelope.

$\Delta = +g$. The output drops to nearly zero at $t \approx t_0$. It then reappears as a delayed re-emission peak, preceded by a small precursor at the leading edge. This specific pattern matches the results obtained for the resonant TLS in Sect. 4.3. The analogy is not coincidental. As demonstrated in Appendix G, when the input photon is tuned to a single-polariton resonance, the cavity-coupled qubit reduces to an effective two-level emitter. This effective emitter possesses a decay rate $\Gamma_{\text{eff}} = \kappa/2$ and is located spectrally at $\omega_c + g$ rather than at ω_c [SF09; LMS15]. The destructive interference observed in Sect. 4.3 is thus transposed from $\Delta = 0$ to $\Delta = \pm g$. The two panels at $(g, \Delta) = (\kappa, \kappa)$ and $(5\kappa, 5\kappa)$ appear nearly identical. This occurs because the temporal shape on a polariton resonance is determined by $\Gamma_{\text{eff}} = \kappa/2$ and by the ratio $\Gamma_{\text{eff}}/\Delta\omega_{\text{pulse}} = 1/2$, both of which are independent of g. The coupling g determines the polariton frequency. It does not affect the scattering dynamics once on resonance.

A complementary perspective on the role of g emerges from the response at $\Delta = 0$, when the photon is tuned exactly between the two polaritons. Three distinct behaviours appear, one per panel. At $g = 0.1\kappa$ (top, black curve), the polariton splitting $2g = 0.2\kappa$ is much smaller than the pulse bandwidth. Both polaritons are populated, but the Rabi exchange between cavity and qubit is too slow to develop before the photon escapes through the cavity. The output displays a single delayed peak with an exponential tail. This shape characterizes the Purcell-dominated scattering of a bare cavity [LMS15]. At $g = \kappa$ (middle, black curve), the polariton splitting matches the pulse bandwidth. Both polaritons are coherently excited, and their relative phase $e^{-i\,2gt}$ produces a beat in the cavity amplitude at the vacuum Rabi frequency. This manifests in the output as a slowly decaying oscillatory structure superimposed on the re-emission tail. Finally, at $g = 5\kappa$ (bottom, black curve), the splitting $2g = 10\kappa$ exceeds the pulse bandwidth by a factor of ten. Neither polariton is excited. The photon traverses the JC arm undisturbed, and the output is indistinguishable from the input envelope. This phenomenon corresponds to the cavity-induced transparency window of strongly coupled cavity QED [SF09; LMS15]. In the time domain, it appears as a vanishing scattering response between the two polariton resonances.

Figure 4.6 displays the integrated detection probabilities at the two output ports of the interferometer, P_c and P_d, as functions of the photon-cavity detuning Δ. The plots show three values of the coupling constant: $g/\kappa = 0.1$, 1, and 5. The two probabilities obey the conservation law $P_c + P_d = 1$ at each detuning point Δ. For values of $|\Delta|$ much larger than both κ and g, all three curves converge to full transmission, $P_c \to 1$, and zero reflection, $P_d \to 0$. Far from any internal resonance, the JC system becomes spectrally transparent. The interferometer simply recovers its balanced classical configuration, with no differential phase shift accumulating

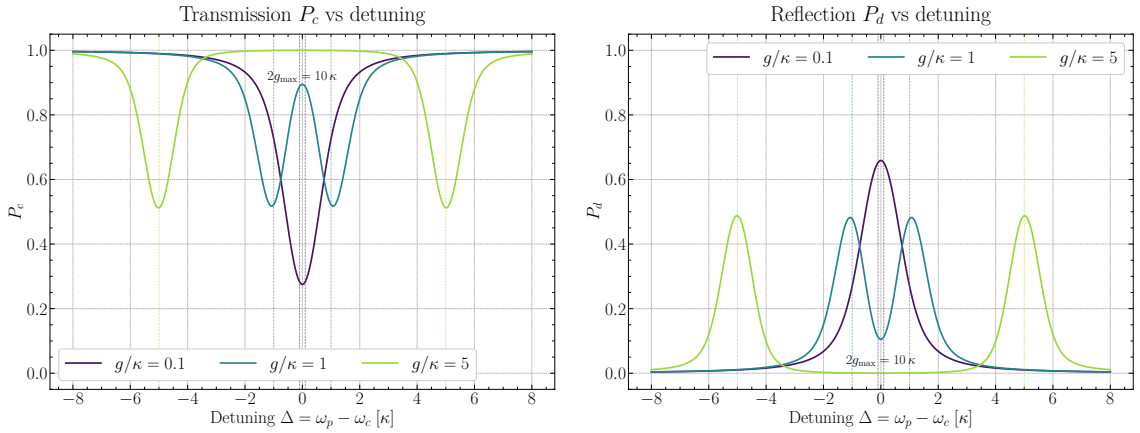

Figure 4.6: Transmission (P_c, left) and reflection (P_d, right) probabilities at the output ports of the MZI as functions of the photon-cavity detuning Δ/κ, for three values of the vacuum Rabi coupling g/κ. Vertical dashed lines mark the vacuum Rabi splitted resonances, i.e., occurring at $\Delta = \pm g$ for each curve. The two-headed arrow in the left panel highlights the vacuum Rabi splitting $2g_{\max} = 10\kappa$, corresponding to the deep strong coupling curve.

between the two arms.

The structure at smaller detunings $|\Delta|$ clearly separates the three coupling regimes. At $g = 0.1\kappa$, the response of P_c shows a single Lorentzian-like dip centered at $\Delta = 0$, with a width of approximately κ. The transmission drops below one-third. This minimum is mirrored by a single maximum in P_d, which approaches two-thirds. Here, the vacuum Rabi splitting $2g = 0.2\kappa$ is significantly smaller than the cavity linewidth and remains unresolved. The system responds essentially as a bare cavity weakly perturbed by the qubit. This represents the Purcell regime introduced in Sect. 2.5.1 [LMS15].

As the Rabi coupling increases to $g = \kappa$, the doublet structure typical of the JC anticrossing begins to emerge: P_c develops two distinct minima at $\Delta \simeq \pm g$ dropping to nearly one-half, separated by a partial transparency window over which transmission is mostly restored. Correspondingly, P_d exhibits two peaks at $\Delta \simeq \pm g$ that reach approximately one-half, accompanied by a local minimum near zero at $\Delta = 0$. Finally, at $g = 5\kappa$, the doublet is fully resolved. The two dips in P_c sit precisely at $\Delta = \pm 5\kappa$, separated by a broad unit-transmission window for $|\Delta| \lesssim 3\kappa$. In this regime, P_d shows two well-separated peaks of identical height, again near one-half. The separation between the dips, marked as $2g_{\max} = 10\kappa$ in the left panel, constitutes the direct spectral footprint of the vacuum Rabi splitting [SF09; LMS15].

A specific physical property emerges from the invariance of the P_d peak heights between $g = \kappa$ and $g = 5\kappa$. Both peaks saturate near one-half on the polariton resonances $\Delta = \pm g$, despite the fivefold change in coupling strength. This behavior fulfills the exact prediction of the effective TLS model derived in Appendix G. On

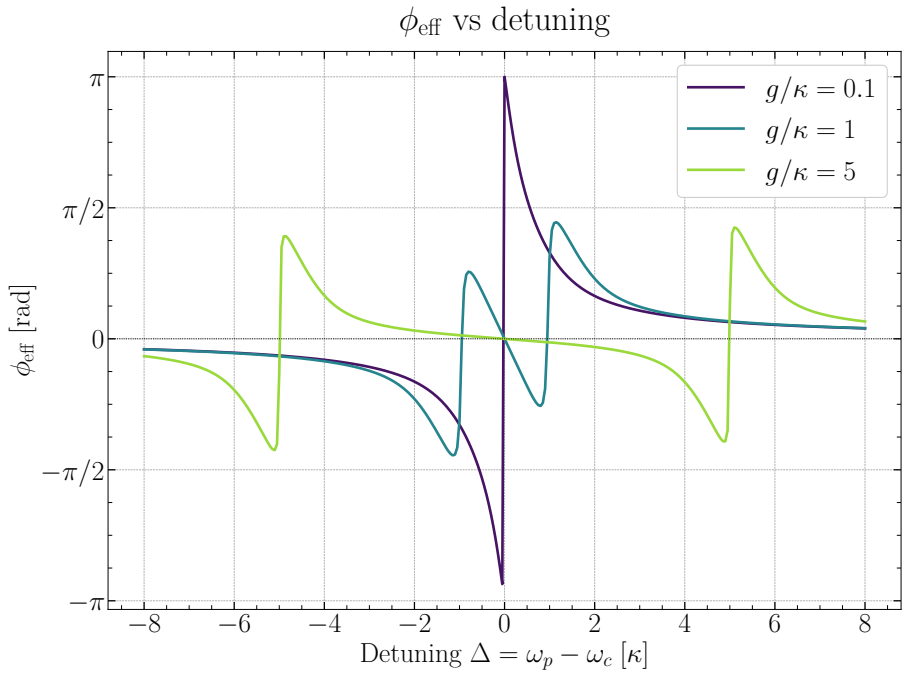

Figure 4.7: Effective phase shift, ϕ_{eff}, as a function of the photon-cavity detuning Δ/κ for $g/\kappa = 0.1$, 1.0, and 5.0, respectively. The phase response illustrates the transition from a single resonance profile to a well resolved polaritonic doublet in the strong coupling regime.

a single-polariton resonance, the cavity-coupled qubit behaves as an effective TLS with a decay rate of $\Gamma_{\text{eff}} = \kappa/2$. Consequently, the routing efficiency depends strictly on the ratio $\Gamma_{\text{eff}}/\Delta\omega_{\text{pulse}} = 1/2$, which is entirely independent of g. The coupling parameter g establishes the spectral position of the polaritons, but it does not dictate the magnitude of the scattering response at resonance.

The behavior at $g = 0.1\kappa$ stands apart. It clarifies the operational role of the strong coupling threshold. In the Purcell regime, the system reduces to a single effective emitter—the bare cavity weakly dressed by the qubit. Its effective linewidth is approximately $\Gamma_{\text{eff}} \approx \kappa$, resulting in a ratio $\Gamma_{\text{eff}}/\Delta\omega_{\text{pulse}} \approx 1$. Because the effective resonance is broad enough to accommodate the entire pulse bandwidth, the interaction maximizes the differential phase shift, leading to the high routing efficiency observed in the single central peak. The transition from $g = 0.1\kappa$ to $g \gtrsim \kappa$ therefore reduces the single-resonance routing efficiency (from near two-thirds down to one-half). In exchange, however, it splits the interferometric response into two distinct routing channels at $\Delta = \pm g$, creating one distinct port per polariton.

The physical mechanism responsible for the routing behavior observed in Fig. 4.6 is elucidated by analyzing the phase shift induced during the scattering process. Figure 4.7 illustrates the effective phase shift ϕ of the scattered field as a function of the photon-cavity detuning Δ for the three selected values of g/κ. The phase profiles demonstrate a direct map to the integrated detection probabilities, revealing how

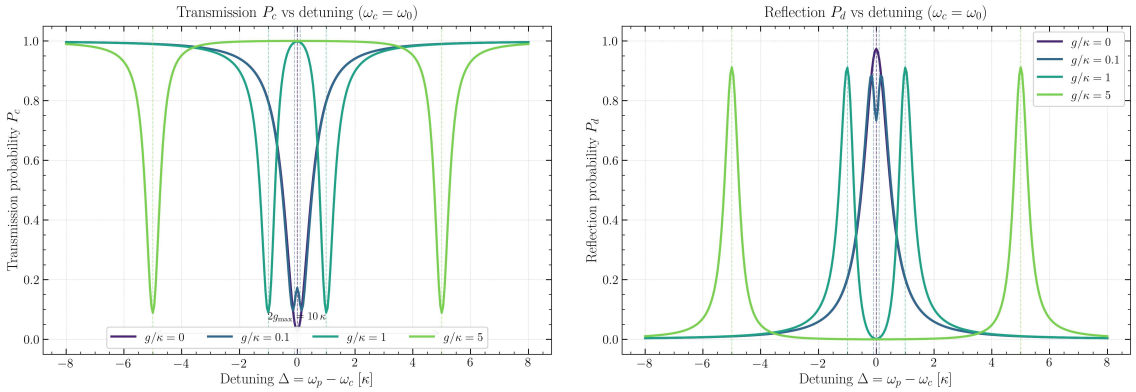

Figure 4.8: Transmission (P_c, left) and reflection (P_d, right) probabilities calculated in the narrow-bandwidth regime ($\Delta\omega_{\text{pulse}} = 0.2\kappa$) as functions of the photon-cavity detuning Δ/κ. The curves show the response for $g/\kappa = 0$, 0.1, 1.0, and 5.0, respectively.

the coherent light-matter coupling shapes the phase response of the interferometer.

At weak coupling ($g = 0.1\kappa$), the phase shift displays a single steep transition centered at $\Delta = 0$, where it reaches a maximum value of π. This behavior closely mirrors the resonant response of the bare two-level emitter discussed in Sect. 4.3. In this Purcell-dominated regime, the cavity and the qubit are not hybridized. The system acts essentially as a single over-coupled scattering center. Because the entire pulse bandwidth sits within this broad effective resonance, the incoming wavepacket experiences a full inversion of its phase profile at zero detuning. This phase jump of π maximizes the differential phase between the two arms of the MZI, explaining the high routing efficiency into port P_d observed in Fig. 4.6.

As the coupling strength increases beyond the threshold, the single phase jump splits into two distinct features centered at the polariton frequencies $\Delta = \pm g$, while the maximum phase shift at these resonances drops from π to $\pi/2$. This reduction is explained by the effective two-level emitter picture established in Appendix G. At strong coupling, the excitation is shared equally between the cavity mode and the qubit. Since only the cavity component couples directly to the waveguide, the effective interaction strength of each resolved polariton channel is halved. Each polariton resonance acts as an isolated, under-coupled mode. On exact resonance with a single polariton ($\Delta = \pm g$), this reduction caps the phase contribution at $\pi/2$. At detuning $\Delta = 0$, the phase drops back to zero. In this condition, the photon is tuned exactly between the two polaritons, experiencing equal and opposite phase pulls that cancel each other out. This flat zero-phase region for $g = 5\kappa$ directly accounts for the broad unit-transmission window seen in P_c.

To fully evaluate the operational performance of the interferometer, the scattering dynamics are investigated in the narrow-bandwidth regime. Figure 4.8 presents the integrated transmission (P_c) and reflection (P_d) probabilities for a pulse band-

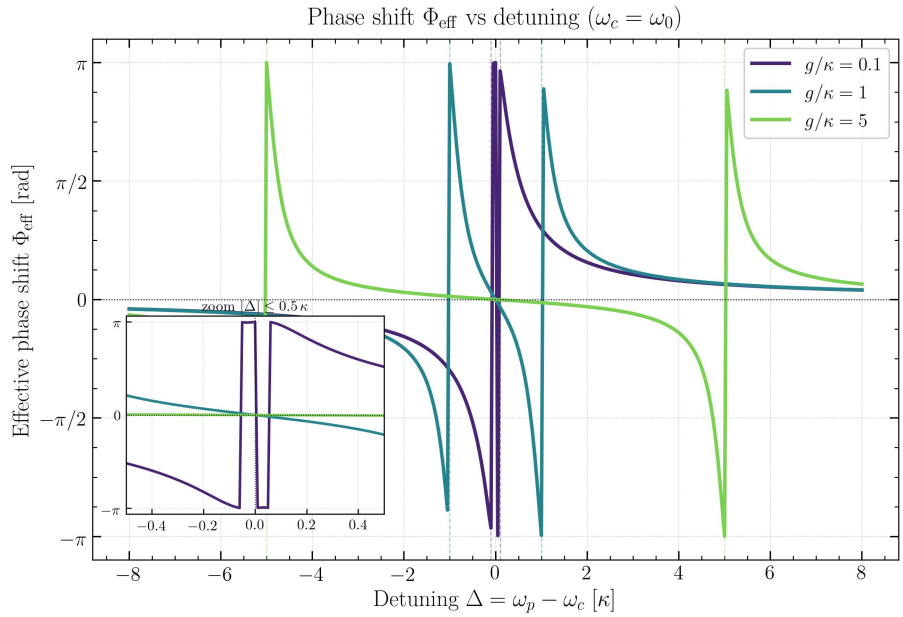

Figure 4.9: Effective phase shift, ϕ_{eff} as a function of the photon-cavity detuning Δ in the narrow-bandwidth regime ($\Delta\omega_{\text{pulse}} = 0.2\kappa$). The steep phase transitions at the polariton frequencies $\Delta = \pm g$ enable the high routing efficiencies observed in the strong coupling regime.

width reduced to $\Delta\omega_{\text{pulse}} = 0.2\kappa$. This spectral narrowing alters the interaction, moving the system toward a quasi-monochromatic probing configuration. The analysis includes the uncoupled baseline case ($g = 0$) to benchmark the routing performance against a bare cavity.

For $g = 0$, the photon interacts exclusively with the bare cavity resonance of width κ. Since the pulse bandwidth is much narrower than the cavity linewidth, the entire wavepacket fits inside the resonance curve. At zero detuning ($\Delta = 0$), the interaction introduces a phase shift close to π. This optimal phase differential routes the photon almost entirely to the reflection port. Consequently, P_d approaches unity while P_c drops near zero, demonstrating the maximum routing efficiency of the bare cavity under monochromatic conditions.

The narrow-bandwidth configuration reveals its high sensitivity when weak coupling is introduced at $g = 0.1\kappa$. In the previous broadband case, the vacuum Rabi splitting was hidden because the pulse covered both polaritons at once. Now, the pulse bandwidth $\Delta\omega_{\text{pulse}} = 0.2\kappa$ matches the polariton separation $2g = 0.2\kappa$. The incoming packet is spectrally narrow enough to resolve the individual light-matter states. As a result, the single central peak splits into an emerging doublet. Two distinct minima appear in P_c at $\Delta = \pm 0.1\kappa$, mirrored by two corresponding peaks in P_d. This feature confirms that the device acts as a sensitive, frequency-selective router even at low coupling strengths.

When the system enters the strong coupling regime ($g = \kappa$ and $g = 5\kappa$), the po-

lariton resonances separate completely. According to the effective description, each polariton possesses a decay rate of $\Gamma_{\text{eff}} = \kappa/2 = 0.5\kappa$. The narrow pulse bandwidth (0.2κ) is smaller than this individual linewidth, yielding a ratio of $\Gamma_{\text{eff}}/\Delta\omega_{\text{pulse}} = 2.5$. Each isolated polariton channel operates in an over-coupled condition. The routing efficiency at the polariton frequencies $\Delta = \pm g$ is significantly enhanced. The reflection probability P_d easily exceeds the one-half threshold, climbing toward higher routing values. The peak heights for $g = \kappa$ and $g = 5\kappa$ reach identical maximum values on resonance. This invariance confirms that the coupling strength dictates the spectral tuning of the routing channels without reducing their maximum efficiency.

The corresponding phase response confirms this physical picture. Figure 4.9 displays the effective phase shift ϕ for the narrow-bandwidth regime. Because the pulse is now spectrally confined, it probes the resonances with high resolution. For $g = \kappa$ and $g = 5\kappa$, the phase transitions at $\Delta = \pm g$ are no longer capped at $\pi/2$. Instead, they exhibit steep profiles that approach a full π shift. This occurs because the narrow pulse bandwidth (0.2κ) is fully contained within the effective polariton linewidth (0.5κ). Unlike the broadband case, the entire wavepacket accumulates a uniform phase inversion without its spectral tails being rejected. This nearly uniform π phase shift maximizes the interferometric contrast. It perfectly accounts for the high routing efficiency P_d observed at the polariton frequencies. The phase analysis thus provides a consistent explanation for the high-efficiency routing capabilities of the device in the quasi-monochromatic limit.

4.6 Dimensional mapping and experimental feasibility

The simulations presented in this thesis work are all displayed in dimensionless units, with the temporal FWHM of the input wavepacket (i.e., τ_g) serving as the fixed reference scale. All the physical observables — detection probabilities, phase shifts, and output wavepacket profiles — depend on the dimensionless ratio $\Gamma/\Delta\omega_{\text{pulse}}$ rather than on Γ and $\Delta\omega_{\text{pulse}}$ independently. A given ratio can therefore be realized either by changing the emitter linewidth at a fixed pulse bandwidth, as done to explore the parameter space in Section 4.3, or by adjusting the pulse duration for a fixed quantum dot.

To assess the experimental accessibility of the explored parameter range, we have adopted the latter perspective. Staunstrup et al. [Sta+24] report linewidths of $\Gamma \approx 1.45$ and 1.95 GHz for the two dipole transitions of an InGaAs quantum dot inside a GaAs photonic crystal waveguide at 4 K base temperature. Taking $\Gamma \approx 1.5$ GHz as a representative value, Table 4.1 lists the pulse bandwidth and duration corresponding to each configuration explored in the numerical simulations reported in this Chapter.

Table 4.1: Mapping of the dimensionless simulation parameters onto physical units, assuming a representative emitter linewidth of $\Gamma = 1.5$ GHz consistent with the InGaAs quantum dot characterized, e.g., in Ref. [Sta+24]. The first column links directly to the dimensionless coupling parameters $\Gamma\tau_g$ used in the numerical figures. Since the scattering response depends strictly on the ratio $\Gamma/\Delta\omega_{\text{pulse}}$, each entry can equivalently be realized by varying Γ at a fixed bandwidth, or by varying the pulse duration τ_g for a fixed value of Γ.

$\Gamma\tau_g$ (Sim.)	$\Gamma/\Delta\omega_{\text{pulse}}$	$\Delta\omega_{\text{pulse}}$ [GHz]	τ_g [ns]
0.5	0.18	8.3	0.33
1.0	0.36	4.2	0.66
1.45	0.52	2.9	0.96
1.9	0.69	2.2	1.3
3.0	1.08	1.4	2.0
7.25	2.62	0.57	4.9
9.5	3.43	0.44	6.3
15.0	5.42	0.28	10

The physical values span from sub-nanosecond pulses in the weak-interaction regime ($\Gamma\tau_g = 0.5$) to $\tau_g \approx 10$ ns in the near-unity routing regime ($\Gamma\tau_g = 15.0$). All derived durations fall within the range of current nanophotonic experiments, confirming that the transition from partial to near-complete single-photon routing predicted by the numerical model is accessible using existing technology.

A comparable dimensional mapping applies to the Jaynes–Cummings interferometric results discussed in Sections 4.4 and 4.5. In those simulations, the cavity decay rate κ dictates the primary physical scale. To establish a realistic experimental context, this parameter can be directly linked to the values derived in Table 4.1. The broadband scattering condition $\Delta\omega_{\text{pulse}} = \kappa$ was simulated using a reference pulse. Selecting the $\tau_g = 2.0$ ns entry yields a physical cavity linewidth of $\kappa = 1.4$ GHz.

This fixed cavity decay rate directly scales the interaction parameters. Table 4.2 details the physical frequencies for the three coupling regimes explored. The vacuum Rabi coupling g ranges from 140 MHz in the weakly coupled Purcell regime to 7.0 GHz deep within the strong coupling limit. Such values align well with standard experimental capabilities for quantum dots embedded in photonic crystal cavities or micropillars [LMS15].

The narrow-bandwidth scattering scenario requires a pulse spectrally five times narrower than the cavity resonance. Imposing $\Delta\omega_{\text{pulse}} = 0.2\kappa$ results in a physical bandwidth of 0.28 GHz. This value perfectly matches the 10 ns pulse duration already listed in Table 4.1. The detuning sweeps Δ scale proportionally, requiring laser tuning ranges on the order of a few tens of GHz. The entire parameter space investigated in the JC simulations is thus experimentally accessible. This scaling consistency confirms the feasibility of implementing highly efficient, frequency-selective

Table 4.2: Mapping of the dimensionless Jaynes–Cummings parameters onto physical units. The cavity linewidth is fixed at $\kappa = 1.4$ GHz to match the broadband pulse condition $\Delta\omega_{\text{pulse}} = \kappa$ corresponding to a $\tau_g = 2.0$ ns duration. The table provides the physical values for the coupling strength g and the resulting vacuum Rabi splitting $2g$ across the three simulated regimes.

JC Regime	g/κ	g [GHz]	$2g$ [GHz]
Purcell	0.1	0.14	0.28
Onset of strong coupling	1.0	1.4	2.8
Deep strong coupling	5.0	7.0	14.0

photon routing with current nanophotonic solid-state architectures.

The required spectral detuning provides a final validation of the experimental feasibility. Consider the narrow-bandwidth routing configuration at the onset of strong coupling ($g = \kappa$). The dimensional mapping fixes the polariton resonances at $\Delta = \pm g = \pm 1.4$ GHz. To activate the routing channel, the central frequency of the incoming single-photon pulse and the resonance of the target state must be precisely matched. Rather than sweeping the optical frequency of the excitation laser, standard experimental protocols keep the laser carrier fixed and tune the transition energy of the emitter. For InGaAs quantum dots embedded in nanophotonic structures, this is routinely achieved via the DC Stark effect by using local electrical contacts (see, e.g., Ref. [Hal+18]). The works present in the literature demonstrate that electrical gating can induce resonance shifts well exceeding 0.3 meV, which translates to over 70 GHz in the frequency domain. A required shift of 1.4 GHz (approximately 6 μeV) falls well within the easily accessible linear regime of the Stark tuning curve. Because standard precision voltage sources provide sub-millivolt resolution, the resulting spectral tuning rate of a few tens of megahertz per millivolt guarantees exact positioning on the polariton resonance. Targeting the specific polariton frequencies to maximize the interferometric routing efficiency is therefore fully compatible with modern laboratory capabilities.

Conclusions

This thesis has presented a complete theoretical treatment of a Mach-Zehnder interferometer in which the phase shift in one arm is induced by the interaction of a single propagating photon with a quantum system: a "quantum MZI". Two configurations have been analyzed for the phase-shifting arm of the interferometer: a two-level system coupled directly to the waveguide, for which an exact analytical solution has been derived, and a Jaynes-Cummings system in which the emitter is embedded within a single-mode optical cavity, which is in turn side-coupled to the waveguide arm, treated numerically within the time-bin framework. In both cases, the interferometer translates the phase and amplitude modifications imprinted by the scattering process into measurable routing probabilities at the two output ports.

For the single two-level emitter case, the single-photon scattering problem has been solved analytically by integrating the equation of motion for the emitter's excitation amplitude driven by a Gaussian wavepacket. The resulting closed-form expression, written in terms of the error function with complex argument, captures the full time-domain dynamics of the interaction including both the finite-bandwidth effects as well as the phase modulation induced by the detuning. The macroscopic routing probability at the reflection port, $\mathcal{P}_d$, has been shown to reduce to the real part of the Faddeeva function — a Voigt profile encoding the convolution of the Gaussian photon spectrum with the Lorentzian response of the emitter. The effective phase shift accumulated by the single propagating photon across the interferometer, Φ_{eff}, has been derived as the argument of the complex transmission amplitude $\mathcal{T} = 1 - \mathcal{Z}(\Delta)$, where $\mathcal{Z}(\Delta)$ is fully determined by the same Faddeeva function. The numerical time-bin simulation and an independent Runge-Kutta integration faithfully reproduce the analytical results across the entire parameter space. The interferometer response is controlled by the dimensionless coupling parameter $\Gamma\tau_g$. In the weak-coupling regime ($\Gamma\tau_g = 0.5$), only a small spectral fraction of the photon interacts with the emitter and the routing remains partial. As $\Gamma\tau_g$ increases, a critical coupling condition is reached at $\Gamma_c\tau_g \approx 1.45$, where the forward-propagating field in the interaction arm is completely extinguished at resonance. Beyond this threshold, the re-emitted field exceeds the input amplitude and the effective phase shift undergoes a π discontinuity. In the narrow-bandwidth limit ($\Gamma\tau_g = 15.0$), the

photon is routed from the transmission port to the reflection port with near-unity efficiency.

For the case in which a Jaynes-Cummings system is placed in the phase shifting arm of the interferometer, the time-bin simulation has been adopted as the primary computational tool, due to the fact that an analytic approach would have been highly non-trivial, if not intractable. The cavity decay rate into the single-mode waveguide, here indicated as κ, sets the natural frequency scale of the problem, and the interferometer response has been explored as a function of the photon-cavity detuning, Δ/κ, as well as the vacuum Rabi coupling, g/κ, across three different regimes: weak coupling, i.e., Purcell enhanced emitter ($g = 0.1\kappa$), onset of strong coupling ($g = \kappa$), and deep strong coupling ($g = 5\kappa$) regimes, respectively. In the Purcell regime, the system responds as a single broadened resonance, and the routing efficiency at $\Delta = 0$ reaches approximately two-thirds. As g increases beyond $\kappa/4$ (set by the Jaynes–Cummings transition point), the transmission spectrum develops two distinct minima at $\Delta = \pm g$, separated by the vacuum Rabi splitting $2g$, with two corresponding maxima in P_d. The reflection probability on each polariton resonance saturates near one-half, independently of g — a result explained by the reduction to an effective two-level emitter with decay rate $\Gamma_{\text{eff}} = \kappa/2$, as derived in Appendix G. In the narrow-bandwidth regime ($\Delta\omega_{\text{pulse}} = 0.2\kappa$), the pulse resolves the individual polariton channels and the phase shift at $\Delta = \pm g$ approaches π, driving the routing efficiency well above one-half. The dimensional mapping onto physical units confirms that the entire parameter space explored in the simulations is accessible with current InGaAs quantum dot technology in photonic crystal waveguides and cavities.

The theoretical framework developed here relies on a set of idealized assumptions that should be kept in mind when contextualizing the results. The waveguide is treated as lossless, the beam splitters as perfectly balanced, and the quantum emitter as purely radiative — non-radiative decay channels, pure dephasing induced by phonon scattering, and imperfect light-matter coupling have been explicitly excluded from the Hamiltonian. Intrinsic propagation losses in the interferometric arms and the non-ideal behavior of the beam splitters would further reduce the absolute detection probabilities at the output ports. In a realistic solid-state environment, these mechanisms inevitably broaden the spectral features and lower the routing efficiency below the ideal values reported in the simulations. Nevertheless, the core physical mechanism remains robust. The transition from a single-resonance (Purcell) regime to a resolved polaritonic doublet dictates the fundamental routing dynamics, and the phase-driven redistribution of the photon between the output ports is a general consequence of the Jaynes-Cummings interaction that survives moderate decoherence. The dimensional mapping presented in Section 4.6 confirms that the physical parameters required to observe these effects — nanosecond pulse

durations, emitter linewidths in the few GHz range, and vacuum Rabi couplings ranging from hundreds of MHz to several GHz — fall within the reach of current nanophotonic experiments on InGaAs quantum dots embedded in photonic crystal waveguides [Sta+24; LMS15]. The electrical tunability of the quantum dot transition via the DC Stark effect, with demonstrated tuning ranges well exceeding the required spectral shifts, provides a practical route to position the system precisely on the target polariton resonance [Hal+18].

Several directions for future work emerge naturally from this study. A first extension concerns the two-excitation sector of the Jaynes-Cummings Hamiltonian, in which two photons are simultaneously injected into the Mach-Zehnder interferometer. In this regime, the nonlinear saturation of the emitter produces photon-number-dependent scattering amplitudes: the response to a two-photon wavepacket differs from the single-photon case, as the emitter cannot absorb a second photon while it is in the excited state. The interferometric geometry would then map these amplitude differences into correlations between the two output ports, providing a direct route to investigate the Hong-Ou-Mandel effect in the presence of a quantum emitter. The interplay between photon indistinguishability and emitter-mediated nonlinearity may alter the bunching statistics with respect to the passive beamsplitter case, and the time-bin framework employed in this thesis can be extended to handle the two-excitation Hilbert space without modification of the underlying algorithmic structure. On the applied side, the device studied in this thesis represents a single unit cell of the mesh architectures underlying quantum photonic neural networks [Ste+19; Ewa+23], where tunable Mach-Zehnder interferometers with single-site nonlinearities constitute the elementary computational building block. The characterization of the single-photon routing efficiency and its dependence on the system parameters carried out in this work may therefore set the basis for the design of such networks at the level of the individual nonlinear interferometric nodes behaving quantum mechanically.

Appendix A

Derivation of the Equations of Motion and the Input–Output Relation

The state $|\psi_{k-1}\rangle$ describes the joint system composed of the emitter and the field after the emitter has interacted with the first $(k-1)$ time bins of the waveguide field, but before it interacts with the k-th bin.

$$|\psi_{k-1}\rangle = \sum_{j\geq k} \sqrt{\Delta t}\, \xi(t_j)\, |g\rangle|1_j\rangle + \psi_e(k-1)\, |e\rangle|\emptyset\rangle \tag{A.1}$$

In other words, the bins with indices $j < k$ correspond to portions of the photonic pulse that have already interacted with the emitter and possibly been scattered, while the bins with $j \geq k$ represent the remaining part of the pulse that has not yet reached the emitter. At this stage, the emitter may be found either in its excited state, with probability amplitude $\psi_e(k-1)$, or in the ground state, correlated with the unscattered portion of the field.

Recalling Eq. (2.20), we can derive the effect of the unitary evolution on the two relevant subspaces, $|g\rangle|1_k\rangle$ and $|e\rangle|\emptyset\rangle$:

$$U_k|e\rangle|\emptyset\rangle = \left(1 - \frac{\gamma}{2}\Delta t\right)|e\rangle|\emptyset\rangle - \sqrt{\gamma\Delta t}\,|g\rangle|1_k\rangle, \tag{A.2}$$

$$U_k|g\rangle|1_k\rangle = |g\rangle|1_k\rangle + \sqrt{\gamma\Delta t}\,|e\rangle|\emptyset\rangle. \tag{A.3}$$

Following the interaction with the k-th time bin, the system state evolves as

$$|\psi_k\rangle = \sqrt{\Delta t}\,\xi_{\text{out}}(t_k)\,|g\rangle|1_k\rangle + \psi_e(k)\,|e\rangle|\emptyset\rangle = U_k\,|\psi_{k-1}\rangle. \tag{A.4}$$

Where we can separate the different contributions as follows: the future bins $(j > k)$ do not interact and therefore remain unchanged, the current bin $(j = k)$ evolves

according to Eq. (A.2)- (A.3), and the excited state also evolves under the same equations. By evaluating the evolution of the $(k-1)$-th state and collecting the coefficients of the two subspaces, we obtain:

$$\psi_e(k) = \left(1 - \frac{\gamma}{2}\Delta t\right)\psi_e(k-1) + \sqrt{\gamma}\Delta t\,\xi(t_k), \tag{A.5}$$

$$\sqrt{\Delta t}\,\xi_{\text{out}}(t_k) = \sqrt{\Delta t}\,\xi(t_k) - \sqrt{\gamma\Delta t}\,\psi_e(k-1). \tag{A.6}$$

By dividing by Δt and taking the limit $\Delta t \to 0$, we obtain the Eq. (2.23) [HJE20]:

$$\frac{d\psi_e(k-1)}{dt} = -\frac{\gamma}{2}\psi_e(k-1) + \sqrt{\gamma}\,\xi(t_k) \tag{A.7}$$

and the well-known input-output relation in Eq. (2.24) [HJE20; GC85]:

$$\xi_{\text{out}}(t_k) = \xi(t_k) - \sqrt{\gamma}\,\psi_e(k-1) \tag{A.8}$$

Appendix B

The Faddeeva Function and the Voigt Profile in Waveguide QED

The Faddeeva function, also known as the complex error function, is a special function of fundamental importance across various branches of physics, including spectroscopy, plasma kinetics, and radiative transfer. Mathematically, it is defined as a scaled complex complementary error function:

$$w(z) = e^{-z^2}\mathrm{erfc}(-iz) \tag{B.1}$$

where z is a complex variable. From a physical perspective, the Faddeeva function naturally emerges whenever the system under consideration is governed by the convolution of a Gaussian and a Lorentzian distribution (i.e., a simple pole in the complex plane).

The real part of the Faddeeva function, up to normalization constants, constitutes the renowned *Voigt profile*. In classical spectroscopy, the Voigt distribution models the broadening of a spectral line due to the simultaneous combination of two independent mechanisms: thermal Doppler broadening (which produces a Gaussian profile) and natural or collisional broadening (which produces a Lorentzian profile).

In the context of this thesis, which focuses on Waveguide Quantum Electrodynamics (Waveguide QED), the Voigt profile and the Faddeeva function do not describe the thermal broadening of a classical atomic gas. Rather, they emerge deterministically from the quantum kinematics of a single scattering event.

Our system involves an incident single photon, which is not an ideal monochromatic wave but possesses a finite bandwidth described by a Gaussian spectral envelope (characterized by the standard deviation σ). The quantum emitter, acting as a two-level system, responds instead with a Lorentzian resonance curve, governed by its radiative decay rate γ and the frequency detuning Δ.

When computing the overlap integral between the photonic pulse and the tem-

poral response of the atom to obtain the macroscopic probabilities, we are effectively performing a convolution in the frequency domain between the Gaussian spectrum of the pulse and the Lorentzian susceptibility of the two-level emitter. It is for this precise structural reason that the complex scattering amplitude assumes the elegant analytical form of the Faddeeva function, and that the macroscopic routing probabilities faithfully follow a Voigt profile.

To rigorously interpret the dynamics of the Mach-Zehnder interferometer and the phase shift accumulated by the photon, it is imperative to establish a clear physical distinction between two fundamental quantities: the scattering amplitude $\mathcal{Z}$ and the macroscopic transmission amplitude $\mathcal{T}$.

- The Scattering Amplitude ($\mathcal{Z}$): This quantity is directly proportional to the Faddeeva function and describes *exclusively* the local response of the emitter. Its real part (the Voigt profile) quantifies the absorption and emission of the photon by the dipole, while its imaginary part quantifies the dispersion, namely the intrinsic phase shift introduced by the atomic polarizability.

- The Transmission Amplitude ($\mathcal{T}$): Defined by the interferometric relation $\mathcal{T} = 1 - \mathcal{Z}$, this quantity describes the global outcome of the propagation process within the waveguide arm housing the atom. Physically, it represents the coherent superposition between the unperturbed incident field and the forward-scattered field from the TLS, whose negative sign reflects the characteristic phase opposition of resonant emission.

The phase shift measurable at the interferometer detectors (Φ_{eff}) does not trivially coincide with the phase angle of the Faddeeva function, but is instead given by the argument of the entirely transmitted wave $\mathcal{T}$. In a regime of strong one-dimensional light-matter coupling, the intensity of the scattered field can equal or even exceed that of the unscattered incident field. At resonance, this dynamic causes the real part of $\mathcal{Z}$ to dominate over the coherent background, driving the transmission vector $\mathcal{T}$ into the complex half-plane with a negative real part. It is precisely this geometric transition, stemming from the destructive interference between 1 and $\mathcal{Z}$, that generates the highly non-linear phase jump and the topological phase winding of $\pm\pi$ observed in the numerical simulations of the device.

Appendix C

Energy Conservation and the Macroscopic Scattering Response

The exact mathematical relationship between the macroscopic routing probability $\mathcal{P}_d$ and the complex scattering response $\mathcal{Z}$ is fundamentally rooted in the conservation of probability. This connection, which represents a one-dimensional manifestation of the Optical Theorem, can be rigorously derived directly from the continuous-time equation of motion of the two-level system.

Let us consider the differential equation governing the probability amplitude of the excited state of the emitter in the waveguide:

$$\frac{d\psi_e(t)}{dt} = -\frac{\gamma}{2}\psi_e(t) + \sqrt{\gamma}\xi_{in}(t) \tag{C.1}$$

To evaluate the dynamic balance of the atomic population, we compute the time derivative of the excitation probability, $|\psi_e(t)|^2 = \psi_e^*(t)\psi_e(t)$:

$$\frac{d}{dt}|\psi_e(t)|^2 = \psi_e^*(t)\dot{\psi}_e(t) + \dot{\psi}_e^*(t)\psi_e(t) \tag{C.2}$$

Substituting the equation of motion into this expression yields:

$$\frac{d}{dt}|\psi_e(t)|^2 = -\gamma|\psi_e(t)|^2 + \sqrt{\gamma}\left(\psi_e^*(t)\xi_{in}(t) + \xi_{in}^*(t)\psi_e(t)\right) \tag{C.3}$$

Recognizing that the sum of a complex number and its conjugate equates to twice its real part, the population dynamics simplify to:

$$\frac{d}{dt}|\psi_e(t)|^2 = -\gamma|\psi_e(t)|^2 + 2\sqrt{\gamma}\mathrm{Re}\left[\xi_{in}^*(t)\psi_e(t)\right] \tag{C.4}$$

We now integrate this equation over the entire duration of the scattering event, from $t = -\infty$ to $t = +\infty$. Since the emitter is initially in its ground state prior to the arrival of the photon and must eventually decay back to it via spontaneous emission, the boundary conditions strictly enforce that $|\psi_e(\pm\infty)|^2 = 0$. Consequently, the

integral of the total derivative on the left-hand side vanishes exactly:

$$0 = -\gamma \int_{-\infty}^{+\infty} |\psi_e(t)|^2 dt + 2\sqrt{\gamma}\mathrm{Re}\left[\int_{-\infty}^{+\infty} \xi_{in}^*(t)\psi_e(t)dt\right] \tag{C.5}$$

Rearranging the terms, we establish a strict identity between the integrated atomic population and the coherent overlap integral:

$$\frac{\gamma}{2} \int_{-\infty}^{+\infty} |\psi_e(t)|^2 dt = \sqrt{\gamma}\mathrm{Re}\left[\int_{-\infty}^{+\infty} \xi_{in}^*(t)\psi_e(t)dt\right] \tag{C.6}$$

At this stage, we map these integral quantities to the macroscopic observables defined in the theoretical framework. The term on the left is exactly twice the integrated transmission-like routing probability, since, by definition, $\mathcal{P}_d = \frac{\gamma}{4}\int_{-\infty}^{+\infty} |\psi_e(t)|^2 dt$. The integral enclosed in the real part on the right side is precisely the definition of the macroscopic complex scattering response $\mathcal{Z}$.

Substituting these macroscopic definitions into the integral equality, we obtain the exact relation:

$$2\mathcal{P}_d = \mathrm{Re}[\mathcal{Z}] \tag{C.7}$$

Beyond its rigorous mathematical derivation, this factor of 2 embodies a profound physical interplay between the local dipole radiation dynamics and the global interferometric geometry. From the perspective of light-matter interaction, the term $2\mathrm{Re}[\mathcal{Z}]$ quantifies the total energy exchanged between the incident field and the two-level system. In both classical and quantum electrodynamics, the total power transferred to a dipole oscillator is strictly proportional to twice the real part of the overlap between the driving field and the induced polarization. Thus, the quantity $2\mathrm{Re}[\mathcal{Z}]$ physically represents the total integrated probability of the photon being scattered by the emitter.

However, this locally scattered light must navigate the macroscopic architecture of the MZI to be detected. Because the emitter is embedded in only one arm of the interferometer, the interaction occurs after the first 50:50 beam splitter and the scattered field subsequently pass through the final 50:50 beam splitter to reach the output ports. Each balanced beam splitter divides the field amplitude by a factor of $\sqrt{2}$. Consequently, the intensity of the scattered field reaching the transmission-like dark port (d) undergoes a geometric attenuation $(1/\sqrt{2})^4 = 1/4$ relative to the total intensity of the incoming single photon.

The integrated detection probability $\mathcal{P}_d$ therefore measures exactly one-quarter of the total scattered energy: $\mathcal{P}_d = \frac{1}{4} \times (2\mathrm{Re}[\mathcal{Z}]) = \frac{1}{2}\mathrm{Re}[\mathcal{Z}]$. The identity $\mathrm{Re}[\mathcal{Z}] = 2\mathcal{P}_d$ is thus not a mere mathematical artifact, but the necessary physical bridge reconciling the continuous-mode dipole scattering theory with the discrete, linear optical transformations of the MZI.

Appendix D

Analytical Derivation of the Critical Coupling Rate

In the framework of Waveguide Quantum Electrodynamics, a dynamical regime of particular physical interest is the perfect critical coupling. In this regime, the coherent forward-propagating field in the waveguide is completely extinguished due to perfect destructive interference with the secondary wave resonantly emitted by the quantum dot. In terms of the scattering formalism developed in Chapter 3, this condition corresponds to the vanishing of the single-arm transmission amplitude at zero detuning, $\mathcal{T}(\Delta = 0) = 1 - \mathcal{Z}(0) = 0$.

Recalling the fundamental interferometric relation $\mathcal{T} = 1 - \mathcal{Z}(\Delta)$, the critical coupling condition rigorously translates to imposing a unity macroscopic scattering response at exact resonance:

$$\mathcal{Z}(0) = 1. \tag{D.1}$$

To determine the specific atomic decay rate γ that satisfies this condition, we rely on the exact closed-form expression for the complex response derived previously:

$$\mathcal{Z}(\Delta) = 2\gamma\sigma\sqrt{\frac{\pi}{2}}W\left(\sqrt{2}\sigma\left(\Delta + i\frac{\gamma}{2}\right)\right). \tag{D.2}$$

Under strictly resonant conditions ($\Delta = 0$), the argument of the Faddeeva function, $W(z)$, becomes purely imaginary. Leveraging the mathematical identity $W(iy) = e^{y^2}\mathrm{erfc}(y)$ for $y \in \mathbb{R}$, the complex response elegantly loses its dispersive imaginary component, reducing to a strictly real function. By introducing the dimensionless parameter $x = \frac{\gamma\sigma}{\sqrt{2}}$, the critical coupling condition simplifies to the following transcendental equation:

$$2\sqrt{\pi}xe^{x^2}\mathrm{erfc}(x) = 1. \tag{D.3}$$

This relationship encapsulates the delicate energetic balance between the finite bandwidth of the incident Gaussian wavepacket (parameterized by σ) and the ra-

diative decay rate of the atomic transition (γ). Solving this transcendental equation numerically yields a single definitive positive root:

$$x \approx 0.435. \tag{D.4}$$

To extract the corresponding critical dimensionless coupling parameter, $\gamma_c \tau_g$, we express the standard deviation σ in terms of the intensity Full Width at Half Maximum (FWHM), τ_g. Utilizing the rigorous statistical relation $\sigma = \frac{\tau_g}{2\sqrt{2\ln 2}}$, and substituting this into the definition of x, we find:

$$x = \frac{\gamma \tau_g}{4\sqrt{\ln 2}}. \tag{D.5}$$

By isolating the dimensionless coupling parameter and substituting the numerical root for x, we obtain the exact condition required to achieve perfect coherent cancellation:

$$\gamma_c \tau_g = 4x\sqrt{\ln 2} \approx 1.45. \tag{D.6}$$

This analytically derived dimensionless value identifies the exact transition threshold between the undercoupled ($\gamma\tau_g < 1.45$) and overcoupled ($\gamma\tau_g > 1.45$) scattering regimes. It confirms that a dimensionless coupling parameter of $\gamma\tau_g \approx 1.45$ induces a discontinuous $\pm\pi$ phase jump in the transmitted field exactly at resonance. It should be noted that this condition characterises the single-arm scattering problem: in the full Mach–Zehnder interferometer, the detection probability at the dark port $P_d = \frac{1}{2}\mathrm{Re}[\mathcal{Z}]$ does not reach unity at critical coupling and continues to grow monotonically for $\gamma\tau_g > \gamma_c\tau_g$, as the scattering response $\mathcal{Z}(0)$ can exceed unity.

Appendix E

Comparison with the Numerical RK4 Solution

The numerical approach utilizing the time-bin formalism provides an exact and norm-preserving solution for the system's unitary evolution. To ensure the robustness and validity of this approach, it is essential to compare the results with a standard numerical technique for solving ordinary differential equations (ODEs), such as the Fourth-Order Runge-Kutta Method (RK4). The full Python code is presented as follows.

The RK4 method, often referred to as the classical Runge-Kutta method, is a highly effective iterative technique for approximating the solution to an Initial Value Problem (IVP) of a first-order ODE, typically expressed as $dy/dt = f(t, y(t))$ [Gur16; Kaw10].

In the context of the single-photon scattering problem, the time evolution of the emitter's excitation amplitude, $\psi_e(t)$, is governed by the first-order ODE of Eq. (2.23).

The RK4 method calculates the solution y_{n+1} at time $t_{n+1} = t_n + h$ (where h is the step size) based on the known value y_n at time t_n [Wan11]:

$$y_{n+1} = y_n + \frac{h}{6}(k_1 + 2k_2 + 2k_3 + k_4) \tag{E.1}$$

The core of the method involves calculating four estimated slopes, k_1, k_2, k_3, k_4, across the interval $[t_n, t_{n+1}]$, which are combined as a weighted average to achieve high accuracy [Kaw10; Was07]:

- k_1: Slope at the beginning of the interval (Euler's estimate):

$$k_1 = f(t_n, y_n)$$

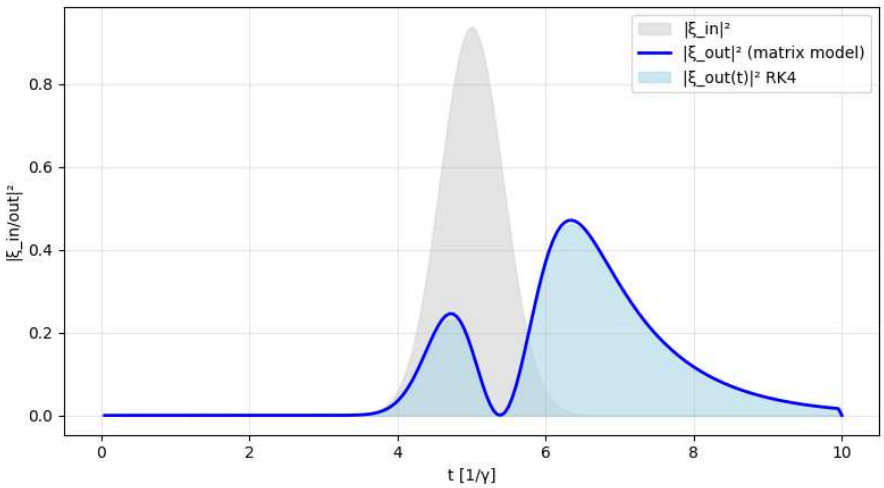

Figure E.1: Comparison of the output field intensity $|\xi_{\text{out}}(t)|^2$ derived from the matrix-based time-bin model (blue solid line) and the numerical RK4 solution of the continuous ODEs (light blue shaded area). The gray shaded area represents the normalized input Gaussian pulse $|\xi_{\text{in}}|^2$. The excellent overlap confirms the consistency between the two numerical frameworks.

- k_2: Slope at the midpoint, using the k_1 estimate:

$$k_2 = f\left(t_n + \frac{h}{2}, y_n + \frac{h}{2}k_1\right)$$

- k_3: Slope at the midpoint, refined using k_2:

$$k_3 = f\left(t_n + \frac{h}{2}, y_n + \frac{h}{2}k_2\right)$$

- k_4: Slope at the endpoint, using k_3:

$$k_4 = f(t_n + h, y_n + hk_3)$$

The RK4 method is preferred for its fourth-order accuracy, meaning the global truncation error is proportional to $\mathcal{O}(h^4)$. Once the numerical solution for $\psi_e(t)$ is obtained, the output wave-packet function $\xi_{out}(t)$ is determined via the input-output relation provided in Eq. (2.24). The RK4 algorithm was implemented in Python (details provided in Appendix B) using the same simulation parameters ($\gamma = 1.0$, $h = \Delta t = 0.05$) and Gaussian input pulse ($\xi(t)$) as the matrix time-bin model. Figure E.1 presents a comparative plot of the input and output field intensities, $|\xi_{\text{in}}|^2$ and $|\xi_{\text{out}}|^2$, obtained from the two distinct numerical methods.

The visual analysis of the output intensity $|\xi_{\text{out}}(t)|^2$ demonstrates an excellent quantitative agreement between the temporal profiles computed by the two methods:

the blue solid line, representing the result from the matrix time-bin model, perfectly overlaps with the light blue shaded area, representing the result from the RK4 solution, and the characteristic scattering pattern is accurately captured by both approaches, with a clear dip in intensity during the interaction time, followed by a delayed re-emission peak. This appendix provides also the complete Python source code used to generate the numerical RK4 solution, which served as the primary benchmark for cross-validating the matrix-based time-bin model.

Listing 1: Implementation of the RK4 method for the solution of the continuous ODE.

```
from __future__ import annotations
import numpy as np
import matplotlib.pyplot as plt
from typing import Callable, Tuple, Union
ArrayLike = Union[float, complex, np.ndarray]
def _as_array1d(y0: ArrayLike) -> np.ndarray:
    arr = np.asarray(y0)
    if arr.ndim == 0:
        arr = arr.reshape(1)
    if np.iscomplexobj(arr):
        return arr.astype(complex, copy=False)
    return arr.astype(float, copy=False)
def rk4_step(f: Callable[[float, np.ndarray], np.ndarray],
             t: float,
             y: np.ndarray,
             h: float) -> np.ndarray:
    k1 = f(t,           y)
    k2 = f(t + 0.5*h,   y + 0.5*h*k1)
    k3 = f(t + 0.5*h,   y + 0.5*h*k2)
    k4 = f(t + h,       y + h*k3)
    return y + (h/6.0)*(k1 + 2*k2 + 2*k3 + k4)
def rk4(f: Callable[[float, np.ndarray], np.ndarray],
        t_span: Tuple[float, float],
        y0: ArrayLike,
        h: float):
    t0, tf = t_span
    if h <= 0:
        raise ValueError("h must be > 0")
    if tf < t0:
        raise ValueError("tf must be >= t0")
```

```
    y = _as_array1d(y0)
    dim = y.size
    N = max(1, int(np.ceil((tf - t0)/h)))
    h = (tf - t0)/N
    t = np.linspace(t0, tf, N+1)
    Y = np.empty((N+1, dim), dtype=y.dtype)
    Y[0] = y
    ti = t0
    for n in range(N):
        y = rk4_step(f, ti, y, h)
        Y[n+1] = y
        ti = t[n+1]
    if dim == 1:
        return t, Y[:, 0]
    return t, Y
gamma, Delta = 1.0, 0.0
def xi(t, tauG=1.0, t0=5.0):
    return
     ↪  np.sqrt(2/tauG)*(np.log(2)/np.pi)**0.25*np.exp(-2*np.log(2)*(t-t0)**2/tauG*
def f_tls(t, psi_vec):
    psi = psi_vec[0]
    rhs = (-(gamma/2) - 1j*Delta)*psi + np.sqrt(gamma)*xi(t)
    return np.array([rhs], dtype=complex)
t_tls, psi = rk4(f_tls, (0.0, 10.0), y0=0.0+0.0j, h=5e-3)
xi_in = xi(t_tls)
xi_out_rk4 = xi_in - np.sqrt(gamma) * psi
```

Appendix F

Python Code for the time-bins Numerical Simulation

The complete Python implementation of the matrix-based time-bin model is reported below.

Listing 2: Time-bin simulation code.

```
import numpy as np
from scipy.special import wofz, erf
from scipy.sparse import csr_matrix, lil_matrix, bmat, identity,
↪  diags
from scipy.sparse.linalg import expm_multiply
import datetime
# ================================================================
# PARAMETERS: TLS (Two-Level System)
# ================================================================
# Spontaneous emission rates to explore (main scan)
tls_gamma_values = [0.5, 1.0, 1.45, 1.9, 3.0]
# Fine gamma range for the dense scan around the critical coupling
tls_gamma_focus  = np.round(np.arange(1.40, 1.51, 0.01), 2)
# Atom-field detuning sweep
tls_delta_values          = np.arange(-10.0, 10.0, 0.1)
tls_delta_focus           = np.round(np.arange(-0.10, 0.11, 0.01), 2)
tls_delta_snapshot_values = [0.0, 1.0, 2.0, 3.5, 5.0]
# Gaussian wavepacket
tls_sigma = 0.425
tls_t0    = 5.0
# Time grid
tls_tmax  = 15.0
```

```
tls_dt    = 0.005
tls_times = np.arange(0, tls_tmax + tls_dt, tls_dt)
tls_N     = len(tls_times)
tls_dim_w = tls_N + 1       # N time-bins + 1 atomic degree of freedom
if tls_dt > tls_sigma:
    raise ValueError(f"tls_dt={tls_dt} > tls_sigma={tls_sigma}: time step too coarse")
if tls_tmax < tls_t0:
    raise ValueError(f"tls_tmax={tls_tmax} < tls_t0={tls_t0}: grid does not cover the pulse")
# ================================================================
# PARAMETERS: JC (Jaynes-Cummings + cavity)
# ================================================================
# Cavity-waveguide coupling rate (cavity linewidth, HWHM), units of kappa
jc_kappa = 1.0
# Vacuum Rabi coupling strengths (main scan)
#   g = 0.1 kappa : weak coupling (Purcell regime)
#   g = 1.0 kappa : onset of strong coupling
#   g = 5.0 kappa : deep strong coupling
jc_g_values     = [0.0, 0.1, 1.0, 5.0]
jc_g_values_pop = sorted(set(jc_g_values + [0.5, 1.5]))   # denser set for the internal-populations run at Delta = 0
# Photon-cavity detuning sweep (delta = omega_p - omega_c)
jc_delta_values          = np.round(np.arange(-8.0,  8.01,  0.05), 5)
jc_delta_focus           = np.round(np.arange(-0.5,  0.501, 0.01), 5)
jc_delta_snapshot_values = [0.0, 0.1, 1.0, 5.0]
# Gaussian wavepacket - sigma chosen so that spectral FWHM = kappa:
#   FWHM_omega = sqrt(2 ln 2) / sigma = kappa  =>  sigma = sqrt(2 ln 2) * 5
jc_sigma = 5 * np.sqrt(2 * np.log(2))
jc_t0    = 30
# Time grid
jc_tmax  = 80
jc_dt    = 0.02
jc_times = np.arange(0, jc_tmax + jc_dt, jc_dt)
jc_N     = len(jc_times)
if jc_dt > jc_sigma:
```

```
55      raise ValueError(f"jc_dt={jc_dt} > jc_sigma={jc_sigma}: time
        ↪ step too coarse")
56  if jc_tmax < jc_t0:
57      raise ValueError(f"jc_tmax={jc_tmax} < jc_t0={jc_t0}: grid does
        ↪ not cover the pulse")
58  # ================================================================
59  # COMMON UTILITY FUNCTIONS
60  # ================================================================
61  def pulse_shape(t, sigma, t0):
62      """Gaussian probability amplitude, normalised so that int
        ↪ |pulse|^2 dt = 1."""
63      norm = (1.0 / sigma) ** 0.5 * (1.0 / (2.0 * np.pi)) ** 0.25
64      return norm * np.exp(-(t - t0) ** 2 / (4.0 * sigma ** 2))
65  # --- Beam-splitter ladder operators (shared by both simulations)
    ↪ ---
66  # Field vector layout (dim = 1 + 2N):
67  #   psi_field[0]       : vacuum
68  #   psi_field[1:N+1]   : wg_a[k], k=0..N-1  (upper arm)
69  #   psi_field[N+1:2N+1]: wg_b[k], k=0..N-1  (lower arm)
70  def _w_bin_a(k, N):
71      dim = 1 + 2 * N
72      return csr_matrix(([1.0], ([0], [k + 1])), shape=(dim, dim),
        ↪ dtype=complex)
73  def _wd_bin_a(k, N):
74      dim = 1 + 2 * N
75      return csr_matrix(([1.0], ([k + 1], [0])), shape=(dim, dim),
        ↪ dtype=complex)
76  def _w_bin_b(k, N):
77      dim = 1 + 2 * N
78      return csr_matrix(([1.0], ([0], [N + k + 1])), shape=(dim, dim),
        ↪ dtype=complex)
79  def _wd_bin_b(k, N):
80      dim = 1 + 2 * N
81      return csr_matrix(([1.0], ([N + k + 1], [0])), shape=(dim, dim),
        ↪ dtype=complex)
82  def construct_H_n_bs(n, N, dt):
83      """
84      50:50 beam-splitter Hamiltonian (Hadamard convention) for
        ↪ time-bin n.
85      H = i*(pi/4/dt) * (wd_b w_a - wd_a w_b)
```

```
    => exp(-i H dt) = (1/sqrt(2)) [[1,-1],[1,1]]
    """
    V = np.pi / 4
    w_a  = _w_bin_a(n, N);  wd_a = _wd_bin_a(n, N)
    w_b  = _w_bin_b(n, N);  wd_b = _wd_bin_b(n, N)
    return 1j * (V / dt) * (wd_b @ w_a - wd_a @ w_b)
def build_initial_field_state(pulse_in, N, dt):
    """
    Initial field vector for the full time-bin MZI formalism.
    psi_field[n+1] = sqrt(dt) * pulse_in[n+1] for n = 0..N-2 (wg_a
    ↪  = input, wg_b = vacuum).
    """
    psi = np.zeros(1 + 2 * N, dtype=complex)
    psi[1:N] = np.sqrt(dt) * pulse_in[1:N]
    return psi
# ================================================================
# TLS HAMILTONIAN
# ================================================================
def construct_H_n(n, gamma, delta, N, dt):
    """
    Sparse TLS Hamiltonian in the full time-bin formalism at step
    ↪  n.
    Acts on psi_tls of dimension 2*(N+1):
      psi_tls[0:N+1]      : ground sector  (field in wg_a)
      psi_tls[N+1:2*(N+1)]: excited sector (field in wg_a)
    Block structure:
      H = [[    0,         -pref * wd_n ],
           [ pref * w_n,    delta * I   ]]
    with pref = i * sqrt(gamma / dt).
    """
    dim_w = N + 1
    pref  = 1j * np.sqrt(gamma / dt)
    w_n = lil_matrix((dim_w, dim_w), dtype=complex)
    if n + 1 < dim_w:
        w_n[0, n + 1] = 1.0
    w_n  = w_n.tocsr()
    wd_n = w_n.conj().T.tocsr()
    H_gg = csr_matrix((dim_w, dim_w), dtype=complex)
    H_ee = delta * identity(dim_w, dtype=complex, format='csr')
    return bmat([[H_gg, -pref * wd_n],
```

```
                [pref * w_n, H_ee]], format='csr')
# ================================================================
# JAYNES-CUMMINGS HAMILTONIAN
# ================================================================
def construct_H_n_jc(n, kappa, g, delta, N, dt):
    """
    Sparse Jaynes-Cummings Hamiltonian in the full time-bin formalism at step n.
    Acts on psi_sys of dimension N+2:
      psi_sys[0:N]  : waveguide time-bins
      psi_sys[N]    : cavity mode
      psi_sys[N+1]  : atom  (kept on resonance with cavity: omega_c = omega_0)
    Non-zero off-diagonal couplings:
      wg bin n <-> cavity : coupling sqrt(kappa/dt)
      cavity   <-> atom   : vacuum Rabi coupling g
    Diagonal: delta = omega_p - omega_c on both cavity and atom.
    """
    dim  = N + 2
    pref = 1j * np.sqrt(kappa / dt)
    rows = [n,     N,    N,    N + 1]
    cols = [N,     n,    N+1,  N    ]
    data = [-pref, pref, g,    g    ]
    H = csr_matrix((data, (rows, cols)), shape=(dim, dim), dtype=complex)
    diag_vals        = np.zeros(dim, dtype=complex)
    diag_vals[N]     = delta
    diag_vals[N + 1] = delta
    return H + diags(diag_vals, format='csr')
# ================================================================
# ANALYTIC SCATTERING FUNCTIONS (TLS, Faddeeva)
# ================================================================
def calculate_analytic_scattering(delta_values, gamma, sigma):
    """
    Transmission (P_trans), reflection (P_refl), and phase shift for a TLS
    in a waveguide, for a Gaussian wavepacket of width sigma (Faddeeva function).
    """
```

```
158     z         = np.sqrt(2) * sigma * (-delta_values + 1j * (gamma /
        ↪ 2))
159     prefactor = gamma * sigma * np.sqrt(np.pi / 2)
160     Z         = prefactor * wofz(z)
161     P_refl    = np.real(Z)
162     P_trans   = 1.0 - P_refl
163     phase     = np.angle(1.0 - 2.0 * Z)
164     return P_trans, P_refl, phase
165 def calculate_analytic_complex_amplitudes(delta_values, gamma,
    ↪ sigma):
166     """
167     Complex transmission amplitude T and scattering response Z for
        ↪ a TLS,
168     for a Gaussian wavepacket of width sigma.  Returns (T, Z) with
        ↪ T = 1 - Z.
169     """
170     z         = np.sqrt(2) * sigma * (-delta_values + 1j * (gamma /
        ↪ 2))
171     prefactor = 2 * gamma * sigma * np.sqrt(np.pi / 2)
172     Z         = prefactor * wofz(z)
173     return 1.0 - Z, Z
174 def calculate_psi_out_analytic(pulse_vals, gamma, delta, sigma, t0,
    ↪ times_plot):
175     """
176     Closed-form output wavefunction psi_out(t) for a TLS in a
        ↪ waveguide.
177     With lambda = gamma/2 + i*delta and mu_eff = t0 +
        ↪ 2*sigma^2*lambda:
178       c_e(t) = sqrt(gamma) * (pi*sigma^2/2)^{1/4}
179                * exp[-lambda*(t-t0) + lambda^2*sigma^2]
180                * [erf((t - mu_eff)/(2*sigma)) -
                   ↪ erf(-mu_eff/(2*sigma))]
181       psi_out(t) = pulse_in(t) - sqrt(gamma) * c_e(t)
182     """
183     lam      = gamma / 2 + 1j * delta
184     mu_eff   = t0 + 2 * sigma**2 * lam
185     pref     = np.sqrt(gamma) * (np.pi * sigma**2 / 2)**0.25
186     exp_term = np.exp(-lam * (times_plot - t0) + lam**2 * sigma**2)
187     erf_term = erf((times_plot - mu_eff) / (2 * sigma)) - erf(-mu_eff
        ↪ / (2 * sigma))
```

```
188     c_e      = pref * exp_term * erf_term
189     return pulse_vals[:-1] - np.sqrt(gamma) * c_e
190 # ================================================================
191 # TLS SIMULATION
192 # ================================================================
193 # --- Input field ---
194 tls_pulse_in  = pulse_shape(tls_times, tls_sigma, tls_t0)
195 tls_pulse_in /= np.sqrt(np.sum(np.abs(tls_pulse_in)**2) * tls_dt)
196 tls_psi_field_init = build_initial_field_state(tls_pulse_in, tls_N,
    ↪ tls_dt)
197 def run_one_tls(gamma, delta):
198     """Run one full time-bin MZI simulation for a TLS at the given
      ↪ (gamma, delta).
199     Returns a dict with integrated probabilities and selected
      ↪ time-domain fields."""
200     psi_field        = tls_psi_field_init.copy()
201     psi_tls          = np.zeros(2 * tls_dim_w, dtype=complex)
202     upper_arm_out    = np.zeros(tls_N, dtype=complex)
203     port_refl_field  = np.zeros(tls_N, dtype=complex)
204     port_trans_field = np.zeros(tls_N, dtype=complex)
205     for n in range(tls_N - 1):
206         # BS1
207         H_n_bs    = construct_H_n_bs(n, tls_N, tls_dt)
208         psi_field = expm_multiply(-1j * H_n_bs * tls_dt, psi_field)
209         # TLS interaction
210         psi_tls[n + 1]       = psi_field[n + 1]
211         H_n                  = construct_H_n(n, gamma, delta, tls_N,
            ↪ tls_dt)
212         psi_tls              = expm_multiply(-1j * H_n * tls_dt,
            ↪ psi_tls)
213         psi_field[n + 1]     = psi_tls[n + 1]
214         upper_arm_out[n + 1] = psi_tls[n + 1] / np.sqrt(tls_dt)
215         # BS2
216         psi_field = expm_multiply(-1j * H_n_bs * tls_dt, psi_field)
217         port_refl_field[n + 1]  = psi_field[n + 1]         /
            ↪ np.sqrt(tls_dt)
218         port_trans_field[n + 1] = psi_field[tls_N + n + 1] /
            ↪ np.sqrt(tls_dt)
219     P_trans = np.sum(np.abs(port_trans_field[:-1])**2) * tls_dt
220     P_refl  = np.sum(np.abs(port_refl_field[:-1])**2)  * tls_dt
```

```
    xi_out      = upper_arm_out * np.sqrt(2)
    overlap_out = np.sum(np.conj(tls_pulse_in) * xi_out) * tls_dt
    overlap_in  = np.sum(np.abs(tls_pulse_in)**2)        * tls_dt
    transm      = overlap_out / overlap_in if np.abs(overlap_in) > 1e-15 else 0.0 + 0j
    return {
        'P_trans': P_trans,
        'P_refl':  P_refl,
        'transm':  transm,
        'xi_out':  xi_out,
    }
# --- Simulation loop ---
_t0_tls = datetime.datetime.now()
print(f"TLS simulation started  [{_t0_tls.strftime('%H:%M:%S')}]")
tls_all_deltas = np.sort(np.unique(np.concatenate((tls_delta_values, tls_delta_focus))))
tls_all_gammas = np.sort(np.unique(np.concatenate((tls_gamma_values, tls_gamma_focus))))
n_tls_gamma    = len(tls_all_gammas)
n_tls_delta    = len(tls_all_deltas)
tls_results_by_gamma = {}
for g_idx, current_gamma in enumerate(tls_all_gammas, 1):
    print(f"\n[{g_idx}/{n_tls_gamma}] gamma = {current_gamma} ({n_tls_delta} delta points)")
    trans_list     = []
    refl_list      = []
    phase_list     = []
    transm_list    = []
    gaussian_plots = {}
    milestones = {int(n_tls_delta * f) for f in (0.25, 0.50, 0.75, 1.0)}
    for d_idx, current_delta in enumerate(tls_all_deltas, 1):
        if d_idx in milestones:
            print(f"  delta {d_idx}/{n_tls_delta} ({100*d_idx//n_tls_delta}%)")
        out = run_one_tls(current_gamma, current_delta)
        trans_list.append(out['P_trans'])
        refl_list.append(out['P_refl'])
        phase_list.append(np.angle(out['transm']))
        transm_list.append(out['transm'])
```

```
255         for d_snap in tls_delta_snapshot_values:
256             if np.isclose(current_delta, d_snap, atol=1e-5):
257                 gaussian_plots[d_snap] =
                    ↪ np.abs(out['xi_out'][:-1])**2
258                 break
259     tls_results_by_gamma[current_gamma] = {
260         'trans_final':    np.array(trans_list),
261         'refl_final':     np.array(refl_list),
262         'phase_numeric':  np.array(phase_list),
263         'transm_complex': np.array(transm_list),
264         'gaussian_plots': gaussian_plots,
265     }
266 _t1_tls = datetime.datetime.now()
267 print(f"\nTLS simulation complete  (elapsed: {str(_t1_tls -
    ↪ _t0_tls).split('.')[0]})")
268 # ================================================================
269 # JAYNES-CUMMINGS SIMULATION
270 # ================================================================
271 # --- Input field ---
272 jc_pulse_in  = pulse_shape(jc_times, jc_sigma, jc_t0)
273 jc_pulse_in /= np.sqrt(np.sum(np.abs(jc_pulse_in)**2) * jc_dt)
274 jc_psi_field_init = build_initial_field_state(jc_pulse_in, jc_N,
    ↪ jc_dt)
275 def run_one_jc(g, delta):
276     """Run one full time-bin MZI simulation for the JC system at
        ↪ the given (g, delta).
277     Returns a dict with integrated probabilities, internal
        ↪ populations, and
278     the complex transmission amplitude."""
279     psi_field = jc_psi_field_init.copy()
280     psi_sys   = np.zeros(jc_N + 2, dtype=complex)
281     upper_arm_out    = np.zeros(jc_N, dtype=complex)
282     port_refl_field  = np.zeros(jc_N, dtype=complex)
283     port_trans_field = np.zeros(jc_N, dtype=complex)
284     cav_amp          = np.zeros(jc_N, dtype=complex)
285     atom_amp         = np.zeros(jc_N, dtype=complex)
286     for n in range(jc_N - 1):
287         # BS1
288         H_n_bs    = construct_H_n_bs(n, jc_N, jc_dt)
289         psi_field = expm_multiply(-1j * H_n_bs * jc_dt, psi_field)
```

```
290             psi_sys[n] = psi_field[n + 1]
291             # Jaynes-Cummings evolution
292             H_n_jc  = construct_H_n_jc(n, jc_kappa, g, delta, jc_N,
                ↪  jc_dt)
293             psi_sys = expm_multiply(-1j * H_n_jc * jc_dt, psi_sys)
294             psi_field[n + 1]     = psi_sys[n]
295             upper_arm_out[n + 1] = psi_sys[n]        / np.sqrt(jc_dt)
296             cav_amp[n + 1]       = psi_sys[jc_N]
297             atom_amp[n + 1]      = psi_sys[jc_N + 1]
298             # BS2
299             psi_field = expm_multiply(-1j * H_n_bs * jc_dt, psi_field)
300             port_refl_field[n + 1]  = psi_field[n + 1]        /
                ↪  np.sqrt(jc_dt)
301             port_trans_field[n + 1] = psi_field[jc_N + n + 1] /
                ↪  np.sqrt(jc_dt)
302         P_trans = np.sum(np.abs(port_trans_field[:-1])**2) * jc_dt
303         P_refl  = np.sum(np.abs(port_refl_field[:-1])**2)  * jc_dt
304         xi_out      = upper_arm_out * np.sqrt(2)
305         overlap_out = np.sum(np.conj(jc_pulse_in) * xi_out) * jc_dt
306         overlap_in  = np.sum(np.abs(jc_pulse_in)**2)        * jc_dt
307         transm      = overlap_out / overlap_in if np.abs(overlap_in) >
            ↪  1e-15 else 0.0 + 0j
308         return {
309             'P_trans':  P_trans,
310             'P_refl':   P_refl,
311             'transm':   transm,
312             'xi_out':   xi_out,
313             'cav_amp':  cav_amp,
314             'atom_amp': atom_amp,
315         }
316     # --- Main simulation loop (full delta sweep for each g) ---
317     _t0_jc = datetime.datetime.now()
318     print(f"\nJC simulation started  [{_t0_jc.strftime('%H:%M:%S')}]")
319     jc_all_deltas = np.sort(np.unique(np.concatenate((jc_delta_values,
        ↪  jc_delta_focus))))
320     n_jc_delta    = len(jc_all_deltas)
321     n_jc_g        = len(jc_g_values)
322     jc_results_by_g = {}
323     for g_idx, current_g in enumerate(jc_g_values, 1):
```

```
    print(f"\n[{g_idx}/{n_jc_g}] g = {current_g}  ({n_jc_delta} delta points)")
    trans_list     = []
    refl_list      = []
    phase_list     = []
    transm_list    = []
    cav_pop_plots  = {}
    atom_pop_plots = {}
    milestones = {int(n_jc_delta * f) for f in (0.25, 0.50, 0.75, 1.0)}
    for d_idx, current_delta in enumerate(jc_all_deltas, 1):
        if d_idx in milestones:
            print(f"  delta {d_idx}/{n_jc_delta}  ({100*d_idx//n_jc_delta}%)")
        out = run_one_jc(current_g, current_delta)
        trans_list.append(out['P_trans'])
        refl_list.append(out['P_refl'])
        phase_list.append(np.angle(out['transm']))
        transm_list.append(out['transm'])
        for dc_snap in jc_delta_snapshot_values:
            if np.isclose(current_delta, dc_snap, atol=1e-5):
                cav_pop_plots[dc_snap]  = np.abs(out['cav_amp'][:-1])**2
                atom_pop_plots[dc_snap] = np.abs(out['atom_amp'][:-1])**2
                break
    jc_results_by_g[current_g] = {
        'trans_final':    np.array(trans_list),
        'refl_final':     np.array(refl_list),
        'phase_numeric':  np.array(phase_list),
        'transm_complex': np.array(transm_list),
        'cav_pop_plots':  cav_pop_plots,
        'atom_pop_plots': atom_pop_plots,
    }
# --- Extra run: internal populations at Delta = 0 for the denser g sweep ---
print("\nExtra JC runs at Delta = 0 (internal populations):")
jc_populations_at_zero = {}
for g_pop in jc_g_values_pop:
    stored = jc_results_by_g.get(g_pop, {})
```

```
    if 0.0 in stored.get('cav_pop_plots', {}):
        jc_populations_at_zero[g_pop] = {
            'cav':  stored['cav_pop_plots'][0.0],
            'atom': stored['atom_pop_plots'][0.0],
        }
        continue
    print(f"  extra: g = {g_pop}")
    out = run_one_jc(g_pop, 0.0)
    jc_populations_at_zero[g_pop] = {
        'cav':  np.abs(out['cav_amp'][:-1])**2,
        'atom': np.abs(out['atom_amp'][:-1])**2,
    }
_t1_jc = datetime.datetime.now()
print(f"\nJC simulation complete  (elapsed: {str(_t1_jc - _t0_jc).split('.')[0]})")
```

Appendix G

Single-photon scattering on a polariton resonance: reduction to an effective two-level emitter

The polariton diagonalization presented in Sect. 2.5.1 provides the spectral structure of the cavity-coupled qubit within the single-excitation subspace. However, it does not directly yield the time-domain scattering response. This appendix bridges the two frameworks. It demonstrates that, on a single-polariton resonance, the input-output relation of the JC system reduces to a form structurally identical to the bare-emitter case of Chapter 3. In this regime, the polariton acts as the effective two-level emitter. This effective description provides a quantitative interpretation of the double-peaked wavepackets observed at $\Delta = \pm g$ in Sect. 4.5.

Assume a Gaussian wavepacket of central frequency ω_p and spectral FWHM $\Delta\omega_{\text{pulse}}$ incident on the cavity-coupled qubit. The two polariton resonances of Eq. (2.29) are located at $\omega_R \pm g$, separated by $2g$. When the pulse is tuned to the upper polariton, $\omega_p = \omega_R + g$ ($\Delta = +g$), its spectral support overlaps the resonance at $+g$ but remains at a distance of $2g$ from the resonance at $-g$. Provided that $2g \gtrsim \Delta\omega_{\text{pulse}}$, the lower polariton remains unpopulated and $c_-(t) \approx 0$. Similarly, for $\Delta = -g$ only the lower polariton is excited and $c_+(t) \approx 0$. The transmission spectrum derived by Shen and Fan [SF09] for the same cavity-coupled architecture confirms this behavior. It shows that the two polaritonic dips at $\omega = \omega_c \pm g$ are spectrally resolved whenever the splitting $2g$ exceeds the dip FWHM κ.

In this regime, the basis decomposition of Eq. (2.33) simplifies to $a(t) = c_+(t)/\sqrt{2}$. Substituting this into Eq. (2.30) yields

$$\xi_{\text{out}}(t) = \xi_{\text{in}}(t) - \sqrt{\kappa/2}\, c_+(t). \tag{G.1}$$

This result is structurally identical to the input-output relation of the bare two-

level emitter analyzed in Chapter 3, i.e., Eq. (2.24), with the substitutions $\sqrt{\Gamma} \to \sqrt{\kappa/2}$ and $\psi_e(t) \to c_+(t)$. The polariton amplitude $c_+(t)$ takes the role of the bare-emitter excitation amplitude. The cavity-coupled qubit responds to the input field as an effective two-level system with a coupling rate of $\sqrt{\kappa/2}$ to the waveguide. An analogous result holds at $\Delta = -g$ with $c_+(t)$ replaced by $c_-(t)$.

The effective coupling rate $\sqrt{\kappa/2}$ in Eq. (G.1) corresponds to an effective decay rate $\Gamma_{\text{eff}} = \kappa/2$ of the polariton into the waveguide. This result derives from two independent arguments. The first follows directly from the hybrid composition of the polariton. The state $|\pm\rangle$ is 50% cavity-excited and 50% qubit-excited. Since only the cavity component couples to the waveguide with rate κ, the Fermi golden rule predicts an effective decay rate $\Gamma_{\text{eff}} = |\langle 1_c, g|+\rangle|^2 \, \kappa = \kappa/2$. The second argument relies on the exact solution of the dissipative Jaynes–Cummings dynamics in the strong coupling regime. This dynamics exhibits Rabi oscillations damped at the rate $(\gamma_{ng} + \kappa)/2$ between the cavity and the qubit [LMS15], where γ_{ng} explicitly represents the rate of spontaneous emission into nonguided radiation modes (i.e., out of the cavity). For $\gamma_{ng} = 0$, as ideally assumed in this setup, this overall damping rate simply reduces to $\kappa/2$, perfectly matching the half-cavity argument derived above. The same result emerges from the stationary spectral analysis of Shen and Fan [SF09]. The FWHM of each transmission dip at $\omega = \omega_c \pm g$ is exactly κ, which corresponds to a polariton amplitude decay rate of $\kappa/2$.

Consequently, on a single-polariton resonance, the cavity-coupled qubit responds as an effective two-level emitter. Three parameters define this reduction. First, the spectral position shifts from the bare qubit transition to the polariton frequency $\omega_R \pm g$. Second, the decay rate into the waveguide is halved from κ to $\Gamma_{\text{eff}} = \kappa/2$. Third, the dynamical variable is the polariton amplitude $c_\pm(t)$ rather than the bare emitter amplitude $\psi_e(t)$. Under this mapping, the entire phenomenology of the bare-emitter scattering detailed in Sect. 4.3 — including destructive interference between the input and re-emitted field, the exponential tail, and the group delay — translates directly to the JC case at $\Delta = \pm g$. The double-peaked wavepackets observed in Fig. 4.5 of Sect. 4.5 are a direct manifestation of this effective two-level dynamics. Because $\Gamma_{\text{eff}} = \kappa/2$ depends solely on κ, the temporal shape of the scattered field on a polariton resonance is invariant with respect to g. This is strictly in agreement with the near superposition of the panels at $(g, \Delta) = (\kappa, \kappa)$ and $(5\kappa, 5\kappa)$.

Bibliography

[AS64] Milton Abramowitz and Irene A. Stegun. *Handbook of Mathematical Functions with Formulas, Graphs, and Mathematical Tables*. Applied Mathematics Series 55. Washington, D.C.: National Bureau of Standards, 1964.

[GC85] C. W. Gardiner and M. J. Collett. "Input and output in damped quantum systems: Quantum stochastic differential equations and the master equation". In: *Phys. Rev. A* 31 (6 June 1985), pp. 3761–3774. DOI: 10.1103/PhysRevA.31.3761. URL: https://link.aps.org/doi/10.1103/PhysRevA.31.3761.

[GPZ92] C. W. Gardiner, A. S. Parkins, and P. Zoller. "Wave-function quantum stochastic differential equations and quantum-jump simulation methods". In: *Phys. Rev. A* 46 (7 Oct. 1992), pp. 4363–4381. DOI: 10.1103/PhysRevA.46.4363. URL: https://link.aps.org/doi/10.1103/PhysRevA.46.4363.

[SZ97] Marlan O. Scully and M. Suhail Zubairy. *Quantum Optics*. Cambridge: Cambridge University Press, 1997. ISBN: 978-0-521-43595-6. DOI: 10.1017/CBO9780511813993.

[ZG97] P. Zoller and C. W. Gardiner. "Quantum Noise in Quantum Optics: the Stochastic Schrödinger Equation". In: *arXiv e-prints* quant-ph/9702030 (Feb. 1997). DOI: 10.48550/arXiv.quant-ph/9702030. URL: https://arxiv.org/abs/quant-ph/9702030.

[DNR98] S. Dürr, T. Nonn, and G. Rempe. "Origin of quantum-mechanical complementarity probed by a 'which-way' experiment in an atom interferometer". In: *Nature* 395.6697 (1998), pp. 33–37. DOI: 10.1038/25653. URL: https://doi.org/10.1038/25653.

[Lou00] Rodney Loudon. *The Quantum Theory of Light*. 3rd. Oxford: Oxford University Press, 2000.

[Sch+07] D. I. Schuster, A. A. Houck, J. A. Schreier, A. Wallraff, J. M. Gambetta, A. Blais, L. Frunzio, J. Majer, B. Johnson, M. H. Devoret, S. M. Girvin, and R. J. Schoelkopf. "Resolving photon number states in a superconducting circuit". In: *Nature* 445.7127 (2007), pp. 515–518. ISSN: 1476-4687. DOI: 10.1038/nature05461. URL: https://doi.org/10.1038/nature05461.

[Was07] Dr. Brian R. Washburn. "Runge-Kutta 4th order method solving ordinary differenital equations differential equations". MA thesis. Kansas State University (KSU), 2007. URL: https://www.phys.ksu.edu/personal/washburn/Teaching/Class%20Files/NQO/Tutorials/Tutorial4_RungeKutta4thOrder.pdf.

[Jac+08] Vincent Jacques, E Wu, Frédéric Grosshans, Fran çois Treussart, Philippe Grangier, Alain Aspect, and Jean-Fran çois Roch. "Delayed-Choice Test of Quantum Complementarity with Interfering Single Photons". In: *Phys. Rev. Lett.* 100 (22 June 2008), p. 220402. DOI: 10.1103/PhysRevLett.100.220402. URL: https://link.aps.org/doi/10.1103/PhysRevLett.100.220402.

[SF09] Jung-Tsung Shen and Shanhui Fan. "Theory of single-photon transport in a single-mode waveguide. I. Coupling to a cavity containing a two-level atom". In: *Phys. Rev. A* 79 (2 Feb. 2009), p. 023837. DOI: 10.1103/PhysRevA.79.023837. URL: https://link.aps.org/doi/10.1103/PhysRevA.79.023837.

[GAF10] Gilbert Grynberg, Alain Aspect, and Claude Fabre. *Introduction to Quantum Optics: From the Photon to Quantum Technologies*. Cambridge: Cambridge University Press, 2010. ISBN: 978-0-521-76032-4. DOI: 10.1017/CBO9780511778261.

[Kaw10] Autar Kaw. "Runge-Kutta 4th order method". MA thesis. University of South Florida, 2010. URL: https://nm.mathforcollege.com/mws/gen/08ode/mws_gen_ode_txt_runge4th.pdf.

[Che+11] Yuntian Chen, Martijn Wubs, Jesper Mørk, and A Femius Koenderink. "Coherent single-photon absorption by single emitters coupled to one-dimensional nanophotonic waveguides". In: *New Journal of Physics* 13.10 (Oct. 2011), p. 103010. DOI: 10.1088/1367-2630/13/10/103010. URL: https://doi.org/10.1088/1367-2630/13/10/103010.

[Wan11] Yanqiu Wang. "Runge-Kutta method". MA thesis. Oklahoma State University (OSU), 2011. URL: https://math.okstate.edu/people/yqwang/teaching/math4513_fall11/Notes/rungekutta.pdf.

[Bar+12] Ben Q. Baragiola, Robert L. Cook, Agata M. Brańczyk, and Joshua Combes. "N-photon wave packets interacting with an arbitrary quantum system". In: *Phys. Rev. A* 86 (1 July 2012), p. 013811. DOI: 10.1103/PhysRevA.86.013811. URL: https://link.aps.org/doi/10.1103/PhysRevA.86.013811.

[CVL14] Darrick E. Chang, Vladan Vuletić, and Mikhail D. Lukin. "Quantum nonlinear optics — photon by photon". In: *Nature Photonics* 8.9 (2014), pp. 685–694. DOI: 10.1038/nphoton.2014.192. URL: https://doi.org/10.1038/nphoton.2014.192.

[Har+14] Nicholas C. Harris, Yangjin Ma, Jacob Mower, Tom Baehr-Jones, Dirk Englund, Michael Hochberg, and Christophe Galland. "Efficient, compact and low loss thermo-optic phase shifter in silicon". In: *Opt. Express* 22.9 (May 2014), pp. 10487–10493.

[Sho+14] Itay Shomroni, Serge Rosenblum, Yulia Lovsky, Orel Bechler, Gabriel Guendelman, and Barak Dayan. "All-optical routing of single photons by a one-atom switch controlled by a single photon". In: *Science* 345.6199 (2014), pp. 903–906. DOI: 10.1126/science.1254699. URL: https://doi.org/10.1126/science.1254699.

[Wan+14] Jianwei Wang, Alberto Santamato, Pisu Jiang, Damien Bonneau, Erman Engin, Joshua W. Silverstone, Matthias Lermer, Johannes Beetz, Martin Kamp, Sven Höfling, Michael G. Tanner, Chandra M. Natarajan, Robert H. Hadfield, Sander N. Dorenbos, Val Zwiller, Jeremy L. O'Brien, and Mark G. Thompson. "Gallium arsenide (GaAs) quantum photonic waveguide circuits". In: *Optics Communications* 327 (2014). Special Issue on Nonlinear Quantum Photonics, pp. 49–55. ISSN: 0030-4018. DOI: https://doi.org/10.1016/j.optcom.2014.02.040. URL: https://www.sciencedirect.com/science/article/pii/S0030401814001874.

[LMS15] Peter Lodahl, Sahand Mahmoodian, and Søren Stobbe. "Interfacing single photons and single quantum dots with photonic nanostructures". In: *Rev. Mod. Phys.* 87 (2 May 2015), pp. 347–400. DOI: 10.1103/RevModPhys.87.347. URL: https://link.aps.org/doi/10.1103/RevModPhys.87.347.

[Gur16] Dr. Evgeny Gurevich. "Runge-Kutta methods". MA thesis. Universität Münster, 2016. URL: https://math.okstate.edu/people/yqwang/teaching/math4513_fall11/Notes/rungekutta.pdf.

[MS16] Emily Marshman and Chandralekha Singh. “Interactive tutorial to improve student understanding of single photon experiments involving a Mach–Zehnder interferometer”. In: *European Journal of Physics* 37.2 (Feb. 2016), p. 024001. DOI: 10.1088/0143-0807/37/2/024001. URL: https://doi.org/10.1088/0143-0807/37/2/024001.

[Cic17] Francesco Ciccarello. “Collision models in quantum optics”. In: *Quantum Measurements and Quantum Metrology* 4.1 (Dec. 2017). ISSN: 2299-114X. DOI: 10.1515/qmetro-2017-0007. URL: http://dx.doi.org/10.1515/qmetro-2017-0007.

[Mor17] Valter Moretti. *Spectral Theory and Quantum Mechanics: Mathematical Foundations of Quantum Theories, Symmetries and Introduction to the Algebraic Formulation*. 2nd. Springer, 2017.

[OH17] Christoph Ohm and Fabian Hassler. “Measurement-induced entanglement of two transmon qubits by a single photon”. In: *New Journal of Physics* 19.5 (May 2017), p. 053018. DOI: 10.1088/1367-2630/aa6d46. URL: https://doi.org/10.1088/1367-2630/aa6d46.

[SN17] Jun John Sakurai and Jim Napolitano. *Modern Quantum Mechanics*. 2nd. Cambridge University Press, 2017.

[Gro+18] Jonathan A Gross, Carlton M Caves, Gerard J Milburn, and Joshua Combes. “Qubit models of weak continuous measurements: markovian conditional and open-system dynamics”. In: *Quantum Science and Technology* 3.2 (Feb. 2018), p. 024005. DOI: 10.1088/2058-9565/aaa39f. URL: https://doi.org/10.1088/2058-9565/aaa39f.

[Hal+18] Dominic Hallett, Edmund Clarke, Andrew P. Foster, David L. Hurst, Ben Royall, Pieter Kok, Igor E. Itskevich, A. Mark Fox, Maurice S. Skolnick, and Luke R. Wilson. “Electrical control of nonlinear quantum optics in a nano-photonic waveguide”. In: *Optica* 5.5 (2018), pp. 644–650. DOI: 10.1364/OPTICA.5.000644.

[Le18] Trung-Thanh Le. “New Approach to Mach-Zehnder Interferometer (MZI) Cell Based on Silicon Waveguides for Nanophotonic Circuits”. In: *Applications of Silicon Photonics in Sensors and Waveguides*. Ed. by Lakshmi Narayana Deepak Kallepalli. London: IntechOpen, 2018. Chap. 3. DOI: 10.5772/intechopen.76181. URL: https://doi.org/10.5772/intechopen.76181.

[For+19] P. Forn-Díaz, L. Lamata, E. Rico, J. Kono, and E. Solano. “Ultrastrong coupling regimes of light-matter interaction”. In: *Rev. Mod. Phys.* 91 (2 June 2019), p. 025005. DOI: 10.1103/RevModPhys.91.025005. URL: https://link.aps.org/doi/10.1103/RevModPhys.91.025005.

[KM19] Alexander Holm Kiilerich and Klaus Mølmer. "Input-Output Theory with Quantum Pulses". In: *Phys. Rev. Lett.* 123 (12 Sept. 2019), p. 123604. DOI: 10.1103/PhysRevLett.123.123604. URL: https://link.aps.org/doi/10.1103/PhysRevLett.123.123604.

[Ste+19] Gregory R. Steinbrecher, Jonathan P. Olson, Dirk Englund, and Jacques Carolan. "Quantum optical neural networks". In: *npj Quantum Information* 5.1 (2019), p. 60. ISSN: 2056-6387. DOI: 10.1038/s41534-019-0174-7. URL: https://doi.org/10.1038/s41534-019-0174-7.

[HJE20] Mikkel Heuck, Kurt Jacobs, and Dirk R. Englund. "Photon-photon interactions in dynamically coupled cavities". In: *Phys. Rev. A* 101 (4 Apr. 2020), p. 042322. DOI: 10.1103/PhysRevA.101.042322. URL: https://link.aps.org/doi/10.1103/PhysRevA.101.042322.

[Vir+20] Pauli Virtanen, Ralf Gommers, Travis E. Oliphant, Matt Haberland, Tyler Reddy, David Cournapeau, Evgeni Burovski, Pearu Peterson, Warren Weckesser, Jonathan Bright, Stéfan J. van der Walt, Matthew Brett, Joshua Wilson, K. Jarrod Millman, Nikolay Mayorov, Andrew R. J. Nelson, Eric Jones, Robert Kern, Eric Larson, C J Carey, İlhan Polat, Yu Feng, Eric W. Moore, Jake VanderPlas, Denis Laxalde, Josef Perktold, Robert Cimrman, Ian Henriksen, E. A. Quintero, Charles R. Harris, Anne M. Archibald, Antônio H. Ribeiro, Fabian Pedregosa, Paul van Mulbregt, and SciPy 1.0 Contributors. "SciPy 1.0: Fundamental Algorithms for Scientific Computing in Python". In: *Nature Methods* 17 (2020), pp. 261–272. DOI: 10.1038/s41592-019-0686-2.

[Bon21] Maria Bondani. "Single-photon Mach-Zehnder interferometry for High Schools". In: *Journal of Physics: Conference Series* 1929.1 (2021), p. 012055.

[Upp+21] Ravitej Uppu, Leonardo Midolo, Xiaoyan Zhou, Jacques Carolan, and Peter Lodahl. "Quantum-dot-based deterministic photon–emitter interfaces for scalable photonic quantum technology". In: *Nature Nanotechnology* 16.12 (2021), pp. 1308–1317. ISSN: 1748-3395. DOI: 10.1038/s41565-021-00965-6. URL: https://doi.org/10.1038/s41565-021-00965-6.

[Uts+22] Takeru Utsugi, Akihisa Goban, Yuuki Tokunaga, Hayato Goto, and Takao Aoki. "Gaussian-wave-packet model for single-photon generation based on cavity quantum electrodynamics under adiabatic and nonadiabatic conditions". In: *Phys. Rev. A* 106 (2 Aug. 2022), p. 023712. DOI: 10.1103/PhysRevA.106.023712. URL: https://link.aps.org/doi/10.1103/PhysRevA.106.023712.

[Bun23] Matias Bundgaard-Nielsen. “Modeling Tools For Quantum Networks”. Master’s thesis. Technical University of Denmark, Electro, 2023.

[Ewa+23] Jacob Ewaniuk, Jacques Carolan, Bhavin J. Shastri, and Nir Rotenberg. “Imperfect Quantum Photonic Neural Networks”. In: *Advanced Quantum Technologies* 6.3 (2023), p. 2200125. DOI: https://doi.org/10.1002/qute.202200125. eprint: https://advanced.onlinelibrary.wiley.com/doi/pdf/10.1002/qute.202200125. URL: https://advanced.onlinelibrary.wiley.com/doi/abs/10.1002/qute.202200125.

[GK23] Christopher C. Gerry and Peter L. Knight. *Introductory Quantum Optics*. Cambridge: Cambridge University Press, 2023.

[Jac23] Dan Jackson. *Quantum Beam Splitters & The Hong-Ou-Mandel Effect*. Cantor’s Paradise. Jan. 2023. URL: https://www.cantorsparadise.com/quantum-beam-splitters-the-hong-ou-mandel-effect-a59eda66de04.

[KH23] Sangbae Kim and Byoung S. Ham. “Observations of the delayed-choice quantum eraser using coherent photons”. In: *Scientific Reports* 13.1 (2023), p. 9758. DOI: 10.1038/s41598-023-36590-7. URL: https://doi.org/10.1038/s41598-023-36590-7.

[Ran24] Farhan Rana. *Propagating quantum states of light*. Cornell University, ECE 531 Lectures, Chapter 8. https://courses.cit.cornell.edu/ece531/Lectures/chapter8.p 2024. URL: https://courses.cit.cornell.edu/ece531/Lectures/chapter8.pdf.

[Sci24] SciPy Developers. *SciPy Special Functions Reference: scipy.special.wofz*. Accessed online. 2024. URL: https://docs.scipy.org/doc/scipy/reference/generated/scipy.special.wofz.html.

[SK24] Siddharth Singh and Rohan Katti. “Quantum analysis of a Mach–Zehnder interferometer with propagating a single photon Gaussian wave packet”. In: *J. Opt. Soc. Am. B* 41.2 (Feb. 2024), pp. 456–465. DOI: 10.1364/JOSAB.498566. URL: https://opg.optica.org/josab/abstract.cfm?URI=josab-41-2-456.

[Sta+24] Mathias J. R. Staunstrup, Alexey Tiranov, Ying Wang, Sven Scholz, Andreas D. Wieck, Arne Ludwig, Leonardo Midolo, Nir Rotenberg, Peter Lodahl, and Hanna Le Jeannic. “Direct observation of a few-photon phase shift induced by a single quantum emitter in a waveguide”. In: *Nature Communications* 15.1 (2024), p. 7583. DOI: 10.1038/s41467-024-51805-9. URL: https://doi.org/10.1038/s41467-024-51805-9.

[Bun+25] Matias Bundgaard-Nielsen, Dirk Englund, Mikkel Heuck, and Stefan Krastanov. “WaveguideQED.jl: An Efficient Framework for Simulating Non-Markovian Waveguide Quantum Electrodynamics”. In: *Quantum* 9 (Apr. 2025), p. 1710. ISSN: 2521-327X. DOI: 10.22331/q-2025-04-17-1710. URL: https://doi.org/10.22331/q-2025-04-17-1710.

[Ber+26] Andrea Bernardi, Marco Clementi, Marcello Bacchi, Matías Rubén Bolaños, Sara Congia, Francesco Garrisi, Andrea Martellosio, Marco Passoni, Alexander Wrobel, Costantino Agnesi, Giuseppe Vallone, Paolo Villoresi, Federico Andrea Sabattoli, Matteo Galli, and Daniele Bajoni. “Gigahertz-rate thin-film lithium niobate receiver for time-bin quantum communication”. In: *Light: Science & Applications* 15.1 (2026), p. 237. DOI: 10.1038/s41377-026-02306-5. URL: https://doi.org/10.1038/s41377-026-02306-5.

[Kri26] D. Kriesell. *Mach Zehnder Interferometer*. Quantum-ABC, 2026. URL: https://quantum-abc.de/mach-zehnder.pdf.